RMIT UNIVERSITY

NUMERICAL AND EXPERIMENTAL STUDY OF MOTION-INDUCED WAKE FLOW AND CONTAMINANT TRANSPORT IN INTERIOR ENVIRONMENTS

A thesis submitted in fulfilment of the requirements for the degree of Doctor of Philosophy

Yao Tao

M.E., Chongqing University, China

School of Engineering

College of Science, Engineering and Health

RMIT University

July 2018

Declaration

I certify that except where due acknowledgement has been made, the work is that of the author alone; the work has not been submitted previously, in whole or in part, to qualify for any other academic award; the content of the thesis is the result of work which has been carried out since the official commencement date of the approved research program; any editorial work, paid or unpaid, carried out by a third party is acknowledged; and, ethics procedures and guidelines have been followed.

Yao Tao

School of Engineering,
College of Science, Engineering and Health,
RMIT University

Acknowledgements

I would like to thank my first supervisor Prof. Jiyuan Tu, for his constant guidance and mentoring throughout my PhD study period, and for giving me wonderful opportunities to improve myself. He always inspired us to explore our potentials and encouraged us to face challenges while also balancing our research and life. His wise guidance has benefited a lot of people and I feel extremely fortunate to be one of them.

Particularly, I am grateful to my second supervisor Dr. Kiao Inthavong for his tremendous academic contributions and countless support. I feel very enlightened and encouraged by his enthusiasm for research. He generously shared brilliant ideas and experience, kept me on track and gave me valuable advices, I greatly appreciate his patience and guidance over these four years.

I also have heartfelt gratitude to all the colleagues in the RMIT CFD group and CSIRO for their kindness and support. It was incredibly lucky to have this group of colleagues working together. They always shared fresh ideas and excellent skills and gave constructive feedbacks on my work. I have benefitted so much from their help and encouragement.

China Scholarship Council (CSC) is sincerely acknowledged for providing financial support without which this work would not have been possible.

My deepest gratitude belongs to my parents for their unconditional support and love throughout my life. With their trust and confidence in me, I stood the chance to have this experience which turned out to change my life.

Last but not least, I would like to express special gratitude to my white fuzzy cat Paper for her unique support by not accidentally typing this dissertation when I was away, and Mr. Sean Read who have brought extraordinary wisdom to my life.

Publications during Candidature

Peer Reviewed Journal Publications:

1. **Tao, Y.,** Inthavong, K. & Tu, J. Y. (2016). Computational Fluid Dynamics Study of Human-Induced Wake and Particle Dispersion in Indoor Environment. *Indoor and Built Environment*, 26, 185-198.
   DOI: 10.1177/1420326X16661025, ***IF = 1.181, Q2***

2. **Tao, Y.,** Dong, J., Pan, X., Xiao, Y. & Tu, J. Y. (2017). Investigation of the Channelling Effect on Pollutants Dispersion between Adjacent Roadway Tunnels. *International Journal of Environmental Science and Technology*, 14, 2733-2744.
   DOI: 10.1007/s13762-017-1355-6, ***IF = 2.037, Q2***

3. **Tao, Y.,** Inthavong, K. & Tu, J. Y. (2017). A Numerical Investigation of Wind Environment around a Walking Human Body. *Journal of Wind Engineering and Industrial Aerodynamics*, 168, 9-19.
   DOI: 10.1016/j.jweia.2017.05.003, ***IF = 2.689, Q1***

4. **Tao, Y.,** Inthavong, K. & Tu, J. Y. (2017). Dynamic Meshing Modelling for Particle Resuspension Caused by Swinging Manikin Motion. *Building and Environment*, 123, 529-542.
   DOI: 10.1016/j.buildenv.2017.07.026, ***IF = 4.539, Q1***

5. **Tao, Y.,** Inthavong, K., Petersen, P., Mohanarangam, K., Yang, W., Tu, J. Y. (2018). Experimental visualisation of wake flows induced by different shaped moving manikins, *Building and Environment,* 142, 361—370.
   DOI: 10.1016/j.buildenv.2018.06.018. ***IF = 4.539, Q1***

6. **Tao, Y.,** Inthavong, K., Petersen, P., Mohanarangam, K., Yang, W., Tu, J. Y. (2018). Vortex structures, and wake flow analysis from moving manikin models. *Building Simulation, Submitted.*

7. Heschl, C., **Tao, Y.,** Inthavong, K. & Tu, J. Y. (2016). Improving Predictions of Heat Transfer in Indoor Environments with Eddy Viscosity Turbulence Models. *Building Simulation*, 9, 213-220.
   DOI: 10.1007/s12273-015-0260-5, ***IF = 1.673, Q1***

8. Inthavong, K., **Tao, Y.,** Petersen, P., Mohanarangam, K., Yang, W. & Tu, J. Y. (2017). A Smoke Visualisation Technique for Wake Flow from a Moving Human Manikin. *Journal of Visualization*, 20, 125-137.
   DOI: 10.1007/s12650-016-0386-2, ***IF = 0.971, Q3***

9. Dong, J., **Tao, Y.,** Xiao, Y. & Tu, J. Y. (2017). Numerical Simulation of Pollutant Dispersion in Urban Roadway Tunnels. *The Journal of Computational Multiphase Flows*, 9, 26-31.
   DOI: 10.1177/1757482X17694041, ***IF = 0.640, Q3***

Conference Publications:

1. **Tao, Y.,** Inthavong, K., Petersen, P., Mohanarangam, K., Yang, W. & Tu, J. Y. (2015). CFD study of human-induced wake and particle dispersion in indoor environment. *Ventilation 2015 - the 11th International Conference on Industrial Ventilation*, 26-28 Oct, Shanghai, China.

2. **Tao, Y.,** Dong, J., Pan, X., Xiao, Y. & Tu, J. Y. (2015). Air Pollutant Channelling Effect between Roadway Tunnel Segments. *Ventilation 2015 - the 11th International Conference on Industrial Ventilation*, 26-28 Oct, Shanghai, China.

3. **Tao, Y.,** Inthavong, K. & Tu, J. Y. (2016). A numerical investigation of wake flow characters during human gait cycle in the indoor environment. *20th Australasian Fluid Mechanics Conference (AFMC)*, 5-8 Dec, Perth, Australia.

4. **Tao, Y.,** Dong, J., Xiao, Y. & Tu, J. Y. (2016). Numerical analysis of pollutants dispersion in urban roadway tunnels. *20th Australasian Fluid Mechanics Conference (AFMC)*, 5-8 Dec, Perth, Australia.

5. **Tao, Y.,** Inthavong, K., Petersen, P., Mohanarangam, K., Yang, W., Tu, J. Y. (2016). Experimental and CFD modelling of indoor air and particle re-dispersing from a moving manikin. *20th Australasian Fluid Mechanics Conference (AFMC)*, 5-8 Dec, Perth, Australia.

6. **Tao, Y.,** Inthavong, K., Petersen, P., Mohanarangam, K., Yang, W., Tu, J. Y. (2018). Numerical Simulation and experimental verification of wake flows induced by moving manikins. COBEE2018 – the 4th international Conference on Building Energy & Environment, 5-9 Feb, Melbourne, Australia

Credits

The following publications have been used as portion of the materials in this thesis:

Chapter 4

Tao, Y., Inthavong, K. & Tu, J. Y. (2016). Computational Fluid Dynamics Study of Human-Induced Wake and Particle Dispersion in Indoor Environment. *Indoor and Built Environment,* 26, 185-198.
DOI: 10.1177/1420326X16661025, ***IF = 1.181, Q2***

Tao, Y., Inthavong, K., Petersen, P., Mohanarangam, K., Yang, W. & Tu, J. Y. (2015). CFD study of human-induced wake and particle dispersion in indoor environment. *Ventilation 2015 - the 11th International Conference on Industrial Ventilation*, 26-28 Oct, Shanghai, China.

Chapter 5

Tao, Y., Inthavong, K. & Tu, J. Y. (2017). A Numerical Investigation of Wind *Environment* around a Walking Human Body. *Journal of Wind Engineering and Industrial Aerodynamics*, 168, 9-19.
DOI: 10.1016/j.jweia.2017.05.003, ***IF = 2.689, Q1***

Tao, Y., Inthavong, K. & Tu, J. Y. (2016). A numerical investigation of wake flow characters during human gait cycle in the indoor environment. *20th Australasian Fluid Mechanics Conference (AFMC)*, 5-8 Dec, Perth, Australia.

Chapter 6

Tao, Y., Inthavong, K. & Tu, J. Y. (2017). Dynamic Meshing Modelling for Particle Resuspension Caused by Swinging Manikin Motion. *Building and Environment*, 123, 529-542.
DOI: 10.1016/j.buildenv.2017.07.026, ***IF = 4.539, Q1***

Tao, Y., Inthavong, K., Petersen, P., Mohanarangam, K., Yang, W., Tu, J. Y. (2016). Experimental and CFD modelling of indoor air and particle re-dispersing from a moving manikin. *20th Australasian Fluid Mechanics Conference (AFMC)*, 5-8 Dec, Perth, Australia.

Chapter 7

Tao, Y., Inthavong, K., Petersen, P., Mohanarangam, K., Yang, W., Tu, J. Y. (2018). Experimental visualisation of wake flows induced by different shaped moving manikins, *Building and Environment,* 142, 361—370. DOI: 10.1016/j.buildenv.2018.06.018. ***IF = 4.539, Q1***

Chapter 8

Tao, Y., Inthavong, K., Petersen, P., Mohanarangam, K., Yang, W., Tu, J. Y. (2018). Vortex structures, and wake flow analysis from moving manikin models. *Building Simulation*, *Submitted.*

Tao, Y., Inthavong, K., Petersen, P., Mohanarangam, K., Yang, W., Tu, J. Y. (2018). Numerical Simulation and experimental verification of wake flows induced by moving manikins. COBEE2018 – the 4th international Conference on Building Energy & Environment, 5-9 Feb, Melbourne, Australia

Contents

List of Figures

List of Tables

Nomenclature

α	Thermal diffusivity
α_k	Inverse effective Prandtl number for k
α_ε	Inverse effective Prandtl number for ε
Γ	Diffusion coefficient of the scalar
λ	Thermal conductivity
μ	Dynamic viscosity
μ_t	Turbulent viscosity
μ_{eff}	Effective viscosity
ν	Kinematic viscosity
ν_t	Turbulent kinematic viscosity
ϕ	Scalar variable for governing equation
ρ	Density
ρ_p	Particle density
τ	Wall shear stress
ε	Dissipation rate of turbulent kinetic energy
AR	Aspect ratio
C_p	Specific heat
d_p	Particle diameter
F_D	Drag force
k	Turbulent kinetic energy

p	Pressure
PM	Particular Matter
Pr	Prandtl number
$R_{i,j}$	Reynolds stress
Re	Reynolds number
Re_p	Particle Reynolds number
S	Source term
St	Strouhal number
T	Temperature
$\overline{u_\iota}$	Mean velocity
$\mathrm{u_i}'$	Fluctuating velocity components
$\vec{u}_g$	Grid velocity
u_p	Particle velocity
UDF	User Defined Function

Abstract

This thesis focuses on the characteristics of motion-induced wake flow and their influence on contaminant transport in interior spaces. The motion of objects such as human bodies would generate wake regions that exhibit highly complicated airflow characteristics. Consequently, it affects the air quality by inducing contaminant transport in interior environments such as manufacturing, hospital wards, clean rooms and airline cabin etc., where occupants' exposure to airborne contaminants are of concern.

A growing number of Computational Fluid Dynamics (CFD) studies investigated the motion-induced wake dynamics and its integration with particle modelling for air quality assessments. Although CFD with dynamic mesh improves the modelling capability to capture transient effects of motion-induced flow, some characteristics of the dynamic wake induced by the motion that is modelled remain unclear. For example, there are differences in flow field between moving rigid body motion and that of realistic human gait cycles, as well as the heat transfer leading to thermal plumes from the human body during the walking and after stopping. Addressing the airflow disturbances from motion is important for understanding the exposure to airborne contaminants which can be prevalent in indoor environments. On the other hand, flow measurements of moving bodies present significant challenges due to setup, large scales, and their dynamic nature. To date little experimental work has been performed to reproduce and visualise the wake flow induced by a moving object, partly due to the challenges in flow visualisation techniques for capturing dynamic flow fields (as opposed to traditional steady state flows).

The main body of this thesis is composed of nine chapters:

In the first two chapters, a research background and a comprehensive literature review are summarised with highlighted research gaps found in the existing literature followed by the research methodology in Chapter 3. Main research contributions are demonstrated from Chapters 4 to 8. In Chapter 4, the wake flow generated by the motion of a rigid manikin and its influence on particle re-dispersion from a local source on the ground was investigated by performing CFD simulations of a moving manikin model in a confined room.

Chapter 5 presents the determination of discrepancies produced in the wake flow field by a simplified geometry in the form of a cylinder and a man-shaped manikin. Manikin motion with and without swinging limbs and heat transfer from the body were also examined. This part (Chapter 5) identifies the major flow characteristics due to geometry, moving schemes and thermal plume. Subsequently the simulation of particle dispersion from the floor and its re-dispersion is presented using an anthropomorphic manikin modelled with realistic walking motion and thermal effects under three different walking speeds in Chapter 6. Chapter 7 discusses the wake structures measured from smoke visualisation for three different shaped manikins (slim and larger, standing and walking poses). Qualitative understanding of the gross flow field, captured separation points and vortex shedding phenomena were obtained from the experiments. Chapter 8 presents CFD simulations of airflow induced by the same manikins used in the smoke visualisation, and the CFD modellings were validate using the experimental data by comparing the gross flow field, separation points over the head and vortex structures. All the contributions are concluded and highlighted in Chapter 9.

In summary, this thesis presents an investigation of the influence of motion-induced flow on contaminant re-dispersion and transport in interior spaces. Experimental measurements were conducted to provide qualitative insight into the wake formation and vortex structures. The research contributes to the following outcomes:

(a) The experimental and numerical study provided meaningful data for understanding the spatial and temporal characteristics on the wake flow development of different shaped moving manikins. The CFD modelling identified the major discrepancies produced in the wake flow field due to geometry, moving schemes and thermal plume.

(b) The smoke visualisation technique on moving anthropomorphic manikins reproduced the motion-generated wake and provided a new perspective on visualisation of the dynamic wake structure;

(c) The CFD modelling revealed details of the flow field and provided reasonably good agreement with the experimental observations in the wake region, which can help identify the transport of pollutants from and around moving bodies and predict occupant exposure to contaminants;

The computational and experimental studies presented in this thesis lay a solid foundation to the investigation of airflow characteristics and vortex structures induced by realistic body motion. Also, they provide a comprehensive understanding of the effects of occupant activity on particle exposure and indoor air quality.

Chapter 1
Introduction

1.1 Motivation

A human activity pattern survey (Klepeis et al., 2001) showed that respondents (number of 9196) spent 86.9% of their time indoors and 5.5% in vehicles. With people spending most of their time in interior environments, the air quality in these environments has become a subject of serious concern. However, a large body of scientific evidence has indicated that the air within homes and other buildings can be more seriously polluted than the outdoor air in even the largest and most industrialized cities (EPA, 2013). Due to the feature of enclosed spaces, they may entrap pollutants inside that have been seeped in from the outside or have been generated inside (Sterling and Kobayashi, 1977). Thus, for many people, the risks to health may be greater due to exposure to air pollution indoors than outdoors as poor indoor air quality can result in significant adverse impacts on occupants' health and indoor environment. Short- and long-term exposure to air pollution has been associated with a wide range of human health effects (Ghorani-Azam et al., 2016). Particularly for interior spaces which were commonly associated with contaminant problems such as: public buildings, hospital wards, wood workshop, and airline cabins etc., where inhalation of and exposure to contaminants are of great concern.

Among various types of indoor pollutants particulate matter (PM) constitute a major class. Particle re-suspension has been identified as a factor for indoor PM transport (Zhou et al., 2011) and this is particularly the case when human activity is considered (Oberoi et al., 2010, Inthavong et al., 2013b, Li et al., 2014a, Se et al., 2010, Gao and Niu, 2005). Occupants will inhale airborne particles if they become resuspended or ingest them if they are carried to the human mouth or to food. These types of particles create potential health hazards upon entering the human body. A number of health effects have been identified as being linked to exposure to airborne particles, including decreased lung function, increased respiratory symptoms such as coughing, shortness of breath, wheezing, and asthma attacks, as well as chronic obstructive pulmonary disease, cardiovascular diseases, and lung cancer (Morawska et al., 2003).

Studies focused on residential indoor air quality have been widely carried out. In the assessment of local contaminant concentrations, it is a well-known fact that the influence of movement is important. Human induced wake flow wields significant influence on particle dispersion and re-suspension particularly in affecting exposure levels and particulate matter (PM) sampling readings (Ferro et al., 2004, Mazumdar et al., 2011, Miguel et al., 2005, Inthavong et al., 2012b). For example, in environments that demand cleanliness such as operation rooms, the effect of human activities may cause a high risk of bacterial transport from the nonclean zones to the patient's wound (Memarzadeh, 2003). However, when compared with the influence from mechanical ventilation which has been widely investigated for interior environments, only relatively little is known about the mechanisms of motion-induced airflow and the corresponding impact on the transport of contaminants (Brohus and Nielsen, 1996, Yang and Sekhar, 2014, Brohus et al., 2006). Many earlier studies addressed this problem by using steady flow over a stationary manikin to represent the relative motion between occupants and the airflow, with focused on the thermal effects between the airflow and the thermal plume. However, under that (steady flow) assumption the transport of pollutants from fixed locations cannot be correctly reflected. It was not until recent years with the development of experimental techniques and advanced computational resources that more complicated motion of objects could be simulated, and the mechanism of motion-induced wake could start to be revealed.

Computer Fluid Dynamics (CFD) software is one of the most typical methods to investigate and evaluate airflow and air quality in indoor environments. Among the research methods, it is undoubtedly that actual measurement is the most reliable method to provide an accurate description for the indoor air quality; however, to carry out extensive parametric studies is expensive, time-consuming, difficult and sometimes dangerous, and the level of detail is practically limited. Nowadays CFD technique is found in almost all the fields ranging from medical research to engineering. It has the advantage of producing a great time and cost reduction, especially the possibility to generate different graphs and visualisations facilitates an understanding of the features of the results. So far many studies had proved the capability of CFD study in evaluating the wind environment around bluff bodies (Heist et al., 2003, Murakami et al., 1999, Ono et al., 2008, Craven and Settles, 2006) and furthermore evaluating the exposure to contaminants (Li et al., 2013, Carpentieri et al., 2011, Ge

et al., 2013). Recently a growing number of CFD studies started to focus on the influence of moving objects on pollutant transport achieved by the dynamic meshing technique (Hang et al., 2014, Poussou et al., 2010, Wu and Gao, 2014).

As mentioned above, a major type of indoor pollutant is particulate matters. Hence the re-dispersion and transport of particles plays a significant role in indoor air quality assessment. In CFD simulations, two approaches are employed to simulate particulate transport in indoor spaces - the Eulerian model and the Lagrangian model. In the Eulerian model, the particle phase is treated as an additional continuous phase inter-penetrating with the continuous phase and two sets of conservation equations governing the mass, momentum and energy of each phase are solved; whereas In the Lagrangian model, the continuous phase is governed by the Eulerian equation and the particles are tracked using the Lagrangian method by solving the equation of motion separately through the continuous fluid field. Comparing to the Eulerian model, the Lagrangian model could comprehensively depict the particle transport and describe the particle movement from the releasing point to the destination. However, simulating particle dispersion with moving bodies is very challenging due to the extremely high computational demand for movement caused by mesh re-generation and coupled physical phenomena between particles and the fluid, as well as the fact that the location of particle source and indoor activity patterns greatly affect the transport mechanisms. Therefore, more fundamental investigations of motion-induced wake flow are in demand to reveal the influence of body motion on particle re-dispersion and transport.

As a compromise, several affecting factors, especially human body related factors such as the shape of the body, the thermal effect, and the realistic movement of limbs were simplified or eliminated in most previous studies to save the computational cost. For example, a number of studies used simplified geometry such as a cuboid or block instead of realistic shaped manikin; the manikin motion was mostly considered rigid, whereas the swinging of limbs was barely applied due to high computational cost. Moreover, the thermal plume was considered negligible during the walking as the walking-induced wake was often assumed to be strong enough to overwhelm the thermal plume, but it remained unclear that when the occupant stopped moving, how influencing of the re-dominated thermal plume would be on the exposure to contaminates especially in the breathing region. With the research gaps identified, this

thesis aims to provide a comprehensive understanding of airflow characteristics induced by body motion and the effects of occupant activity on particle exposure and indoor air quality.

1.2 Objectives

The aim of this study is to understand the fundamental fluid dynamics of the motion-induced wake flow and its influence on contaminant transport in interior environments. The commercial CFD package ANSYS Fluent (v14.5) was used to simulate the airflow and contaminant dispersion. Smoke visualisation experiments were conducted to generate smoke from moving manikin bodies. The specific objectives of this thesis are:

- To explore the range and strength of the flow field generated by moving bodies of different shapes, thermal conditions and types of motion by CFD simulations.
- To experimentally capture the transient wake flow development using smoke produced through a chemical reaction and highspeed photography, and to quantify the gross flow field by image post-processing.
- To validate the approach of computational modelling method using dynamic mesh technique for moving objects in interior environments with the experimental data from the smoke visualisation.
- To identify the impact of human-induced wake flow on particle re-dispersion from floors and the distribution of particle concentration in the flow domain, as well as occupant's exposure to contaminants in the near body region.

1.3 Thesis Outline

This thesis is composed of nine chapters. The topic of each chapter is outlined below:

Chapter 2 provides a comprehensive literature review in relation to the existing studies on the bluff body wake and the motion-induced wake, including the experimental studies and the CFD studies. The recent and closely related investigations on flow over fixed bluff bodies and moving bodies are reviewed

and summarised. The existing simulation approaches to predict the particle transport induced by motion in indoor spaces are also reviewed and discussed. The reviewed literature lays a solid foundation for the research outcomes in the following chapters.

Chapter 3 illustrates the detailed strategy and the applied methodologies in the following chapters. The computational modelling starts with a benchmark scenario of rigid motion and iso-thermal condition. After that, more comparisons are made between conditions such as different geometries, thermal conditions and motion types. Particle tracking is also implemented. Accordingly, the computational methods of mesh generation, governing equations (Navier-Stokes equations), turbulence modelling, discrete phase modelling and dynamic mesh are introduced, as well as the experimental method and setup of the smoke visualisation.

Chapter 4 presents a simulation on an iso-thermal manikin with rigid motion and evaluates the motion induced re-dispersion of locally distributed particles on the ground. The Lagrangian model is employed to predict contaminants transport trajectories. The simulated flow field shows the fundamental flow patterns in the wake region. The particles on the floors are significantly disturbed by the motion induced flow, thereby lifting off the ground and dispersing into the ambient air. This chapter provides some insight into the flow and particle dynamics under a preliminary scenario, which is utilized as a benchmark case to be compared with later more realistic scenarios.

Chapter 5 compares the generated flow patterns from simplified scenarios and realistic moving scenarios. Discrepancies in the wake flow field by a simplified geometry in the form of a cylinder and a man-shaped manikin, motion with and without swinging limbs and thermal conditions of the body are determined. This part identifies the major flow characteristics due to different body shapes, rigid motion versus swinging motion, iso-thermal versus thermal conditions. The outcomes prove that the type of motion and thermal plume effect plays a pivotal role on the contaminants transport during walking and after the manikin had stopped respectively.

Chapter 6 subsequently discusses the particle dispersion from the floor and its re-dispersion by simulation using the anthropomorphic manikin modelled with realistic walking and swinging motion, with thermal effects under three

different walking speeds. Particle suspension caused by human activity is influenced by the stratified airflow characteristics induced by the different body parts and their kinematics. The particle concentration comparison under different walking speeds shows the variation of the vertical transport of particles in front of the body and occupant's exposure levels.

Chapter 7 discusses the vortex structures measured from smoke visualisation for three different shaped manikins (slim/larger, standing/walking). A smoke visualisation technique is presented for visualising a moving object through a stagnant environment. High speed camera and image processing techniques are used to capture the generated smoke tracing the moving object, qualitative insight into the wake formation and its transformation during the manikin motion are presented.

Chapter 8 continues unsteady CFD modellings with the same three different shaped models and uses the experimental data from the smoke visualisation to provide validation data for computational simulations. The vortex structures are visualised using an omega vortex identification method and are compared with experimental visualisations. The location and main patterns of the vortex structures match with the smoke visualisation, which can help identify the transport of pollutants from and around the body during walking and coming to a stop.

Chapter 9 concludes and highlights all the conclusions and contributions.

1.4 Contribution

In addition to the knowledge provided by previous researchers, this thesis contributes to the following major outcomes:

(a) The experimental and numerical study provided meaningful data for understanding the spatial and temporal characteristics on the wake flow development of different shaped moving manikins. The CFD modelling identified the major discrepancies produced in the wake flow field due to geometry, moving schemes and thermal plume.

(b) The smoke visualisation technique on moving anthropomorphic manikins reproduced the motion-generated wake and provided a new perspective on visualisation of the dynamic wake structure;

(c) The CFD modelling revealed details of the flow field and provided reasonably good agreement with the experimental observations in the wake region, which can help identify the transport of pollutants from and around moving bodies and predict occupant exposure to contaminants;

Chapter 2
Literature Review

2.1 Human Influence on Pollutant Transport

Human activity has significant influence on indoor airflow patterns due to wake flows and vortex shedding that disturb localised suspended particles (Flynn and Ljungqvist, 1995, Li et al., 2014a, Anthony and Flynn, 2006, Inthavong et al., 2013c). Airborne contaminants that redispersed in the air, if inhaled, can lead to severe or fatal consequences in enclosed indoor environments e.g. surgery theatre (Brohus et al., 2006), clean rooms (Choi and Edwards, 2008)(Choi and Edwards, 2012), and confined spaces such as airline cabins (Poussou et al., 2010, Mazumdar et al., 2011). Qian and Ferro (2008) demonstrated the effects of human activity where 'heavy and fast' walking produced higher resuspension rates compared to less-active walking. Similarly studies investigated human interactions with floor type (You and Wan, 2015), dust type and contaminant concentration in dust loads (Gomes et al., 2007). Zhang et al. (2008) modelled the stepping motions of the foot, down and up and showed that shoe bottom roughness, foot size, walking velocity, background velocity as well as the foot stepping velocities, down and up, all affected particle resuspension rate from the floor as well as the corresponding particle concentrations in the indoor environment.

Exposure level analysis were also conducted to address the influence from occupant activities. Licina et al. (2017) monitored human exposure/inhalation risks to spatially varying indoor emissions and found that the inhalation intake of particles from localized sources was considerably influenced by the source position, manikin thermal plume, and exposure duration. They also pointed out that the well-mixed representation of an indoor environment could underestimate the inhalation intake by 40–90% for various localised indoor emissions, and by up to 3 times for particles emitted from the human envelope. Keshavarz et al. (2017) simulated the effects of thermal plume, respiration and motion of the body on the indoor air quality in a ventilated cubicle with the presence of a heated, breathing and rotating manikin. Their simulation results indicated that the rotation of the manikin significantly

distorted the thermal plume of the body and the associated transport of particulates. Furthermore, the rotation decreased the concentration of particles in the breathing zone of the manikin and the thermal plume generated by the body was distorted by the airflow of the mixing ventilation system.

2.2 Airflow Characteristics in the Wake

2.2.1 Studies on Airflow over Bluff Bodies

The motion-induced wake exhibits fluid dynamics similarities to boundary layer separation of flows over wall-mounted finite bodies, where a mixing zone of vortices entraining air into a reverse flow region is formed (Flynn and Ljungqvist, 1995, Mahjoub Said et al., 2008, Zhang et al., 2016). Over the last several decades there has been a surge of activity concerning wake flows, numerous studies on flow over bluff bodies had provided detailed information of the wake region. The vortex street behind the bluff cylinder contain useful information regarding the distribution of three-dimensional vortex structure. Approaches to this problem have been principally experimental, while later there has been vigorous activity in numerical simulation and analysis (Williamson, 1996). Frederich et al. (2008) performed simulations and experiments to capture the spatial-temporal flow field around a finite circular cylinder mounted on a ground plate, and showed characteristic flow features in the wake include boundary layer separation, shear layer instability and the subsequent vortex formation; and these are strongly affected by downwash effects from the flow over the top free end (Figure 2.1).

Finite bodies are typically classified by their cross-sectional proportions via the aspect ratio AR (*H/D*), which compares the body height *H* to its width *D*. Studies often reported the effects of various aspect ratios (*H/D*) on momentum and heat transport in the wake of wall-mounted finite-length cylinders (Wang et al., 2009, Uffinger et al., 2013). Among cylinders of various proportions, an aspect ratio of 3 is the most similar shape to a human body. Rostamy et al. (2012) compared details in the near-wake region and found the vortex structure behind the cylinder was different for the cylinder of AR = 3 comparing to slimmer cylinders (AR > 3). All cylinders had large re-circulation immediately behind the free end, while a second vortex is found behind the cylinder near

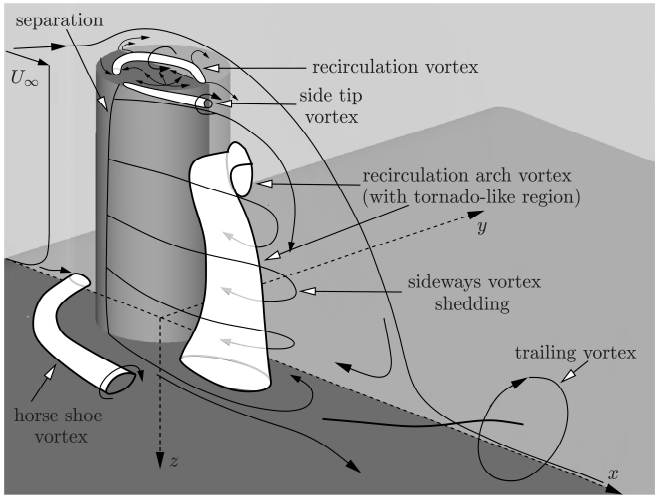

Figure 2.1 A time-averaged flow topology for flow over a cylinder investigated by Frederich et al. (2008)

the cylinder-wall junction except for the cylinder of AR = 3, indicating a distinct wake structure for this cylinder. Moreover, weak upwash flow occurs from the ground plane directed towards the central region of the wake; this upwash flow is weakest for the cylinder of smallest aspect ratio.

Overall, the findings in the bluff body wake flow presented the typical wake structures behind a wall-mounted bluff body and demonstrated that the geometry aspect ratios influence the wake structure. On the one hand, it provided preliminary indications of how human wake flow and vortex structures would develop; on the other hand, it showed that for human bodies with different shape/aspect ratio, the generated wake structure could differ hence changing the influence on particle dispersion. Therefore, the geometry of the human body is carefully considered in this thesis to accurately reflect the wake characteristics.

2.2.2 Flow Over Stationary Manikins

The fluid dynamics of human wake have primarily been investigated by considering a stationary bluff body exposed to an oncoming wind (Inthavong et al., 2013a, Irwin, 2008, Murakami and Deguchi, 1981, Inthavong et al., 2012b, Li et al., 2014b). Early experimental studies (Kulmala et al., 1996, Kim and Flynn, 1991) used a manikin installed in an open-ended wind tunnel, and tracer

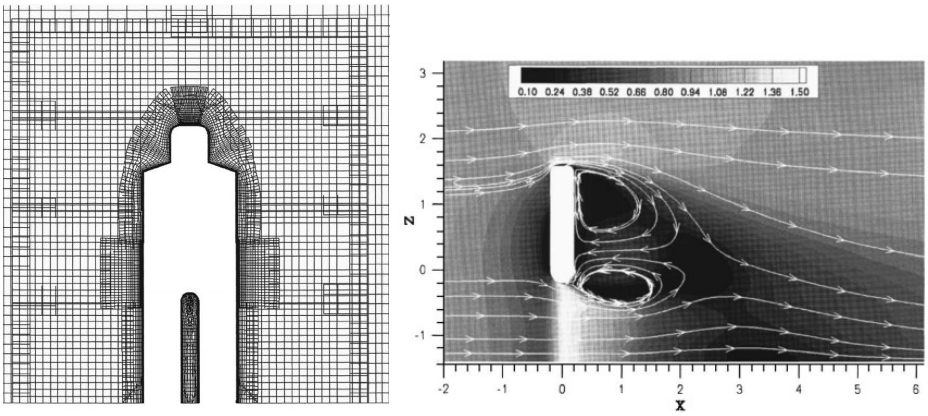

Figure 2.2 Front view of the overset-grid system and the mean velocity magnitude with streamlines for a computational study of flow over a manikin (Edge et al., 2005)

gases were released from different locations to visualise the boundary layer separation, and the size and location of the wake region. CFD studies (Murakami et al., 1999, Hayashi et al., 2002, Ge et al., 2013, Se et al., 2010) have explored the detailed flow structures of unsteady wake regions from stationary manikins and their impact on the subsequent transport of indoor pollutants.

An issue arising with flow over a stationary manikin is the flow separation at the feet which neglects flow unsteadiness caused by the manikin motion; thus, the near wake flow characteristics during walking are only partially represented (though (Brohus et al., 2006) applied distributed momentum sources to simulate movement). In addition, under the assumption of relative motion between airflow and human body, the transport of pollutants from fixed locations cannot be correctly reflected. Simplified geometries such as vertical finite cylinders and cuboids were often used as substitutes for human bodies (Poussou et al., 2010, Thatcher et al., 2004). This also leads to discrepancies between realistic and cylindrical geometries. For example, when legs are considered as two cylinders instead of one single thick cylinder, there is increased mixing in the wake produced by the gap between the legs accelerating flow (Edge et al., 2005, Flynn and Ljungqvist, 1995, Tao et al., 2017b, Tao et al., 2017c).

2.2.3 **Experimental Studies on Moving Manikins**

Flow measurements of moving bodies presents significant challenges due to set up, large scales, and its dynamic nature. Recent experimental studies have

Figure 2.3 Indoor Experimental study of flow field induced by limbs pendulum and body motion measured by anemometers (Han et al., 2015)

focused on the effects of human activity on the fluid wake dynamics by using moving models. Han et al. (2014b) used a full-scale thermal manikin and measured the dynamic airflow with hot-wire anemometers (Figure 2.3) and found the limitation of the method was that measurements were taken at a point (from the probe sensor) and thus unable to obtain comprehensive information of the whole flow field. Luo et al. (2017) conducted PIV measurements on a small-scale cabin with a moving manikin, and observed flow patterns such as symmetric eddies, upward vortex and a strong downwash in the wake flow along the vertical centre plane. A few other studies that have investigated the fluid dynamics from a moving manikin including: Inthavong et al. (2016) investigated an isothermal $1/5^{th}$ scaled rigid moving manikin model; Luo et al. (2015) and Oliveira et al. (2014) investigated natural and forced convection heat transfer from a moving thermal manikin in rigid motion. In the thermal model studies, the heat transfer coefficient increased as a power exponent function with increase of the moving speed.

Poussou et al. (2010, 2012, 2015) conducted small-scale PIV and Planar Laser Induced Fluorenscene (PLIF) measurements to qualitatively capture the wake flow from a moving block and contaminant transport inside an airline cabin. Although PIV experiments provide detailed flow field information, extremely large data sets are needed to achieve statistical average for each image pair covering a small field of view, and at each instantaneous moment in time – and each instantaneous time produces different manikin positions. To date

there are limited experimental studies of wake flow induced by a moving human. This is partly due to the challenges in flow visualisation to capture a moving object compared with a traditional fixed object with a steady state flow. Smoke visualisation provides a qualitative understanding of the gross flow field. Recent studies have demonstrated the ability to capture separation points, reattachment points, and vortex shedding phenomena (Sohankar et al., 2015). Moreover, with high speed photography and image processing, quantitative data can be produced for validating CFD simulation data of moving human subjects/manikins.

2.2.4 CFD Studies on Moving Manikins

A growing number of computational studies have laid emphases on the effects of human activity on the wake dynamics. CFD with dynamic mesh advances the modelling capability to capture transient effects of manikin motion. This was used to qualitatively capture the wake flow from moving blocks (Brohus et al., 2006, Poussou et al., 2010). Realistic anthropomorphic manikins have also been used as they provided more realistic results in the near-body regions (Gao and Niu, 2005). Computational studies have observed wake flow patterns and vortices in the wake region causing significant dispersion of pollutants (Hang et al., 2014, Oberoi et al., 2010, Tao et al., 2017b, Choi and Edwards, 2012, Choi and Edwards, 2008). Choi and Edwards (2012) conducted a large-eddy simulation with an immersed boundary method to demonstrate the contaminant transport owing to complex human- and door-motion-induced wake

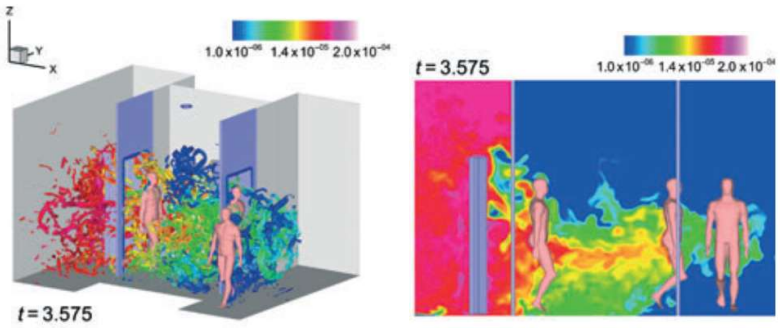

Figure 2.4 Vorticity iso-surfaces coloured by SF6 mass concentration for multiple-men walking events by large-eddy simulation of human-induced contaminant transport in room compartments (Choi and Edwards, 2012)

(Figure 2.4). Their results quantified the effect of different walking speeds and door opening on contaminant transport between room compartments.

To visualise the vortex structures inside the wake, the vorticity parameter, using the q-criterion or λ_2 methods, has been widely adopted to depict the vortex dynamics or to identify vortex cores in the wake region. However, this method can be difficult to accurately distinguish the actual rotational motion of the vortex (Kolář, 2007). The selection of the vorticity value in either the q-criterion or λ_2 methods for vortex identification lacks a clear physical meaning. Additionally, inappropriate values can lead to strong vortices being captured while weak ones are skipped. Moin and Kim (2006) suggest that it is only suitable for vortex visualisation, and that it cannot identify the accurate positions and regions of the vortices. In this study we use an omega vortex identification method proposed by Liu et al. (2016) which is based on a physical meaning of its omega criterion.

While previous studies have advanced the modelling capability and complexity by integrating dispersed particle modelling for inhalation exposure assessments, the investigation of particle re-suspension from floors influenced by a moving manikin with swinging motion and heat transfer needs to be further pursued. For example, there are differences in flow field due to a moving rigid body motion, and that of a swinging human gait cycle, and in combination with a thermal plume. The advancements in modelling can lead to enhanced evaluation of airborne contaminant exposure influenced by occupant activity which is also prevalent in indoor environments (e.g. pollutants, and exhaust fumes in pedestrian/urban streets).

To accurately predict the realistic motion-induced wake, a key factor to consider is the effects of heat transfer leading to thermal plumes from the human body. Murakami et al. (1999) investigated the thermal and dynamic effects of 0.25m/s and 2.5m/s wind on stationary bodies. Velocity and temperature fields around the body revealed a thin layer of warm rising air around the body under a stagnant or weak wind environment; but this disappeared when the wind velocity increased. Combining a wind tunnel experiment and CFD, Li and Ito (2014) and Ono et al. (2008) showed thermal plumes emitting from around a human body in an outdoor environment. Therefore, the effect of heat transfer is an important component for wind flow over a human body. Wu and Gao

(2014) concluded that when the moving speed is larger than 0.4 m/s, the wake flow dominates the micro-environment airflow near the moving body therefore contaminant transport due to the thermal plume became negligible comparing to the motion.

2.3 Particle Transport by the Wake

Particle resuspension and deposition indoors has received increasing attention recently as a result of public concern about contaminant exposure (Lai, 2002). This is particularly the case when human activity is considered as floors are an important reservoir of human-associated contaminants, and human walking is an important contributor to the re-suspension of particles (Oberoi et al., 2010, Goldasteh et al., 2014, Hospodsky et al., 2012, Tian et al., 2014).

Experimental studies have confirmed the occurrence of particle re-suspension caused by human activities. Qian and Ferro (2008) used optical particle counters in a full-scale test chamber and showed that 'heavy and fast' walking produced higher re-suspension rates than less active walking. This was attributed to a combination of increased pace, increased air swirl velocity, and electrostatic field effects established by the walking. Similarly, studies investigated human interactions with floor type (You and Wan, 2015), dust type and contaminant concentration in dust loads (Gomes et al., 2007). Thus, it is necessary to investigate the human-induced wake flow and its influence on the re-suspension of settled particles.

The regular vortex patterns in the wake and their impact on airborne pollutants transport has received a lot of attention (Ferro et al., 2004, Mazumdar et al., 2011, Tian et al., 2016, Wang and Chow, 2011). Vortex shedding in the wake has been shown to influence pollutant dispersion and caused complex behaviour due to advection and turbulent diffusion (Tominaga and Stathopoulos, 2013). For example, Edge et al. (2005) found increased spreading of pollutants attributed to combined effects of the left-right vortex shedding and the downwash effect from the wake coming from a stationary human body. Khare and Marr (2014) demonstrated particle re-suspension/dispersion occurring from the floor induced by the wake produced during human walking. Similar fluid-particle behaviour of airflow over bluff bodies were found in street canyons where wind moving over a building generated a trailing vortex, and pollutant

dispersion was perturbed by the vortices in the wake flow of the buildings (Park et al., 2015, Tsai and Chen, 2004). These studies suggest unsteady vortices in the wake region over bluff bodies are a key factor in influencing pollutant transport.

The computational fluid dynamics (CFD) technique has been proven to be an efficient approach in analysing transport of particulate matters in indoor environments. CFD is not only able to provide full-scale simulations and visualisation of the pollutant transport in a cost-efficient way, but also capable of leading to an in-depth understanding of complicated physical phenomena. Through CFD simulations, a number of studies (Wang et al., 2011, Inthavong et al., 2013b, Gao et al., 2012b, Chang and Hu, 2008, Chen and Zhao, 2010, Han et al., 2014a, Chen et al., 2013) have employed the Lagrangian approach to predict the particle movement in airflows. Zhang and Chen (2007) compared the performance of two modelling methods – the Eulerian model and the Lagrangian model on predicting particle concentration distributions in ventilated spaces. By comparing both results with the experimental data, the Lagrangian method was found to perform better than the Eulerian method in terms of predicting the transient dispersion of the particles from a coughing, though the Lagrangian method was computationally more demanding. Qian and Li (2010) investigated the fate of respiratory particles in a ventilated isolation room both experimentally and computationally. Through Lagrangian model, the effectiveness of the ventilation design on removing fine and large respiratory particles was analysed.

The computational modelling integrating the body motion with dynamic mesh and the particle tracking with Lagrangian model also showed good performance. Goldasteh et al. (2014) simulated the particle resuspension due to shoe stepping on the floor and showed that particles were detached and re-suspended from the substrate during the downward motion of the foot. Their prediction of particle resuspension from Lagrangian approach was validated with the corresponding experimental results. Wang and Chow (2014) numerically investigated the impacts of human movement on the airborne particles distribution in hospital rooms. The Lagrangian method was adopted to trace the motion of droplets and the dynamic mesh model was employed to describing human walking. Results showed the change of suspended droplets

concentration due to walking speeds and posture change, and the adopted models were successfully validated against reported experimental data.

2.4 Summary

Studies on the airflow over stationary objects and moving manikins revealed the complicated structures in the human wake region and confirmed the significant impact of objects motion on indoor air quality. However, there were some questions remained to be addressed, e.g. the wake flow development after the manikin motion stopped; the influence of the ceased motion on pollutant transport; the details of vortex structures of the motion-induced wake, and the validation of CFD simulations of indoor moving objects with higher moving speed etc. Therefore, this study focused on presenting comprehensive descriptions of temporal and spatial characteristics of human-induced wake during the manikin motion and after it stopped. Anthropomorphic geometry, realistic motion and thermal conditions were considered to provide more realistic results of the motion-induced flow field. Particle suspension caused by the human walking was thereby conducted based on the flow field generated by the realistic motion. On the other hand, smoke visualization was adopted as the experimental method to reproduce the wake from moving manikins and provide data to validate with simulation results.

Chapter 3
Methodology

3.1 CFD Geometries and Validation

3.1.1 Cylinder Geometry for Model Validation

The fluid dynamics of wake flow around human body comply with the principle of the boundary layer separation when air flows over bluff bodies such as mounted vertical finite cylinders. Studies into the flow field around fixed cylinders have provided insight into the major characteristics of bluff body aerodynamics, and identified the main flow features of vortices such as downwash flow and recirculation regions extending downstream behind the bluff body (Kawamura et al., 1984, KrajnoviĆ, 2011, Wang and Zhou, 2009).

To validate the numerical modelling accuracy, simulations of near wake flow around mounted vertical cylinders were firstly conducted and validated against PIV measurements by Rostamy et al. (2012), in which a circular cylinder with a similar aspect ratio (AR = 3) to the manikin model was mounted on a plane and had air flowed over it (Figure 3.1a). The same geometry and flow domain were built in the CFD modelling (Figure 3.1b for model validation. To solve the boundary layer separation in the viscous sub-layer on the cylinder surface, very fine prism cells were extruded from the surface. The flow domain

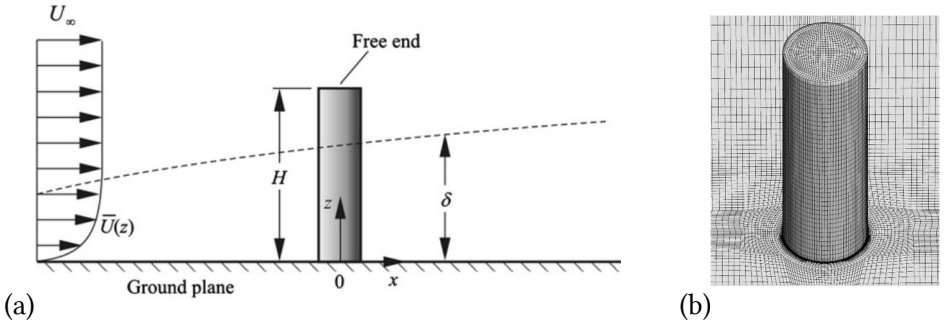

Figure 3.1 (a) A schematic representation of flow past a finite cylinder mounted normal on a ground plane in Rostamy et al. (2012); (b) grids around the cylinder in the CFD model for validation

was calculated by applying identical ambient flow conditions with the experiment data.

3.2 Manikin Models

The computational domain had a manikin model located on the centreline close to the back wall. Different shaped manikins with the same height of 1.7m were placed in the computational domain individually. The manikins used in different cases could be summarised as: (1) a slim body with rigid motion; (2) a slim body with swinging motion; and (3) three manikin bodies (slim, walking pose and large) with rigid motion (Figure 3.2). Manikins moved at different speeds under several case scenarios throughout this study. The length of the enclosed domain varied slightly in each case, the details of the manikins and the domain were clarified in each chapter. Unstructured tetrahedral cells and prism layers were generated around the manikin surface, while a hex-core filled inside the room. To capture the boundary layer separation around the manikin, similarly scaled mesh sizes obtained from the validated wall-mounted cylinder model were applied on the manikins' surface.

(a) Model #1: slim manikin in standing gesture

(b) Model #2: slim manikin in walking gesture

(c) Model #3: larger bodied manikin in standing gesture

Figure 3.2 3D printed manikin models

For the dynamic meshing, the layering mesh method was used to update the moving grids at each new time step for the rigid motion case, while the re-meshing method was applied to re-generate the mesh at each time step for the

swinging motion. The number of steps per second (called cadence) and the walking speed of a person are subject to various human factors. We assumed a cadence of 2 steps per second with a mean walking speed of 1.2 m/s based on gait parameters presented in Al-Obaidi et al. (2003). The total flexion angle for the arms and legs were 60°and 40° based on Han et al. (2013) and the rotating limb angular velocities were calculated from the length of limbs, the swinging period, and walking speed. The gait cycle was achieved by defining the angular limb velocities through a User-Defined-Function (UDF) in the commercial CFD software ANSYS Fluent v14.5.

The body temperature is usually set in the range of 30.3°C to 33.7°C (Murakami et al., 1999, Salmanzadeh et al., 2012, Li et al., 2013). In this study, the manikin used a fixed surface temperature of 32°C, with an air temperature of 22°C. Since one of our objectives was to compare the thermal plume around the manikin during walking, the convective heat transfer from the body surface was the main contributor, and radiation, evaporation, and respiration were not considered. Likewise, clothing was not considered.

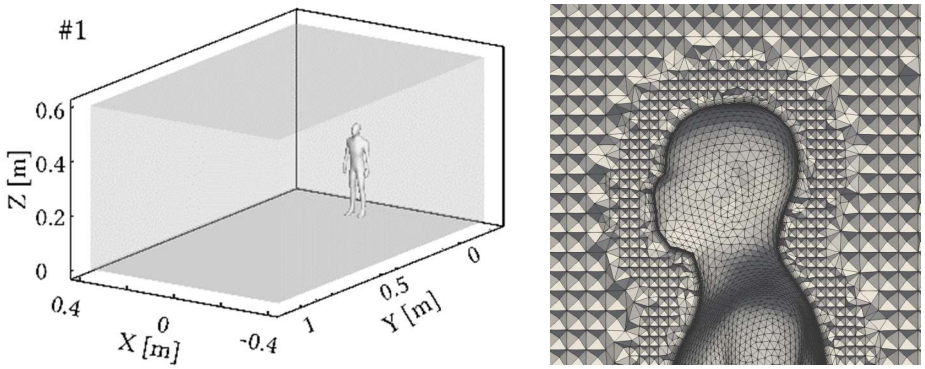

Figure 3.3 CFD models of (a) the computational domain; (b) the mesh setup of the slim standing body.

3.3 CFD Airflow Modelling

The physical characteristics of the fluid motion related to velocity, pressure, temperature, density, etc. are usually described through the incompressible Navier-Stokes equations which are often called governing equations in CFD.

3.3.1 Governing Equations

The governing equation of the continuous gas phase is obtained by identifying the fundamental principles based on conservation of mass, Newton's second law for the conservation of momentum and first law of thermodynamics for the conservation of energy. The general form of transport equation for incompressible flow is expressed as (3.1):

$$\frac{\partial \phi}{\partial t} + \nabla \cdot (\phi \vec{V}) = \nabla \cdot (\Gamma \nabla \phi) + S_\phi \tag{3.1}$$

Where ϕ is a general fluid property, t represents time, the fluid velocity $\vec{V}$ at any point in the flow field is described by the local velocity components u, v, and w, Γ is a general diffusion coefficient and S_ϕ is the source term. This transport equation can also be expressed using three-dimensional form (3.2):

$$\frac{\partial \phi}{\partial t} + \frac{\partial (u\phi)}{\partial x} + \frac{\partial (v\phi)}{\partial y} + \frac{\partial (w\phi)}{\partial z} = \frac{\partial}{\partial x}\left[\Gamma \frac{\partial \phi}{\partial x}\right] + \frac{\partial}{\partial y}\left[\Gamma \frac{\partial \phi}{\partial y}\right] + \frac{\partial}{\partial z}\left[\Gamma \frac{\partial \phi}{\partial z}\right] + S_\phi \tag{3.2}$$

3.3.2 The Mass Conservation Equation

To achieve the conservation of mass, the scalar variable ϕ is identified as the fluid density ρ in the governing equation while the diffusion is discarded. The conservation form of mass conservation in the absence of mass sources can be expressed as (3.3):

$$\frac{\partial \rho}{\partial t} + \nabla \cdot \left(\rho \vec{V}\right) = 0 \tag{3.3}$$

In the Cartesian coordinate system, it can be expressed as (3.4):

$$\frac{\partial \rho}{\partial t} + \frac{\partial (\rho u)}{\partial x} + \frac{\partial (\rho v)}{\partial y} + \frac{\partial (\rho w)}{\partial z} = 0 \tag{3.4}$$

It reflects the rate of increase of mass within the control volume equals the net rate at which mass enters the control volume. For incompressible flow that density is a constant value:

$$\nabla \cdot \vec{V} = 0 \tag{3.5}$$

3.3.3 The Momentum Equations

Deriving the conservation of momentum from Newton's second law, the scalar variable ϕ is identified as the fluid velocity $\vec{V}$ and Γ is replaced by the kinematic viscosity $\nu = \mu/\rho$, respectively. The force induced by the pressure p is added into the source terms. The conservation form of the momentum equation can be rewritten from the conservation equations as (3.6):

$$\frac{\partial \vec{V}}{\partial t} + (\vec{V} \cdot \nabla)\vec{V} = \nu \nabla^2 \vec{V} - \frac{1}{\rho}\nabla p \tag{3.6}$$

In the Cartesian coordinate system, it can be expressed as:

x momentum:

$$\frac{\partial u}{\partial t} + u\frac{\partial u}{\partial x} + v\frac{\partial u}{\partial y} + w\frac{\partial u}{\partial z} = \nu[\frac{\partial^2 u}{\partial x^2} + \frac{\partial^2 u}{\partial y^2} + \frac{\partial^2 u}{\partial z^2}] - \frac{1}{\rho}\frac{\partial p}{\partial x} \tag{3.7}$$

y momentum:

$$\frac{\partial v}{\partial t} + u\frac{\partial v}{\partial x} + v\frac{\partial v}{\partial y} + w\frac{\partial v}{\partial z} = \nu[\frac{\partial^2 v}{\partial x^2} + \frac{\partial^2 v}{\partial y^2} + \frac{\partial^2 v}{\partial z^2}] - \frac{1}{\rho}\frac{\partial p}{\partial y} \tag{3.8}$$

z momentum:

$$\frac{\partial w}{\partial t} + u\frac{\partial w}{\partial x} + v\frac{\partial w}{\partial y} + w\frac{\partial w}{\partial z} = \nu[\frac{\partial^2 w}{\partial x^2} + \frac{\partial^2 w}{\partial y^2} + \frac{\partial^2 w}{\partial z^2}] - \frac{1}{\rho}\frac{\partial p}{\partial z} \tag{3.9}$$

3.3.4 The Energy Equation

Deriving the equation for the conservation of energy from the first law of thermodynamics, ϕ is substituted by the temperature T, while Γ is the thermal diffusivity ($\alpha = k/\rho C_p$). The equation of conservation of energy can be rewritten as (3.10):

$$\frac{\partial T}{\partial t} + (\vec{V} \cdot \nabla)T = \alpha \nabla^2 T + S_T \tag{3.10}$$

Where, k is the thermal conductivity, C_p represents the thermal capacity and S_T is the internal thermal source. In the Cartesian coordinate system, it can be expressed as (3.11):

$$\frac{\partial T}{\partial t} + u\frac{\partial T}{\partial x} + v\frac{\partial T}{\partial y} + w\frac{\partial T}{\partial z} = \frac{k}{\rho C_p}\left[\frac{\partial^2 T}{\partial x^2} + \frac{\partial^2 T}{\partial y^2} + \frac{\partial^2 T}{\partial z^2}\right] \tag{3.11}$$

3.3.5 Equations for Turbulent Flow

Turbulent flow is a chaotic and irregular state of motion associated with random fluctuations in both direction and magnitude in the fluid. In CFD simulations, the turbulent flow can be solved using the direct numerical solution (DNS), the Large-eddy simulation (LES) or the Reynolds-Averaged Navier-Stokes (RANS) method. The DNS method resolves the whole range of spatial and temporal scales of the turbulence and the LES model resolves all the large eddies, therefore they require significantly high computational cost. Whereas the RANS model approximates time-averaged solutions to the Navier–Stokes equations by decomposing the instantaneous quantities, while still provides reasonably reliable solutions to turbulence flows with less computational cost and time. In the RANS model, the scalar variable $\phi(t)$ in the instantaneous Navier-Stokes equations is decomposed into the mean component $\bar{\phi}$ and the fluctuating component $\phi'(t)$:

$$\phi(t) = \bar{\phi} + \phi'(t) \tag{3.12}$$

For the velocity components:

$$u_i(t) = \overline{u_i} + u_i'(t) \tag{3.13}$$

Where $\overline{u_i}$ and $u_i'(t)$ are the mean and fluctuating velocity components. The intensity of the turbulence flow can be defined by the ratio of the fluctuating velocity to the mean velocity:

$$I = \frac{u_i'}{\overline{u_i}} = \frac{\sqrt{\frac{1}{3}({u_x'}^2 + {u_y'}^2 + {u_z'}^2)}}{\sqrt{{\bar{u}_x}^2 + {\bar{u}_y}^2 + {\bar{u}_z}^2}} \tag{3.14}$$

In which the mean velocity is:

$$\bar{u}_i = \frac{1}{t}\int_{t_0}^{t_0+t} u(x,y,z,t)dt \tag{3.15}$$

And the mean and fluctuating velocity component is:

$$\overline{u_i'(t)} = \frac{1}{t}\int_{t_0}^{t_0+t} u_i'(t)dt = \frac{1}{t}\int_{t_0}^{t_0+t} (u_i(t) - \bar{u}_i)dt = 0 \tag{3.16}$$

By substituting expressions of the decomposed form for the flow variables into the continuity equation and taking a time average, the ensemble-averaged momentum equations can be written as:

$$\frac{\partial \bar{u}_i}{\partial x_i} = 0 \tag{3.17}$$

Similarly, the momentum equation would become:

$$\frac{\partial \bar{u}_i}{\partial t} + \frac{\partial}{\partial x_i}(\bar{u}_i\bar{u}_j) = \nu\frac{\partial^2 \bar{u}_i}{\partial {x_i}^2} - \frac{1}{\rho}\frac{\partial p}{\partial x_i} + \frac{\partial}{\partial x_i}(-\overline{u_i'u_j'}) \tag{3.18}$$

The above equations are called Reynolds-averaged Navier-Stokes (RANS) equations. The additional term $\overline{u_i'u_j'}$ representing the effects of turbulence is related to the Reynolds stress tensor:

$$R_{ij} = \rho\overline{u_i'u_j'} \tag{3.19}$$

3.3.6 The RNG k-ε Turbulence Model

Among the RANS turbulence models, the RNG (Re-Normalisation Group) k-ε model has been widely employed due to its good performance on modelling indoor airflow and pollutant transport (Chen and Chao, 1997). The RNG k-ε model was developed by Yakhot and Orszag (1986), (1992) from the standard k-ε model to account for the effects of smaller scales of motion by using a modified form of the epsilon equation through changes to the production term. The RNG k-ε model has a broader applicability and is more reliable and accurate than the standard k-ε model under very complex environment with wider class of flows. In the standard k-ε model (Launder and Spalding, 1974) in which

k represents the turbulence kinetic energy and ε stands for its rate of dissipation:

$$k = \frac{1}{2}\overline{u_\iota{}' u_\iota{}'} \tag{3.20}$$

$$\varepsilon = \nu \overline{\frac{\partial u_\iota{}' \partial u_\iota{}'}{\partial x_j \partial x_j}} \tag{3.21}$$

The transport equation of the RNG k-ε model has a similar form to the standard k-ε model, and in the ANSYS FLUENT is given as:

$$\frac{\partial(\rho k)}{\partial t} + \frac{\partial}{\partial x_i}(\rho k u_i) = \frac{\partial}{\partial x_j}[\alpha_k \mu_{eff} \frac{\partial k}{\partial x_j}] + G_k + G_b - \rho\varepsilon - Y_M + S_k \tag{3.22}$$

And

$$\frac{\partial(\rho\varepsilon)}{\partial t} + \frac{\partial}{\partial x_i}(\rho\varepsilon u_i) = \frac{\partial}{\partial x_j}[\alpha_\varepsilon \mu_{eff} \frac{\partial \varepsilon}{\partial x_j}] + C_{1\varepsilon}\frac{\varepsilon}{k}(G_k + C_{3\varepsilon}G_b) - C_{2\varepsilon}\rho\frac{\varepsilon^2}{k} - R_\varepsilon + S_\varepsilon \tag{3.23}$$

Where, G_k represents the generation of turbulent kinetic energy due to the mean velocity gradients, and G_b is the generation of turbulent kinetic energy due to buoyancy. The quantities α_k and α_ε are the inverse effective Prandtl numbers for k and ε, respectively, $\alpha_k = \alpha_\varepsilon \approx 1.393$. μ_{eff} is the sum of the fluid viscosity μ and the turbulent viscosity μ_t, where μ_t is computed by combining k and ε as:

$$\mu_t = \rho C_\mu \frac{k^2}{\varepsilon} \tag{3.24}$$

The model constantsC_μ, $C_{1\varepsilon}$ and $C_{2\varepsilon}$ have values derived analytically by the RNG theory. These values are:$C_\mu = 0.0845$, $C_{1\varepsilon}$ = 1.42, $C_{2\varepsilon}$=1.68.

3.4 Particle Modelling

3.4.1 The Eulerian-Lagrangian Model

The Lagrangian approach is the most popular two-phase flow model for modelling PM transport when the dispersed second phase occupies a low volume fraction. It has unique advantage in describing particle movement from the injection point to the destination. The airflow is treated as a continuum by solving the Navier-Stokes equations, while the dispersed phase is solved by tracking particles through the calculated flow field separately. It also allows an integrated inter-phase coupling which could include various interacting mechanisms between the phases.

The discrete phase model (DPM) in ANSYS FLUENT follows the Euler-Lagrange approach and is used in this study to model the particle re-suspension. In this Euler-Lagrange method, the fluid phase is treated as a continuum by solving the Navier-Stokes equations, while the dispersed phase is solved by tracking a large number of particles through the calculated flow field. The dispersed phase can exchange momentum, mass, and energy with the fluid phase. The Lagrangian particle tracking model is based on the particle force balance equation given as:

$$\frac{\partial u_p}{\partial t} = F_D(u - u_p) + \frac{g(\rho_p - \rho)}{\rho_p} + F_x \tag{3.25}$$

where u is the fluid phase velocity and up is the particle velocity; ρ is the fluid density and ρ_p is the particle density. F_x is additional acceleration forces. $F_D(u - u_p)$ is the drag force per unit particle mass and F_D is defined using the spherical drag law:

$$F_D = \frac{18\mu}{\rho_p {d_p}^2} \frac{C_d Re}{24} \tag{3.26}$$

d_p is the particle diameter, Re is the relative Reynolds number which is defined as:

$$Re = \frac{\rho d_p |u_p - u|}{\mu} \tag{3.27}$$

The effect of turbulent dispersion on particles can be modelled in the Lagrangian model by adding an eddy fluctuating component onto the mean air velocity. It is the fluctuating component of the air velocity which causes the dispersion of particles in turbulent flow:

$$u_f' = \zeta(\frac{2}{3}k)^{0.5} \tag{3.28}$$

Where ζ is a normally distributed random number which accounts for the randomness of turbulence. The particle motion equation is solved for the entire time that the particle interacts with the turbulent eddy. This time is defined as the minimum between the eddy lifetime and the time required by the particle to pass through the eddy. In each eddy, the fluctuating eddy velocity can be varied by the eddy length scale and the lifetime t_e:

$$L_e = \frac{C_\mu^{3/4} k^{3/2}}{\varepsilon} \tag{3.29}$$

$$t_e = L_e/(\frac{2}{3}k)^{1/2} \tag{3.30}$$

The model of turbulent dispersion of particles assumes that a particle is always within a single turbulent eddy. When a particle enters the eddy, the fluctuating velocity for that eddy will impose impact on the particle when two conditions are satisfied: (1) the time of interaction between the particle and the eddy interaction is less than the eddy lifetime, and (2) the displacement of the particle relative to the eddy is less than the eddy length. If either condition is exceeded, the particle is assumed to be entering a new eddy with new u_f', t_e, and L_e (ANSYS, 2009).

3.5 Dynamic Mesh Modelling

3.5.1 Dynamic Mesh

The dynamic mesh model in ANSYS Fluent is used to model flows where the shape of the domain is changing with time due to motion on the boundaries. There are three groups of dynamic mesh in ANSYS Fluent to update the volume mesh in the deforming regions subject to the motion defined at the boundaries – smoothing, dynamic layering and local remeshing methods. In

the smoothing method, the edges between any two mesh nodes are idealised as a network of interconnected springs. The dynamic layering method is used in prismatic (hexahedral or wedge) mesh zones to add or remove layers of cells adjacent to a moving boundary, based on the thickness of the layer adjacent to the moving surface. For zones with a triangular or tetrahedral mesh, the remeshing method agglomerates cells that violate the skewness or size criteria and locally re-meshes the agglomerated cells or faces. If the new cells or faces satisfy the skewness criterion, the mesh is locally updated with the new cells (with the solution interpolated from the old cells). Otherwise, the new cells are discarded and the old cells are retained (ANSYS, 2009).

For the purpose of simulating indoor body motion, the dynamic mesh method of dynamic layering and local remeshing methods were both used in this study. When the rigid motion was considered for a case, the whole computation domain was divided into two parts - dynamic mesh zone and static mesh zone, to reduce the amount of dynamic meshes and to save computational time. The dynamic mesh zone updated the hexahedral mesh only at the boundary of the domain – front and back walls of the room. When the realistic motion was to be considered – the swinging of limbs can only be achieved by the re-meshing method, when the mesh close to the moving limbs were all re-meshed according to the criteria. The body motion was prescribed by profile (for layering method) and user-defined functions (for swinging limbs). The update of the volume mesh is handled automatically by ANSYS Fluent at each time step based on the new positions of the boundaries.

The dynamic mesh model in ANSYS Fluent can be used to model flows where the shape of the domain is changing with time due to motion on the domain boundaries. In this study, the manikin body was considered as the moving boundary in the computational domain and was therefore achieved by the layering and re-meshing dynamic mesh methods.

For a general scalar ϕ on an arbitrary control volume V with a moving boundary, the integral form of the conservation equation is given as:

$$\frac{\partial}{\partial t}\int_V \rho\phi dV + \int_{\partial V} \rho\phi(\vec{u} - \vec{u}_g)\cdot d\boldsymbol{A} = \int_{\partial V} \Gamma\nabla\phi \cdot d\boldsymbol{A} + \int_V S_\phi dV \qquad (3.31)$$

where, ϕ represents a scalar, ρ is the fluid density, $\vec{u}$ is the flow velocity vector; $\vec{u}_g$ is the grid velocity of the moving mesh, $\boldsymbol{A}$ is the boundary of the control volume V, Γ is the diffusion coefficient, S_ϕ is the source term.

3.5.2 Motion of the Swinging Model – UDF

A user-defined function (UDF) is a function that written in the C programming language and programmed to be dynamically loaded with the ANSYS FLUENT solver to enhance the standard features of the code. In this study, the swinging motion of limbs was considered as a type of boundary motion and was defined using a UDF. The macro DEFINE_CG_MOTION in UDF was used to specify the motion of a particular dynamic zone by the linear and angular velocities at every time step. ANSYS FLUENT used these velocities to update the node positions on the dynamic zone based on solid-body motion.

DEFINE_CG_MOTION (name, dt, vel, omega, time, dtime)

There are six arguments to DEFINE_CG_MOTION: (*name, dt, vel, omega, time, and dtime). dt, vel, omega, time*, and *dtime* are variables that are passed by the ANSYS FLUENT solver to the UDF. The linear and angular velocities are returned to ANSYS FLUENT by overwriting the arrays *vel* and *omega*, respectively. An example of UDF applied on the swinging manikin in this study is given in Table 3.1.

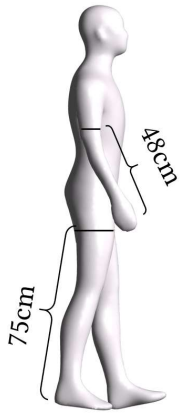

Figure 3.4 The segmentation of body and limbs for applying UDF on dynamic mesh to achieve the swinging motion of limbs

```
#include "udf.h"
#include <math.h>
#include <stdio.h>
#define v1 1.3

DEFINE_CG_MOTION(left_arm, dt, cg_vel, cg_omega, time, dtime)
{
       real t,Rt;
       int t_int, t_cycle;
       Rt = 0.8;
       t = CURRENT_TIME;
       t_int = t*100/Rt;
       t_cycle = t_int%100;
       if (t_cycle >= 0 && t_cycle < 25 )
       {      DT_CG(dt)[0] = -0.2;
              DT_CG(dt)[1] = -0.07+1.2*t;
              DT_CG(dt)[2] = 1.205;
              cg_vel[1] = 1.2;
              cg_omega[0] = -1*v1;
       }
       else if (t_cycle >= 25 && t_cycle < 50)
       {      DT_CG(dt)[0] = -0.2;
              DT_CG(dt)[1] = -0.07+1.2*t;
              DT_CG(dt)[2] = 1.205;
              cg_vel[1] = 1.2;
              cg_omega[0] = v1;
       }

       else if (t_cycle >= 50 && t_cycle < 75)
       {      DT_CG(dt)[0] = -0.2;
              DT_CG(dt)[1] = 0.011+1.2*t;
              DT_CG(dt)[2] = 1.205;
              cg_vel[1] = 1.2;
              cg_omega[0] = v1;
       }
       else if (t_cycle >= 75 && t_cycle < 100)
       {      DT_CG(dt)[0] = -0.2;
              DT_CG(dt)[1] = 0.011+1.2*t;
              DT_CG(dt)[2] = 1.205;
              cg_vel[1] = 1.2;
              cg_omega[0] = -1*v1;
       }
}
```

Table 3.1 An example of UDF describing the swinging motion of the left arm

The manikin motion with swinging limbs was simplified by rotating the arms and legs without bending the elbows and knees. The locations of rotating pivots were set at the front and back points of the horizontal cuts by which limbs were segmented (Figure 3.4), from where the lengths of moving parts were 48cm for arms and 75 cm for legs of a 170cm-tall manikin. The UDF in Table 3.1 showed an example of how left arm was swinging in a gait cycle. "Rt = 0.8" defined the period of a gait cycle as 0.8 secs, and it was then divided into 4

phases: swinging forward, back to vertical, swinging backward, and back to vertical again. “DT_CG(dt)” defined the location of pivot points and it was shown as a function of time (t) as the body was moving forward. “cg_omega[0]” defined the angular velocity of limbs thereby controlled the amplitude of swinging.

3.6 Smoke Visualisation Method

3.6.1 Smoke Generation

Smoke was generated from the chemical reaction between acetic acid (CH_3COOH) and cyclohexylamine ($C_6H_{11}NH_2$) that produces a salt (ethanoate):

$$CH_3COOH + C_6H_{11}NH_2 \longrightarrow C_6H_{11}N + H_3 + CH_3COO -$$

This technique was first patented by (Britt, 1943) as a method to produce smoke without combustion to obscure visibility in warfare, or to overcome a riotous mob. Its use is also prevalent in the arts, such as photography, theatre and movie production for creating the illusion of smoke or fog. The primary substances employed in forming the smoke comprise an amine and an organic acid which are brought together and will react to produce a mass of fine opaque particles of amine salt suspended in the atmosphere. The amine used in this work was cyclohexylamine because of its availability and relatively low health risk. It reacts with a volatile liquid organic acid in the presence of air at standard atmospheric or room temperatures to produce smoke. The acid used in this work was acetic acid also because of its availability, low cost, and low health risk. It is a liquid at standard atmospheric temperature and pressure and is able to react with a carbon containing amine without additional heat energy. While the method is not new, it was introduced as a technique for visualising flow streamlines of moving bodies in a stagnant fluid in Inthavong et al. (2017).

Smoke is visualised from illuminating light reflecting off the opaque amine salts formed as the by-product of the chemical reaction between the cyclohexylamine and acetic acid. The settling velocity of the amine salt particles is extremely low and therefore are ideal as a tracer gas. The particles are also extremely effective in reflecting light. Since the smoke visualisation depends on

light illumination. a strong light source with a dark contrasting background is needed.

A comprehensive risk assessment was undertaken for the entire experiment according to Australian HSE (Health Safety Environment) standards. The outcome of the assessment included allowing only two operators close to the rig. Personal protective equipment for the two operators included a full-face mask worn at all times to filter the acetic acid vapour, and cyclohexylamine. Protective clothing for operators and strict chemical handling procedures from the outcomes of the risk assessment were also followed during the course of the experiment.

3.6.2 Test Chamber and Manikin

A 1/5th scaled model of an indoor room was created with dimensions of 800mm (x-coordinate) × 1100mm (y-coordinate) × 600mm (z-coordinate) (Figure 3.5). Two trays of acetic acid (40%) were placed on the floor in opposing corners and allowed to evaporate into the air, thereby saturating the air inside the chamber. A small CPU-fan was used to increase the evaporation rate and reach a well-mixed room condition. We found that the fan operating for approximately 5 mins was the optimal time to produce sufficient acid vapour in the air. After 5 min, the fan was switched off and the air was allowed settle to an idle state. An exhaust vent was connected to the ceiling to purge the chamber

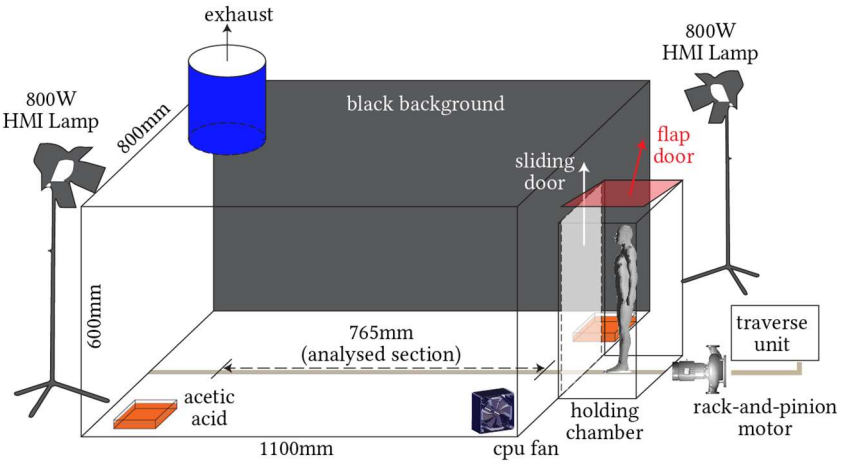

Figure 3.5 Indoor room scaled at 1/5th dimension. On the floor are the acetic acid (as a volatile liquid) trays, and CPU mixing fan. Light is sourced from two 800W lamps.

after each experimental run. Upon completion of each run, an 11kW suction fan was used to remove the fumes from the measurement chamber. The suction fan was run for a minute such that there was a turnover of almost 100 times compared to volume of the measurement chamber, which ensured that for every repeating run, the wake flow was only caused by the current movement.

Rectangular fabric material (approximately 2cm^2) were stuck on the manikin in different locations and cyclohexylamine was dabbed onto its surface. The amount of cyclohexylamine (85%) is very small (less than 0.1 ml for each application), a dab with a cotton tip swab was enough to wet the fabric material in locations of interest for each run of the experiment. Smoke was formed via the chemical reaction between the acetic acid (CH_3COOH) saturated air and the cyclohexylamine ($C_6H_{11}NH_2$). The reaction produced smoke (comprised of suspended opaque amine salt particles) suitable for flow visualisation with a high-speed camera. A black background was used to provide strong contrast when light scattering illuminated the smoke. A Phantom Miro M310 high speed camera with a Canon 90mm f/2.8 shift lens was used to capture the trailing smoke from the manikin. Two 800W Broncolor HMI (Hydrargyrum Medium-Arc Iodine) lamps with PAR (parabolic aluminized reflector) reflectors and MFL-UV filter glasses were placed behind and to each side of the perspex test chamber, providing sufficient light and illumination of the smoke.

Three 1/5th scaled manikins (a slim manikin in standing gesture, model #1, the same slim manikin in walking gesture, model #2 and a larger bodied manikin in standing gesture, model #3) were 3D printed at RMIT University's Advanced Manufacturing Precinct (Melbourne, Australia) and shown in Figure 3.2. The models come from our library of 3D generated CAD models which include different human manikins in various poses. The manikin selection was based on slim body build with height of 170cm. The second body was selected based on the need for a completely different shape and size to demonstrate the effects caused by different geometries. The manikins were mounted onto a rack-and-pinion travelator that moved the manikin inside a holding chamber through a sliding door and across the floor of the test chamber. The details of body geometries used in different scenarios are introduced in each chapter.

Chapter 4
Wake Flow and Particle Dispersion Induced by Rigid Body Motion

The main findings of this chapter have been published in:

- **Tao, Y.,** Inthavong, K. & Tu, J. Y. (2016). Computational Fluid Dynamics Study of Human-Induced Wake and Particle Dispersion in Indoor Environment. *Indoor and Built Environment,* 26, 185-198.
  DOI: 10.1177/1420326X16661025, ***IF = 1.181, Q2***

- **Tao, Y.,** Inthavong, K., Petersen, P., Mohanarangam, K., Yang, W. & Tu, J. Y. (2015). CFD study of human-induced wake and particle dispersion in indoor environment. *Ventilation 2015 - the 11th International Conference on Industrial Ventilation*, 26-28 Oct, Shanghai, China.

The impact of human-induced wake flow and particle re-dispersion from floors in an indoor environment was investigated by performing CFD simulations with dynamic-mesh of a moving manikin model in a confined room. The linear manikin motion was achieved by a dynamic layering mesh method to update new grids with each time step. Particle transport from the floors and its re-dispersion as tracked by the Lagrangian approach. A series of numerical simulations of three walking speeds were performed to compare the flow disturbance induced by different motion strength. The results showed that the significant airflow patterns in the indoor flow field, where identified major characters such as the upward flow in front of the body, downwash towards the back with highest velocities, the stagnant region behind the gap of legs, and the counter-rotating vortices in the wake region. The airflow momentum induced by the moving body disturbed the PM2.5 size particles from the floor to lift off and suspend due to the interaction with the trailing wake. The residual flow disturbances after the manikin stopped continued to induce the particle to spread and deposit over time. The spatial and temporal characteristics

of the particle dispersion and concentration showed that higher walking speed was conducive to reducing the human's exposure to contaminants on the height of breathing zone.

4.1 Introduction

Particle re-suspension has been identified as a factor for indoor PM transport (Zhou et al., 2011),, and this is particularly the case when human activity is considered (Oberoi et al., 2010, Inthavong et al., 2013a, Li et al., 2014, Se et al., 2010, Gao and Niu, 2005). In addition, human induced wake flow wields significant influence on particle dispersion and re-suspension affecting exposure levels and particulate matter (PM) sampling readings (Ferro et al., 2004, Mazumdar et al., 2011, Miguel et al., 2005, Inthavong et al., 2012, Wang and Chow, 2011). Flynn and Ljungqvist (1995) described human wake flow as a mixing zone characterized by vortices which entrain air into a reverse flow region. Early experimental studies investigated the effects of airflow patterns around manikins and its effect on contaminant concentrations (Heist et al., 2003, Johnson et al., 1996). Numerical studies also visualised distinct wake regions and unsteady vortex shedding from flow over static bodies (Murakami et al., 1999, Edge et al., 2005, Ge et al., 2013). However, representing a moving manikin with steady flow over a stationary manikin neglects any flow disturbance caused by the manikin acceleration and deceleration.

Recently a growing number of studies have laid emphases to the effects of human motion in the indoor environments such as hospital wards and clean rooms. Experimental studies examined the motion-induced wake patterns and their effects on contaminant distribution (Matsumoto and Ohba, 2004, Poussou and Plesniak, 2015, Bjørn and Nielsen, 2002, Han et al., 2015). Compared to experimental studies, Computational Fluid Dynamics (CFD) approaches have become more popular in studying indoor air flows (Heschl et al., 2013, Heschl et al., 2014), the human-induced wake flow (Choi and Edwards, 2012) and indoor airborne particle dispersion (Inthavong et al., 2009, Li et al., 2012), owing to its advantages of low-cost and powerful visualisation capabilities. CFD methods have been able to qualitatively predict the characteristic of wake flow induced by obstacle motion (Brohus et al., 2006), and the human induced airflow and contaminant transport (Poussou et al., 2010).

The computational Eulerian or Lagrangian methods are often used to simulate the different types of contaminant transport. Hang et al. (2014) found that the concentration of tracer gases on the body was considerably influenced by body motion and ventilation conditions. Wu and Gao (2014) observed distinct vortices in the wake region of a moving body under thermal conditions, and analysed the dispersion of gaseous contaminant emitted from the body. Wang and Chow (2011) found that a faster human walking speed could effectively reduce the transport or suspension of contaminants for cough droplet dispersion. Choi and Edwards (2012) used the Immersed Boundary Method and found that a faster walking speed resulted in reduced mass transport from the contaminated room into a clean room.

Numerical studies of contaminant dispersion with human-induced wake flow mostly considered the emission of pollutants from objects and the particle-laden flow in compartments. In comparison, re-suspension of settled dust has only been discussed in mathematical models (Qian et al., 2014, Ferro et al., 2004); while the inclusion of human movement is scarcely investigated. Floors are an important reservoir of human-associated bacteria, and the re-suspended floor dust caused by human walking has become an important contributor to contaminant concentrations (Goldasteh et al., 2014, Hospodsky et al., 2012, Tian et al., 2014) and experimental studies have confirmed the occurrence of particle resuspension caused by human activities. Qian and Ferro (2008) used optical particle counters in a full-scale test chamber and showed that 'heavy and fast' walking produced higher resuspension rates than less active walking. This was attributed to a combination of increased pace, increased air swirl velocity, and electrostatic field effects established by the walking. Similarly studies investigated human interactions with floor type (You and Wan, 2015), dust type and contaminant concentration in dust loads (Gomes et al., 2007). Thus, it is necessary to investigate the human-induced wake flow and its influence on the re-suspension of settled particles. In addition, an anthropomorphic geometry can provide more accurate results than simple geometries (Gao and Niu, 2005). Compared to simplified geometries which were commonly used to represent the human body in previous studies, there is a lack of studies regarding a realistic human manikin geometry.

To better understand the effects of human-induced wake flow on particle dispersion and occupant exposure to contaminants, this chapter presents CFD

simulations using a realistic manikin model under various constant walking speeds. A dynamic mesh model was used for moving the manikin and the particle modelling used the Lagrangian approach. The impact of human-induced wake flow on particle dispersion from floors and the distribution of particle concentration in the flow domain were analysed.

4.2 Numerical Procedures

4.2.1 Cylinder Geometry for Model Validation

The fluid dynamics of wake flow around human body comply with the principle of the boundary layer separation when air flows over bluff bodies such as mounted vertical finite cylinders. Research into the flow field around fixed cylinders have provided insight into the major characteristics of bluff body aerodynamics and identified the main flow features of vortices such as

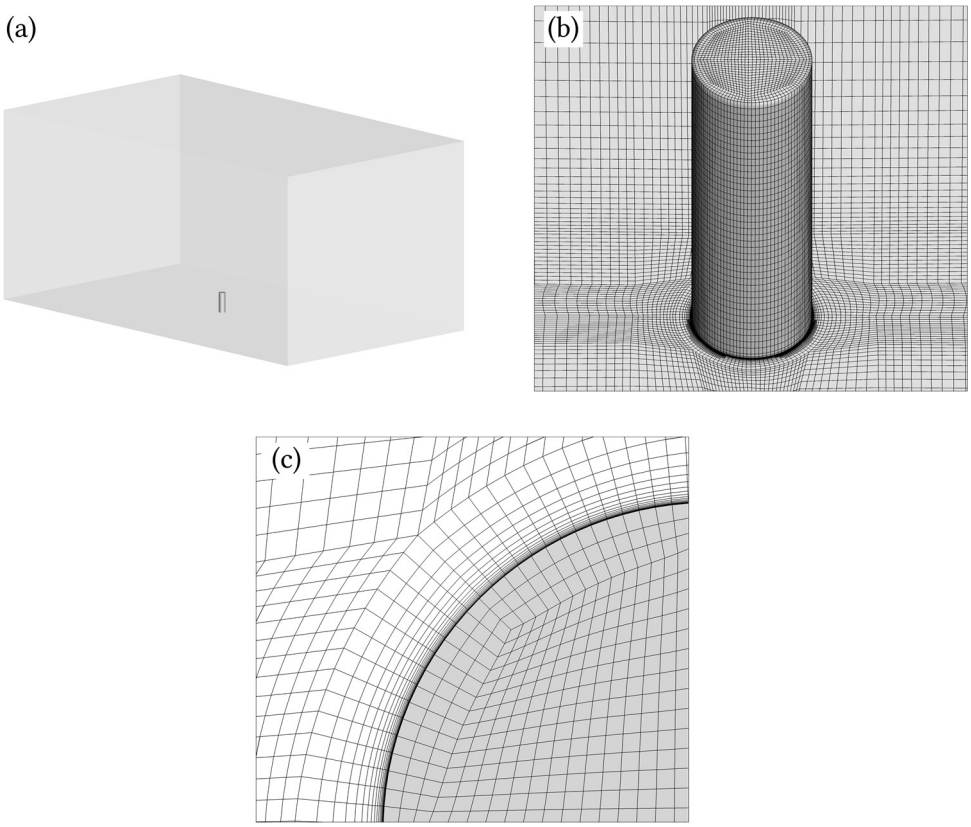

Figure 4.1 Computational mesh for the mounted vertical cylinder (a) computational domain, (b) grids around the cylinder and (c) grids on the prism layer.

downwash flow and recirculation regions extending downstream behind the bluff body (Kawamura et al., 1984, KrajnoviĆ, 2011, Wang and Zhou, 2009). To validate the numerical modelling accuracy, simulations of near wake flow around mounted vertical cylinders were conducted and validated against PIV measurements by Rostamy et al. (2012). The computational domain was a cuboid with dimensions of 1.96m × 0.91m × 1.13m. A circular cylinder with a diameter of 31.5mm and an aspect ratio (H/D) of 3 was mounted at a distance of 900mm from the leading edge (Figure 4.1a). The vertical cylinder has similar aspect ratio with our manikin model (discussed later). The free stream velocity was U = 20 m/s, turbulence intensity less than 0.6%, giving a Reynolds number of 42000 based on the cylinder diameter.

To solve the boundary layer separation in the viscous sub-layer on the cylinder surface, 10 layers of prism cells were extruded from the surface with an initial grid spacing of 1×10^{-4} m (Figure 4.1b and c). This produced a dimensionless wall distance ($y+$) of less than 5 to keep the first grid point within the viscous sub-layer and ensure a sufficient number of grid points within the

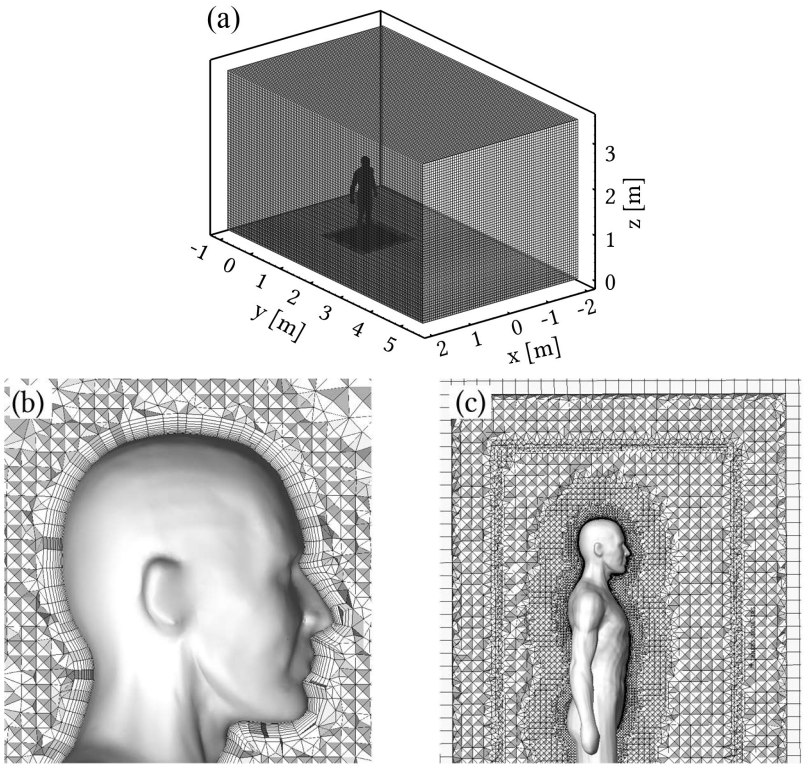

Figure 4.2 (a) Computational domain of the room; (b) Prism layers and mesh generation around the manikin surface and (c) hex-core cell elements used in the room environment

buffer region where turbulent production rapidly increases. The $y+$ term is defined as $y+ = \mu_\tau v/\upsilon$, where y is the distance normal to the wall, ν is the kinematic viscosity, and μ_τ is the friction velocity defined as $\mu_\tau = \sqrt{\tau_w/\rho}$, where τ_w is the wall shear stress and ρ is the air density. Structured hexahedron meshes with total grid amount of 3.1 million were generated. The flow domain was calculated by applying identical ambient flow conditions with the experiment data, and the time step size for the unsteady process was 1×10^{-3} sec.

4.2.2 Indoor Room Model Geometry

The computational domain was a room with dimensions of 4m (x-coordinate) ×6.5m (y-coordinate) × 3.0m (z-coordinate). A manikin model (1.7m-height, 0.58m-width) was located at x = 0 m, y = 0 m, facing the $+y$ direction with a distance of 1 meter to the back wall (Figure 4.2a). The manikin moved at a constant speed of 0.4m/s, 0.8 m/s, or 1.6m/s for a distance of 3 meters. Taking the body width as the hydraulic diameter, the corresponding Reynolds numbers were between 15,000, 31,000 and 62,000. Unstructured tetrahedral cells and prism layers were generated around the manikin surface, while a hex-core filled inside the room Figure 4.2b, and c. To capture boundary layer separation around the manikin, 10 prism layers were generated on the manikin surface to keep the dimensionless wall distance $y+ < 5$. The layering mesh method was used to update the moving manikin grid at each new time step.

A grid independence study was conducted by reducing individual cell spacing by a factor of 1.3 consecutively and plotting the velocity magnitude along a horizontal and vertical line behind the manikin (Figure 4.3). The horizontal line was 0.25m behind the body at a height of 1.0m (labelled line-1), while the vertical line was centred and 0.25m behind the body (labelled line-2). We started with a grid of 0.9 million and subsequent grids of 1.7 million, 3.6 million, and 6.9million were made. The velocity profiles showed convergence between mesh size 3.6 million and 6.9 million and for computational efficiency and accuracy, the 3.6-million model was chosen for the remainder of this case.

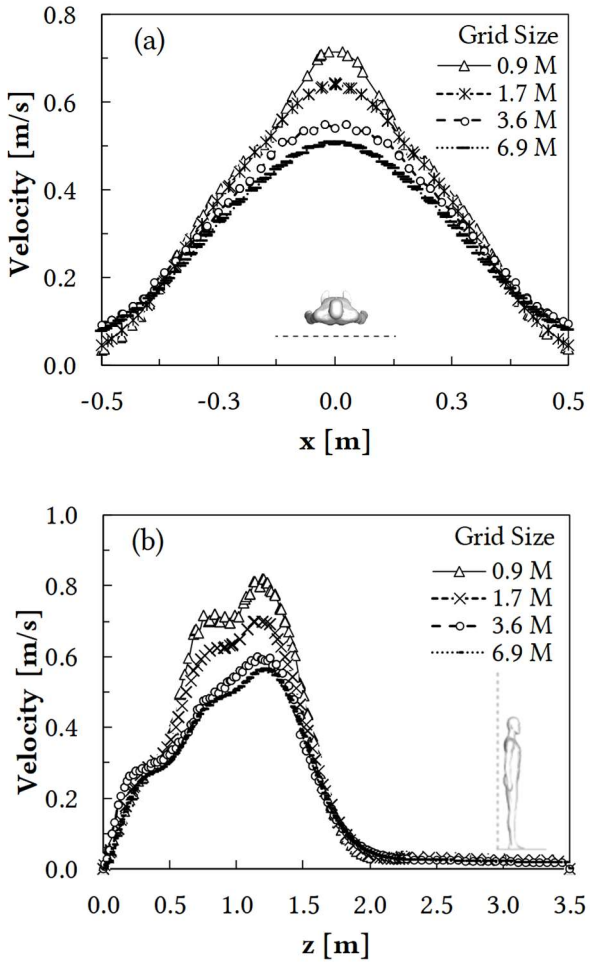

Figure 4.3 Mesh independence study: comparisons of velocity simulation results of four grids: (a)velocity profile on line-1 (horizontal); (b)velocity profile on line-2 (vertical).

4.2.3 **Airflow Modelling**

For a 3-dimensional time-dependent incompressible flow, the Reynolds-average Navier-Stokes equations were solved for the fluid phase. The general transport equation for continuity, momentum and turbulent quantities are given as follows:

$$\frac{\partial \phi}{\partial t} + \frac{\partial (u_i \phi)}{\partial x_i} = \frac{\partial}{\partial x_i}[\Gamma \frac{\partial \phi}{\partial x_i}] + S_\phi \tag{5.1}$$

where, ϕ represents the general variable, u_i is the velocity vector, Γ represents the diffusion coefficient and S_ϕ represents source terms. The human motion in the computational domain was achieved by a laying dynamic mesh.

The conservation equation for a general scalar with a moving boundary can be written as:

$$\frac{\partial}{\partial t}\int_V \rho\phi dV + \int_{\boldsymbol{A}} \rho\phi\left(\vec{u} - \vec{u}_g\right)\cdot d\boldsymbol{A} = \int_{\boldsymbol{A}} \Gamma\nabla\phi \cdot d\boldsymbol{A} + \int_V S_\phi dV \qquad (5.2)$$

where, ρ is the fluid density, $\vec{u}$ is the flow velocity vector; $\vec{u}_g$ is the grid velocity of the moving mesh, $\boldsymbol{A}$ is the boundary of the control volume V, Γ is the diffusion coefficient, S_ϕ is the source term.

In this chapter, model validation compared the RNG k-ε model with the Shear Stress Transport (SST) turbulence model. The RNG k-ε model has shown high accuracy, computing efficiency and robustness for modelling indoor environments (Zhang et al., 2007). The SST model is a blended k-ε/k-ω model proposed by Menter (1994) which predicts free stream turbulence quantities with the k-ε model, and predicts more accurately boundary layer separation flows in adverse pressure gradients with the k-ω model. The commercial CFD code ANSYS-Fluent was used for the modelling and the discretization involved the QUICK scheme for momentum, and the SIMPLE algorithm for pressure-velocity coupling. The second-order upwind scheme was used for the convection and diffusion terms. The time step size was set as 0.005s and the mesh was updated at each time step matching the manikin movement.

4.2.4 **Particle Modelling**

The Lagrangian particle trajectory-tracking model, based on the particle force balance equation, was used to track particle transport and its deposition, given as:

$$\frac{\partial u_p}{\partial t} = F_D\left(u - u_p\right) + \frac{g(\rho_p - \rho)}{\rho_p} + F_x \qquad (5.3)$$

where $F_D(u - u_p)$ is the drag force per unit particle mass and F_D is defined using the spherical drag law; u is the fluid phase velocity and u_p is the particle velocity; ρ is the fluid density and ρ_p is the particle density. F_x is additional forces and the major particle driving force considered for micron particles in this study was the Saffman lift force (Chang and Hu, 2008).

To examine the effects of human motion on indoor particle dispersion, 2.5μm particles (otherwise known as $PM_{2.5}$ where PM = particulate matter) were distributed on the floor centred at y = 1.5m, with surface area of 0.5m × 0.5m. The particle mass was set to 120mg. The boundary conditions for the particles on the human surface and walls were set as trap which assumed that the particle tracking ceased once the particle touched the wall surface.

The re-suspension factor (R) was used to describe the level of re-suspension of particles, defined as $R = C/L$ (Qian et al., 2014), where C is the airborne concentration of indoor PM (particles per m^3), and L is the concentration of surface-bound particles in the indoor flooring (particles per m^2). In our simulations, only re-suspension induced by walking speeds was compared, while the adhesion of particles to surfaces was not considered, which could affect the result comparisons with experimental data of real situations.

4.3 Results and Discussion

The numerical results of the phase-average velocity field on the centre plane and the measured data are compared in Figure 4.4. The immediate downwash flow that originated near the free end and persisting in the stream-wise direction was observed from the simulated results. A tip vortex below the free end and the other near the cylinder-wall junction were captured. Minor differences occurred at the locations of the saddle points related to the two vortices, and the prediction in the u and w velocity components. The RNG model showed better performance over the $k\omega$-SST in predicting the velocity distribution in the near wake region. Overall, the reasonably good agreement concluded from the comparisons showed that the proposed numerical approach was reliable for the wake flow prediction behind a bluff-body with good accuracy.

4.3.1 Air Flow Patterns of the Human Induced Wake Flow

To compare the unsteady aerodynamics under different walking speeds, the non-dimensional time is defined as $T = t/(S/V)$, where t is the walking time non-dimensionlized by the walking distance S = 3m under various walking speed (V). Thus, for all the testing condition, the manikin came to a stop at dimensionless time T = 1, and the residual wake was examined until T = 4.

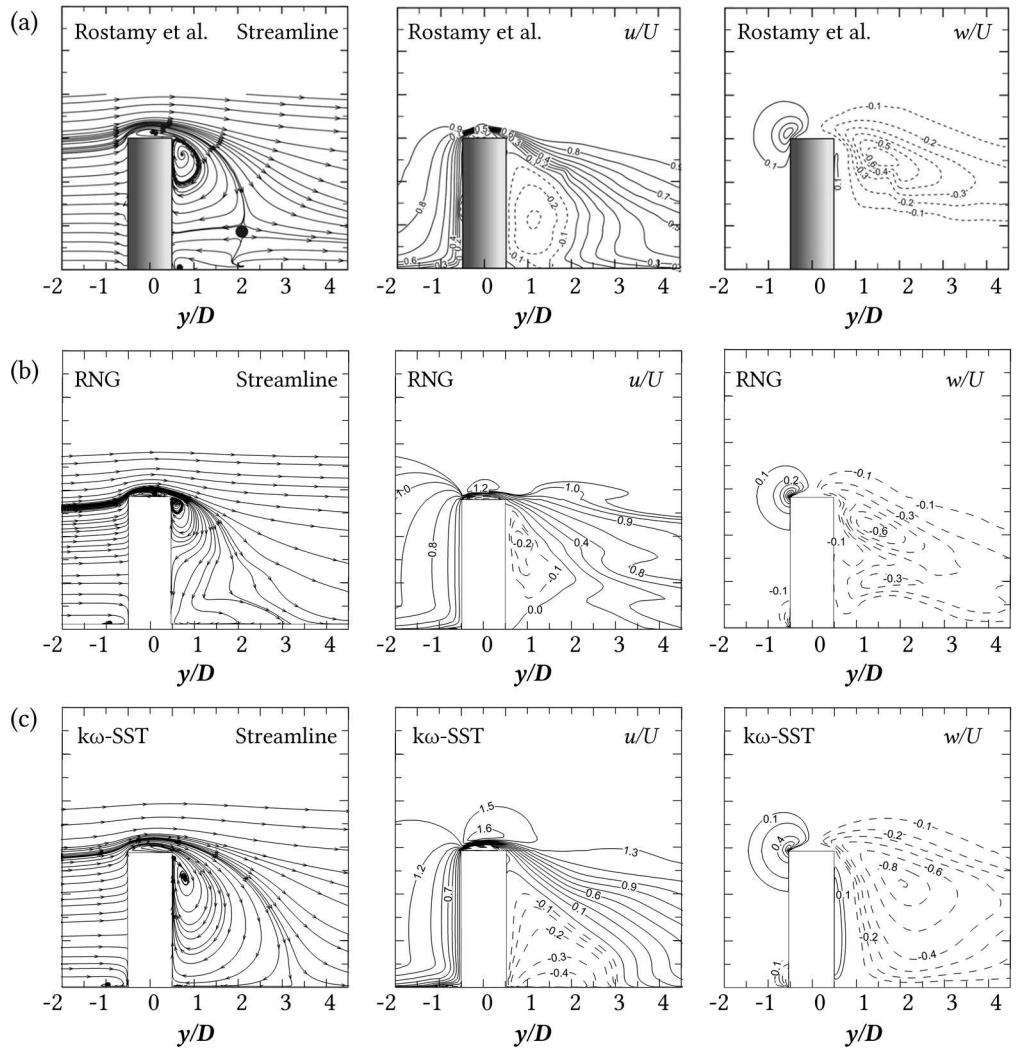

Figure 4.4 Results comparison between the CFD simulations and PIV measurement data on the centre plane of (a) streamlines (b) normalized u-velocity component (c) normalized w-velocity component.

The fluid dynamics of the human wake are shown through plots of the velocity vectors on the vertical middle plane (yz = 0m) and the vertical plane through the right leg (yz = 0.11m) under a walking speed of 0.8m/s at the dimensionless time of T = 0.33, T = 1 (stopped moving) and T = 2, representing the manikin walking distance of 1m, and stopping at 3m (Figure 4.5). The velocity field was non-dimensionalized by the walking speed. The disturbed air formed a triangular region behind the body and the wake size grew during walking. After the manikin stopped, the wake shrunk while the disturbed airflow kept moving forwards due to its inertia.

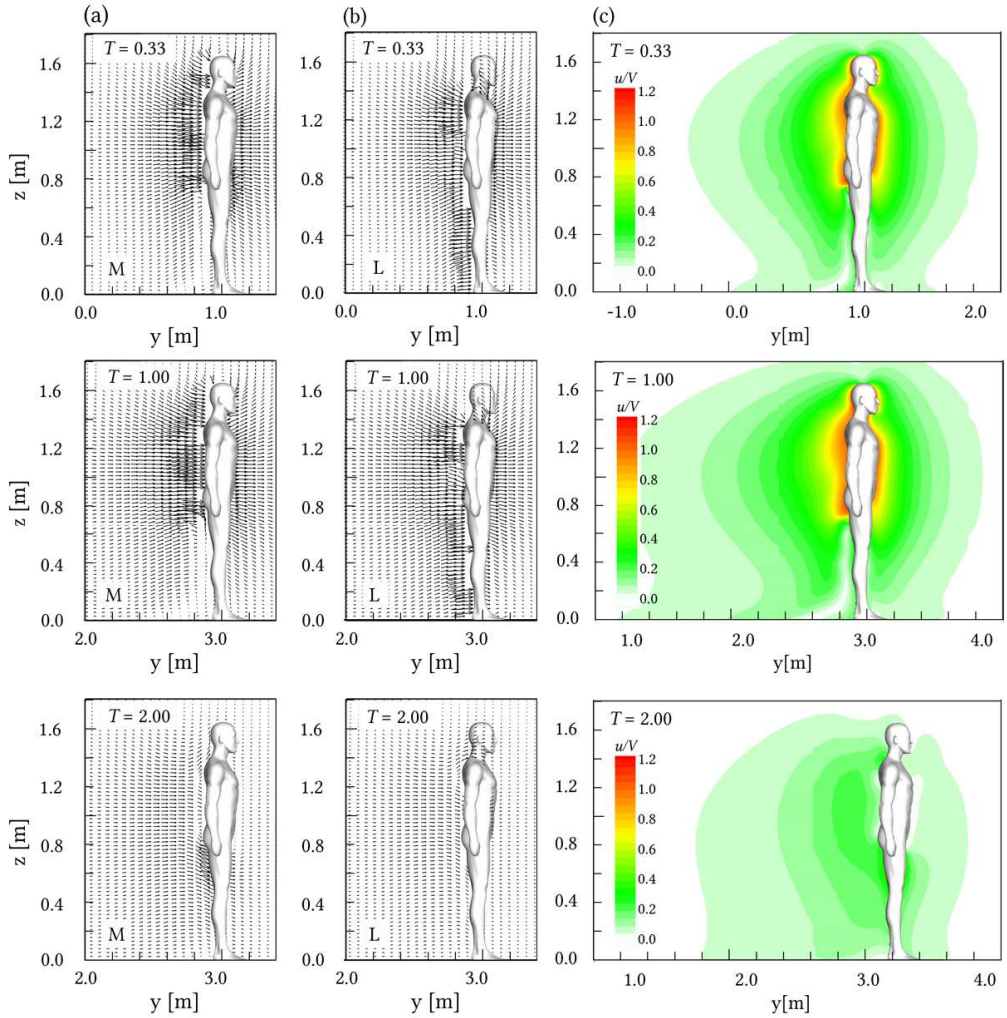

Figure 4.5 Flow field comparisons at dimensionless time T = 0.33, T = 1 and T = 2: (a) velocity vectors on the vertical middle plane ((M) yz=0m); (b) velocity vectors on the vertical plane through the right leg ((L) yz=0.11m); (c) velocity field non-dimensionalized by the walking speed (V = 0.8m/s)

Streamlines originating from the body were used to determine the local flow behaviour around the manikin (Figure 4.6). During walking, the airflow behaviour changed at different heights of the body. The disturbed air near the upper body generated an upward flow in the moving direction and a significant downwash towards the back. The highest velocity in the flow field was approximately 1.2 times the walking speed at the region near the back and the buttocks. Due to the pressure increase at the front face and the pressure drop at the rear during the motion in the confined space, the airflow was driven from the front body towards its rear. When viewed from the right-hand side of the body to the vertical middle plane, a spherical-type anti-clockwise

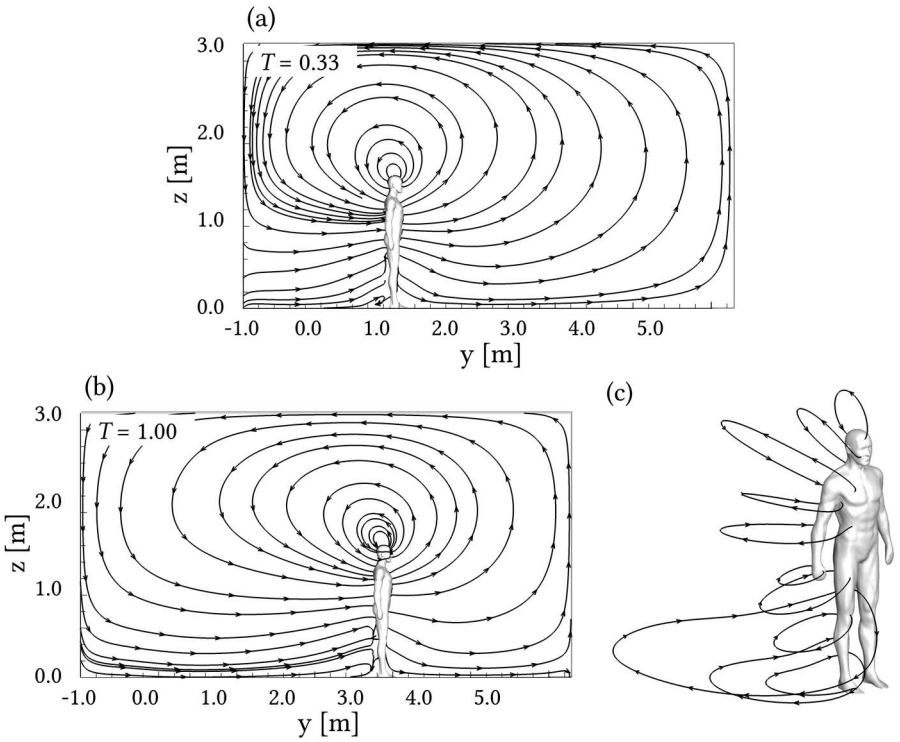

Figure 4.6 Streamlines on the vertical mid-plane at (a) T = 0.33, (b) T = 1 and (c) the 3D view of the volume streamlines during the walking process under the walking speed of 0.8 m/s

recirculation region was formed immediately above the head, and with the continued motion the recirculation region stretched downwards (Figure 4.6).

At the lower part of the body, there was a significant jet protruding from the thigh gap, but after that it counteracted against the downwash from the upper body, thus forming a stagnant region behind the lower part of the leg. The velocity field on the vertical plane through the leg showed similar flow characteristics (Figure 4.5b). In the front region of the legs, the disturbed air moved forward and downward towards the ground, which would wield influence on the dispersion of floor contaminants. The vectors generated at the feet showed an upward trend that would induce the particles to lift off the ground and move upwards.

Figure 4.7 shows contours of vorticity ω_x magnitude in the vertical mid-plane (yz = 0m) at non-dimensional time of T = 0.33, 1 and 4. A strong negative vorticity concentration convected off from the head and shoulders, indicating an anti-clockwise circulation region at the back of the upper body where the significant downwash occurred. Besides, a strong positive vorticity protruding

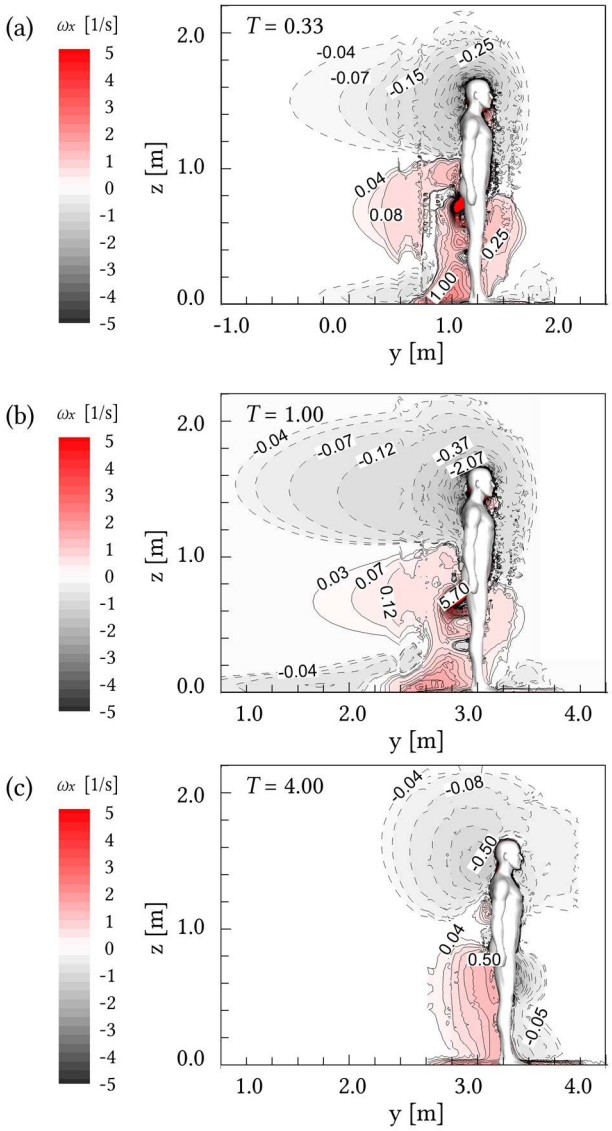

Figure 4.7 Vorticity ω_x magnitude on the vertical middle plane under a walking speed of 0.8m/s at dimensionless time (a) T=0.33; (b) T=1 and (c) T=4.

from the gap of the legs identified a clock-wise circulation against the downwash circulation behind the upper body. The counter-rotating vortex shedding then stretched downwards into the wake region. The vorticity contour showed consistency with the flow field analysed earlier. At the back of the body, the downwash counteracted with the jet between legs thus inducing the jet to flow downwards and re-circulate in a clockwise direction, which further enhances particle re-dispersion once the manikin walks pass the source. The upper flow circulation also enhances the particles to disperse higher. When the manikin stopped moving, the vortices gradually descend towards the ground through the gaps of legs into the front direction.

Overall, airflow generated by the upper body flowed upward in the front region and downward towards the back. Despite the lateral airflow induced by the lower body due to the suppression from the upper flow, the airflow generated by the lower legs and foot had a substantial effect on inducing the particles to flow upwards. After the manikin stopped, the flow towards the back changed into an upward flow over the head and a downward flow through the gap of the legs. The airflow characteristics under different walking speeds would induce different particle dispersion results.

4.3.2 Effects of Human Motion on Particle Dispersion

The suspended particle trajectory (Figure 4.8), mass concentration (Figure 4.9) and suspension factor (Figure 4.10) under the same non-dimensionalized time are compared. The re-suspension factor $R = C/L$ (Qian et al., 2014) was calculated at several certain time steps during walking and after the motion stopped. C, the airborne concentration of indoor PM, was obtained from the particle mass at the current time step (reported by the software FLUENT) divided by the space volume; and L, the concentration of surface-bound particles in the indoor flooring, was calculated from the mass of particle source divided by the surface area of the ground. As the manikin moved ($T = 0.33$), some of the particles lifted from the floor upwards and slightly forward. This was due to the forward and downward trend of airflow induced by the lower part of legs, thus starting suspension before the manikin had reached the initial location of the particle source. As the manikin moved passed the particle source, the upward flow in the circulation region behind the legs continued to take the particles towards the back of legs, while the downwash at the back helped to contain the particles to a smaller region. At the same time, some particles in the front of the body had already ascended to the breathing zone where the airflow generated by the upper body flowed upwards, thus resulting in an adverse situation of high particle concentrations in the breathing zone.

For the same walking distance, a lower walking speed (0.4m/s) resulted in reduced suspension but more scattered dispersion. The particle clusters with concentration above 3mg/m^3 ascended into the breathing zone and even higher beyond the head when the manikin walked past the particle source. For a faster walking speed (1.6m/s) nearly twice the amount of suspension was generated due to higher momentum (Figure 4.10a), but the particles were less

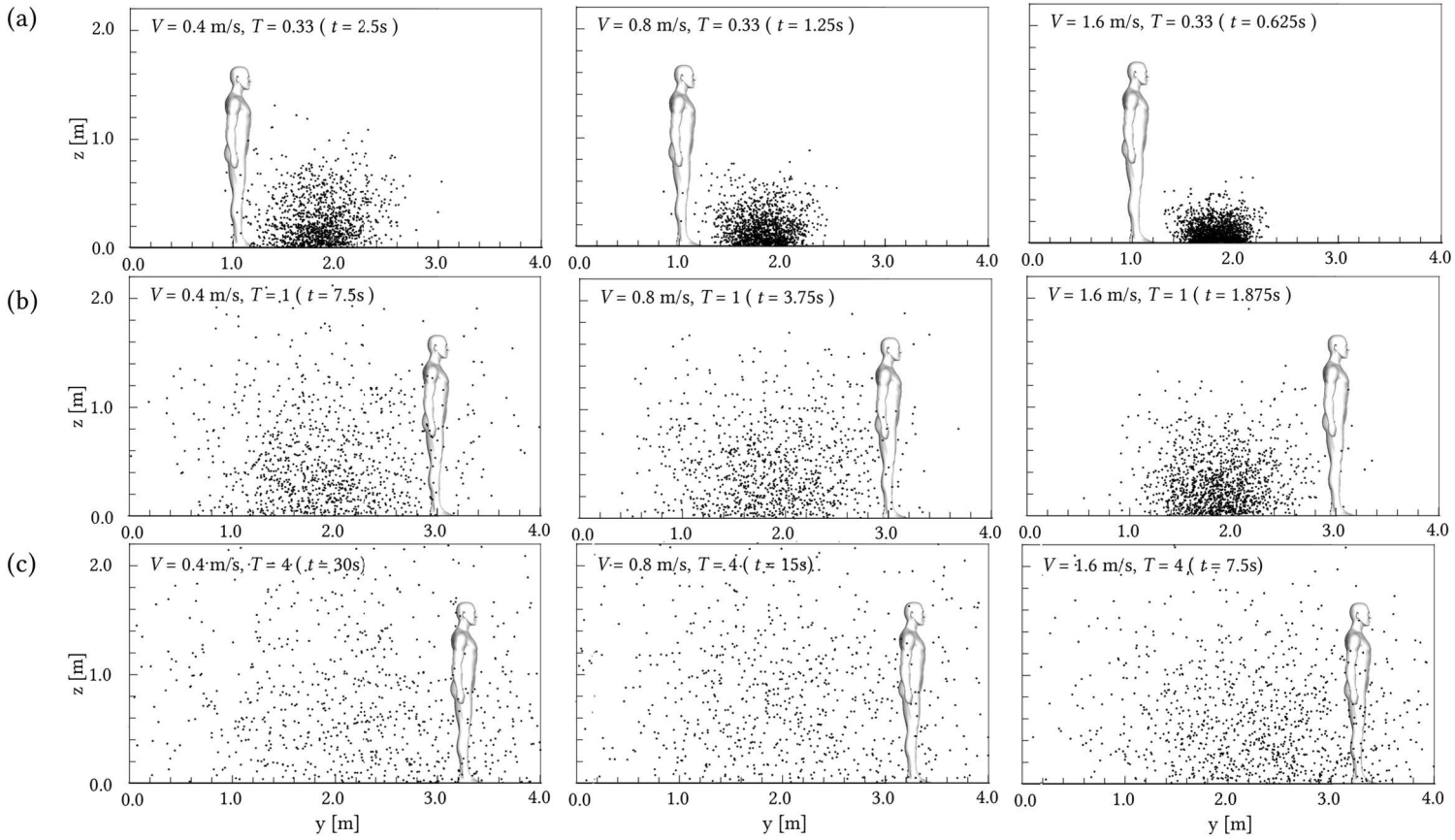

Figure 4.8 Particle trajectory under 3 walking speeds (0.4m/s, 0.8m/s and 1.6m/s): (a) walked for 1m (T = 0.33); (b) walked for 3m (T = 1 and motion ceased); (c) stopped until dimensionless time T = 4.

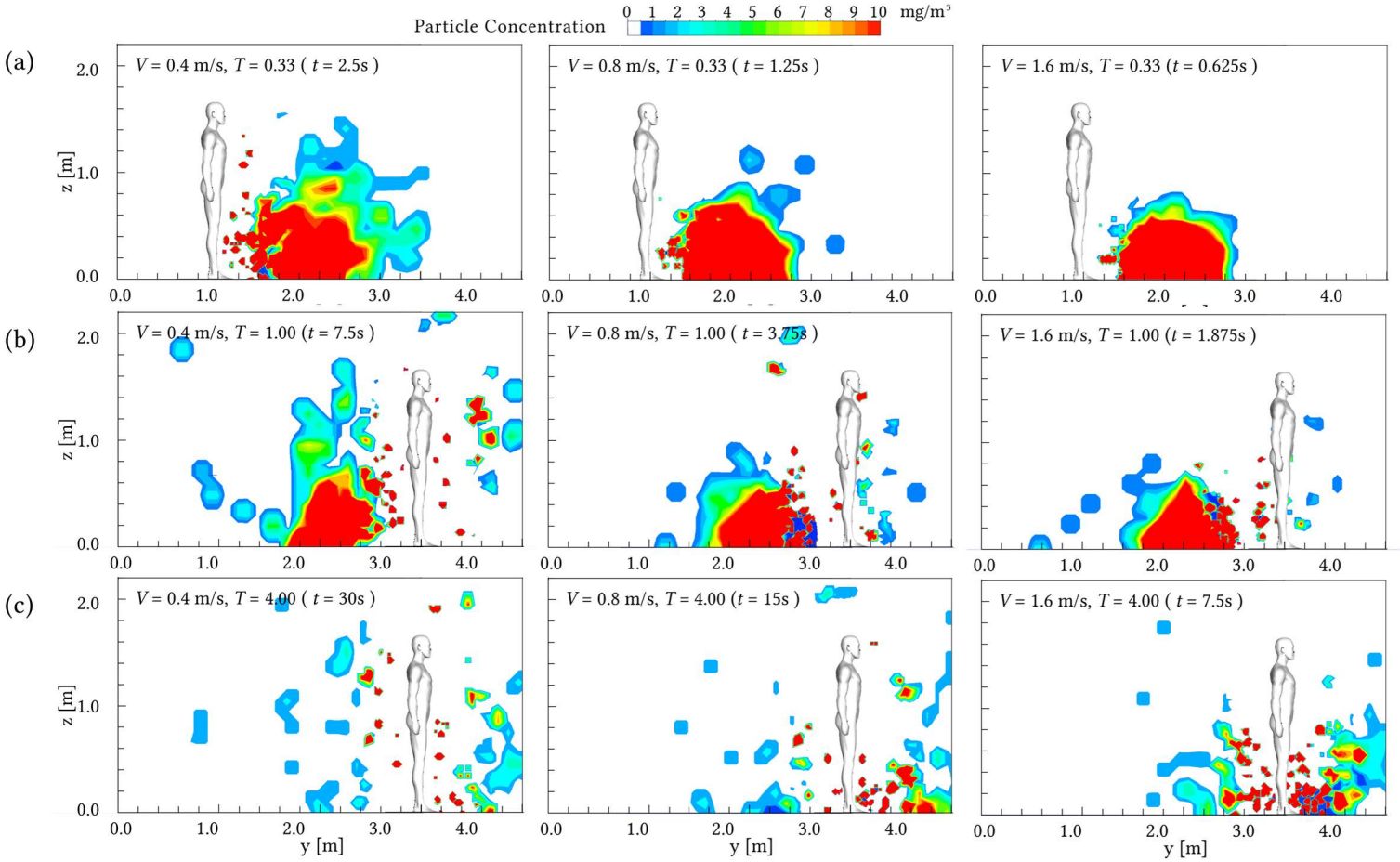

Figure 4.9 Particle concentration contours on the vertical middle plane under 3 walking speeds (0.4m/s, 0.8m/s and 1.6m/s): (a) walked for 1m (T = 0.33); (b) walked for 3m ((T = 1 and motion ceased); (c) stopped until dimensionless time T = 4..

scattered when the manikin passed the same position. High concentration of particles was found at the leg level and less ascended to the breathing zone under a higher walking speed (Figure 4.9). This was because within the same walking distance, a walking speed of 0.4 m/s allows 4 times the duration of particle-flow interaction compared to a walking speed of 1.6 m/s, thus dispersing more widely with sufficient contact between the disturbed air and particles. However, under a faster walking speed, the manikin escaped the contaminated area quicker before the particles could ascend to the breathing level. With the particle source left behind, the stagnant region and downward airflow at the rear of the body helped to contain the particle suspension, therefore avoiding high exposure to contaminants.

After the manikin stopped at dimensionless time $T = 1$, the wake continued to propagate and transport the particles forward and consequently the particle

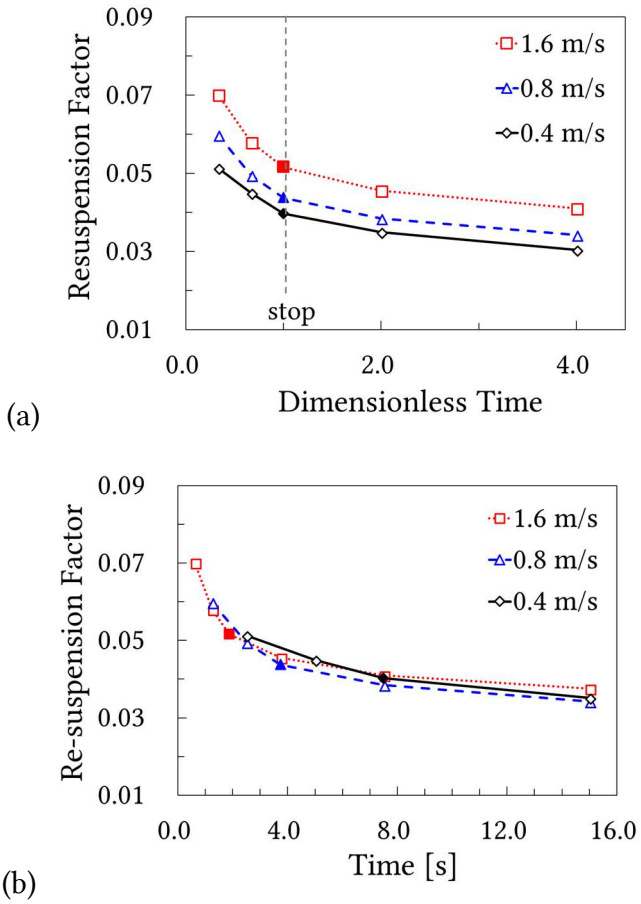

Figure 4.10 Comparisons of particle re-suspension factor under 3 walking speeds (0.4m/s, 0.8m/s and 1.6m/s) over (a) dimensionless time (b) real time (solid markers indicated the stop of motion)

dispersion remained influenced by the residual wake flow. Up to the time T = 4, the particle mass concentration near the body decreased significantly. Some dense particle clusters were assembled near the front of the legs as the vortices moved forward through the leg gaps. The particles then began to settle due to gravitational effects. However, the time for particles to deposit from flow disturbances took much longer time than the recovery of airflow velocities.

Figure 4.10a shows the comparison of particle suspension factors under three walking speeds (0.4m/s, 0.8m/s, 1.6m/s) at the same dimensionless time. The trend reflected a higher suspension amount under faster walking speeds, and similar trend in the depletion of contaminant concentration with time. During manikin motion, the suspension factor dropped rapidly owing to the forced interaction between the body and particles which led to more particle capture by the surfaces and the ground. After the manikin stopped, the particles were transported by the residual airflow thus slowing down any further deposition. When the suspension was compared under real time (Figure 4.10b), the suspension factor for the three walking speeds showed minor differences. A quicker deposition occurred for a faster walking speed during walking. For a walking speed of 1.6m/s, the manikin induced a substantial suspension at the beginning and quickly dropped the suspension factor by 28.5% within 1.25 seconds. With a lower walking speed of 0.4m/s, the reduced particle deposition resulted in a slower decrease of suspension factor by 25% within 5 seconds during walking, thus having more time for particles to scatter widely.

Overall, the suspension induced under various walking speeds was related to both the strength and interacting time between the manikin and particles. The quicker the human walked pass the contaminant resource, the lower height that contaminates ascended and safer from the exposure to contaminate.

4.4 Conclusion

This chapter presented unsteady simulations of the wake flow induced by a moving manikin in a confined room and its influence on particle dispersion from floors was discussed. The simulated flow field showed a recirculation region after the free end of the head, an upward flow in front of the upper body and a downwash flow at the back where highest velocity in the flow field occurs. At the lower part of the body, the wake flow gradually became

horizontal due to the suppression by the airflow from the upper body. But the airflow induced by the lower part of the legs induced an upward trend of airflow, which became the major contributor for particles to lift off the ground. A pair of counter-rotating vortices was formed behind the moving manikin, one convecting off the head and another protruding from the gap of legs and extending downwards in the wake region. When the manikin stopped walking, the residual flow disturbances diminished downward and forward.

The particles on the floors were significantly disturbed by the motion induced flow, thereby lifting off the ground and dispersing into the ambient air. The slower walking speed induced less amount of suspension when the manikin walked through the same position, but the particles were more scattered within the indoor space due to a longer period of interaction between the body and particles, thus generating high concentration of particles near the breathing region which would cause hazard inhalation issues. When the manikin walked through more quickly within the same distance, more particles lifted off the floor, the dispersion was less dispersing, and particles ascended to a lower height. Comparisons between walking speeds showed a higher walking speed was conducive to avoid high particle concentration in the inhalation region owing to the instant contact between the body and particles. When the manikin stopped moving, particles continue to spread into the ambient air and deposit towards the lower part of the front body due to the residual flow disturbances, and the particle concentration gradually diminished over time. This chapter provided some insight into the flow and particle dynamics. The particle suspension and its factor was significantly influenced by the moving manikin.

Chapter 5

Comparisons of Wake Flow Between Swinging Motion and Rigid Motion

The main findings of this chapter have been published in:

- **Tao, Y.,** Inthavong, K. & Tu, J. Y. (2017). A Numerical Investigation of Wind Environment around a Walking Human Body. *Journal of Wind Engineering and Industrial Aerodynamics*, 168, 9-19.
  DOI: 10.1016/j.jweia.2017.05.003, ***IF = 2.689, Q1***

- **Tao, Y.,** Inthavong, K. & Tu, J. Y. (2016). A numerical investigation of wake flow characters during human gait cycle in the indoor environment. *20th Australasian Fluid Mechanics Conference (AFMC)*, 5-8 Dec, Perth, Australia.

Human-induced wake flow characteristics and its interaction with thermal conditions was investigated by performing CFD simulations with dynamic-meshing of a moving manikin model. The manikin motion with and without swinging limbs was achieved by the re-meshing method to update the grid with each time step. The results focused on determining what discrepancies are produced in the flow field by a simplified geometry in the form of a cylinder, swinging limbs and thermal conditions; and whether such assumptions can be made for larger multi-body analysis. Using a cylinder showed differences in the velocity field behind the head and leg gap. The flow field between the rigid motion and swinging limb motion, showed significant discrepancies which corresponded to the gait phase. There were increased airflow disturbances at the hands and ankles (furthest body parts from the pivot point). The influence of thermal plume on the wake flow was minor during walking motion because of the walking speed of 1.2m/s which dominated the buoyant thermal plume velocity. However, after the manikin stopped moving the thermal plume velocity became comparable to the residual wake.

5.1 Introduction

Wind flowing over a human body influences thermal comfort (Sasaki et al., 2000) and pollutant exposure in outdoor conditions. Its fluid dynamics have primarily been investigated by considering a stationary human body exposed to an oncoming wind (Inthavong et al., 2013a, Se et al., 2010, Irwin, 2008, Murakami and Deguchi, 1981, Inthavong et al., 2012, Li et al., 2014). The induced wake exhibits similarities to boundary layer separation of flows over bluff bodies, where a mixing zone of vortices entraining air into a reverse flow region is formed (Flynn and Ljungqvist, 1995, Mahjoub Said et al., 2008, Zhang et al., 2016). Therefore, simplified geometries such as vertical finite cylinders and cuboids were used as substitutes for human bodies (Poussou et al., 2010, Thatcher et al., 2004). This leads to discrepancies in flow features due to the simplified geometry. For example, when legs are considered as two cylinders instead of one single thick cylinder, there is increased mixing in the wake, influenced by the gap width (Edge et al., 2005, Flynn and Ljungqvist, 1995). Another issue that arises with flow over a stationary manikin is the flow separation at the feet which neglects flow disturbances caused by the manikin motion; thus, the near wake characteristics during walking are only partially represented.

A second factor to consider is the effects of heat transfer leading to thermal plumes from the human body. Murakami et al. (1999) investigated the thermal and dynamic effects of 0.25m/s and 2.5m/s wind on stationary bodies. Velocity and temperature fields around the body revealed a thin layer of warm rising air around the body under a stagnant or weak wind environment; but this disappeared when the wind velocity increased. Combining a wind tunnel experiment and CFD, Li and Ito (2014) and Ono et al. (2008) showed thermal plumes emitting from around a human body in an outdoor environment. Therefore, the effect of heat transfer is an important component for wind flow over a human body.

Flow measurements of moving bodies presents significant challenges due to set up, large scales, and its dynamic nature. There are a few studies that have investigated the fluid dynamics from a moving manikin including: Inthavong et al. (2017) who investigated an isothermal $1/5^{th}$ scaled rigid moving manikin model; Luo et al. (2015) and Oliveira et al. (2014) who investigated natural and

forced convection heat transfer from a moving thermal manikin in rigid motion. In the thermal model studies, the heat transfer coefficient increased as a power exponent function with increase of the moving speed.

Recently a growing number of computational studies have laid emphases on the effects of human activity on the wake dynamics. CFD with dynamic mesh advances the modelling capability to capture transient effects of manikin motion. This was used to qualitatively capture the wake flow from moving blocks (Brohus et al., 2006, Poussou et al., 2010). Realistic anthropomorphic manikins have also been used as they provided more realistic results in the near-body regions (Choi and Edwards, 2012, Gao and Niu, 2005, Hang et al., 2014, Mazumdar et al., 2010, Oberoi et al., 2010, Wu and Gao, 2014, Tao et al., 2016). While these studies are gradually developing its complexity by being integrated with particle modelling for air quality assessments, some characteristics of the dynamic wake induced by the walking motion that is modelled, remains unclear. For example, there are differences in flow field due to a moving rigid body motion, and that of a swinging human gait cycle, and in combination with a thermal plume. These processes are important for understanding exposure to airborne contaminants which can be prevalent in the urban environments (e.g. pollutants, and exhaust fumes in pedestrian / urban streets).

This chapter is to understand the fundamental fluid dynamics of the wake flow, in particular, for flow separation over bluff bodies in motion. The investigations into the motion-induced wake flows were closely related to practical applications such as wind turbines (Abdelsalam et al., 2014, Lam and Peng, 2016) and pollutant transport induced by vehicle motions in tunnels (Chung and Chung, 2007, López González et al., 2014) and urban street canyons (Solazzo et al., 2008). The wake flow generated by human activities highly interests the assessment of air quality as the human activity constitute an important factor to influence the exposure to air pollutants in both indoor and outdoor workplaces.

In this chapter, the numerical setup was first validated with experimental data of a simplified cylindrical body, before being applied to a manikin under rigid and swinging motion. Thermal and isothermal conditions were also evaluated to examine the interaction between the thermal plume and the effects of motion. The results focused on the spatial and temporal characteristics of the flow

field and vortex structures. The range and strength of the flow field around the manikin would be explored in order to show the area of disturbed airflow, where observable potentials to influence the transport of contaminants could be deduced. The thermal analysis was to address under which circumstances the thermal plume is valuable or negligible by comparing the relative magnitude between the thermal plume and the motion-induced airflow.

5.2 Method

5.2.1 Cylinder Geometry for Model Validation

To validate the numerical model setup, a transient simulation of near wake flow around a vertical cylinder was performed. The solution was time-averaged and its velocity field was compared with PIV measurements by Rostamy et al. (2012). A circular cylinder with a diameter of 31.5mm and an aspect ratio (height/diameter, h/D) of 3 is similar to the manikin model. The cylinder was placed inside a computational domain with dimensions of 1.96m × 0.91m × 1.13m. The free stream velocity was U = 20 m/s giving a Reynolds number of 42000 based on the cylinder diameter, and a turbulence intensity of 0.6% based on Rostamy et al. (2012).

To solve the boundary layer separation in the viscous sub-layer on the cylinder surface, 10 prism cell layers were extruded with a first cell grid spacing of 1×10^{-4} m. This produced a dimensionless wall distance (y^+) of less than 5 within the viscous sub-layer and ensured enough grid points within the buffer region where turbulent production rapidly increases. A structured hexahedral mesh with 3.1 million cells was generated and a time step of $t = 1\times10^{-3}$ s was used.

5.2.2 Manikin Model and Boundary Conditions

A manikin with dimensions of 1.7m-height, 0.58m-width, and aspect ratio h/D = 2.93 was placed in a computational domain of 2.6 m (x-coordinate) × 6.0m

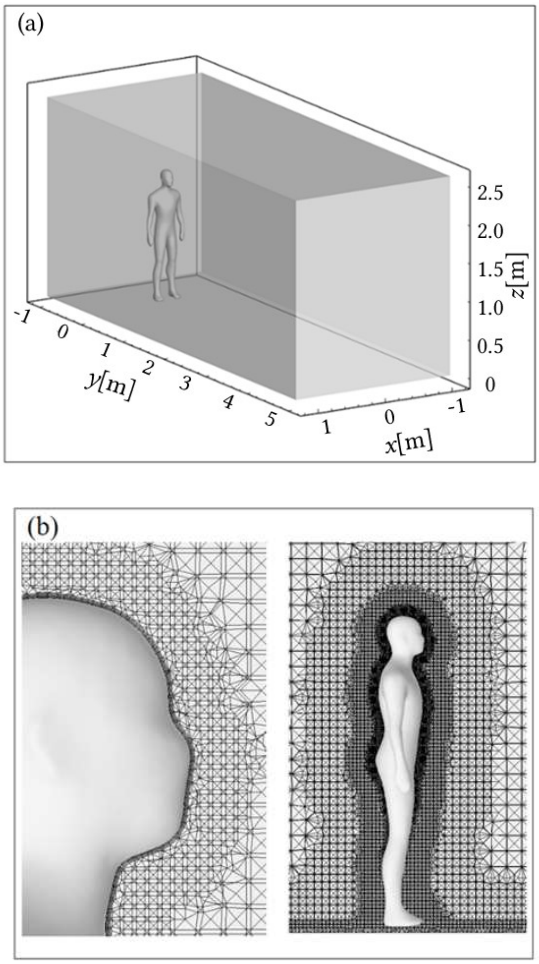

Figure 5.1 (a) Computational domain of the room, x- y- z- coordinates are in meters; (b) Prism layers and tetrahedral mesh generation around the manikin body

(y-coordinate) × 2.7 m (z-coordinate). The coordinate system located the manikin at an initial standing position at x = 0 m, y = 0 m, facing the $+y$ direction 1m from the back wall (Figure 5.1a). To capture the boundary layer separation around the manikin, 10 prism layers were generated on the manikin surface to keep the dimensionless wall distance $y^+ < 5$. For the dynamic meshing, the domain was re-meshed at each time step to update the moving manikin.

The number of steps per second (called cadence) and the walking speed of a person are subject to various human factors. We assumed a cadence of 2 steps per second with a mean walking speed of 1.2 m/s based on gait parameters presented in Al-Obaidi et al. (2003). To reduce the computational demand of dynamic meshing, walking gestures were simplified as swinging pendulums with the base taken at the shoulder and hips, and therefore no bending of knees and elbows. The total flexion angle for the arms and legs were 60° and

40° based on Han et al. (2013) and the rotating limb angular velocities were calculated from the length of limbs, the swinging period, and walking speed. The gait cycle was achieved by defining the angular limb velocities through a User-Defined-Function (UDF) in the commercial CFD software ANSYS Fluent v16 (Figure 5.2). Under the walking speed of 1.2m/s, the manikin had walked for a distance of 3.6 meters under a velocity of 1.2m/s thus travelled for 3 seconds and then stopped for 3 seconds.

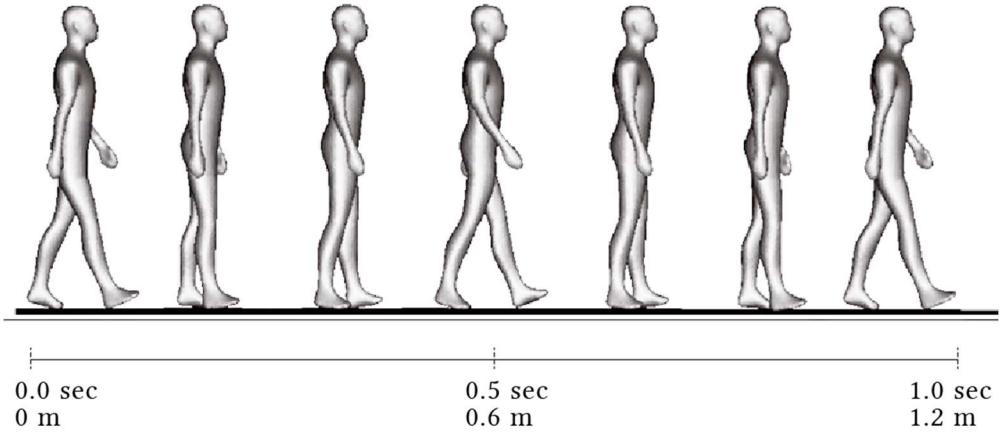

Figure 5.2 Gait cycle in the simulation within a normal gait cycle (1 second). The walking speed is 1.2m/s

In numerical studies, the body temperature is usually set in the range of 30.3°C to 33.7°C (Murakami et al., 1999, Salmanzadeh et al., 2012, Li et al., 2013). In this chapter, the manikin used a fixed surface temperature of 32°C, with an air temperature of 22°C. Since our objective was to compare the thermal plume around the manikin during walking, the convective heat transfer from the body surface was the main contributor, and radiation, evaporation, and respiration were not considered. Likewise, clothing was not considered. A grid independence study was conducted by consecutively reducing individual cell spacing by a factor of 1.3. We started with a grid of 0.9 million and subsequent grids of 1.7 million, 3.6 million, and 6.9 million were created. Velocity profiles along a horizontal and vertical line behind the manikin showed convergence between mesh size 3.6 million and 6.9 million. For computational efficiency and accuracy, the 3.6-million model was chosen for the remainder of this case.

5.2.3 Air Flow and Heat Transfer Models

The manikin motion in the computational domain was achieved by the layering and re-meshing dynamic mesh methods. For a general scalar ϕ on an arbitrary control volume V with a moving boundary, the integral form of the conservation equation is given as:

$$\frac{\partial}{\partial t}\int_V \rho\phi dV + \int_{\partial V} \rho\phi(\vec{u} - \vec{u}_g)\cdot d\boldsymbol{A} = \int_{\partial V} \Gamma\nabla\phi \cdot d\boldsymbol{A} + \int_V S_\phi dV \tag{5.1}$$

where, ϕ represents a scalar, ρ is the fluid density, $\vec{u}$ is the flow velocity vector; $\vec{u}_g$ is the grid velocity of the moving mesh, $\boldsymbol{A}$ is the boundary of the control volume V, Γ is the diffusion coefficient, S_ϕ is the source term. Under thermal conditions, the buoyant force is resulted from the density gradients in the vertical direction and is considered using the Boussinesq approximation, which retains the density variation in the buoyancy term in the vertical component while the density is a constant in the inertial terms and the continuity equation.

Previous studies showed that for a thermal body in still air, a convective laminar boundary layer formed at the feet. As the flow proceeded up the legs by the buoyancy forces, the flow transitioned to a turbulent flow in the upper body (Craven and Settles, 2006). We evaluated two turbulence models based on Tominaga (2015)'s study on steady and unsteady RANS turbulence models which showed the unsteady RNG k-ε model was able predict the velocity and total kinetic energy fields better than the k-ω SST model for flow separation over a building. However, the unsteady RNG model overestimated the reattachment lengths of flow over the roof, and behind the buildings. Furthermore, the k-ω SST was the only URANS model (from the five tested) that successfully reproduced unsteady fluctuation behind the building. While this has significant bearing for unsteady flows over stagnant bodies, the reversed reference frame of a moving body in a stagnant flow field will naturally induce flow field fluctuations. Our model validation compared the results from the RNG k-ε model with the Shear Stress Transport (SST) turbulence model. The discretization schemes used were the QUICK scheme for momentum, second-order upwind for the convection and diffusion terms, and the SIMPLE algorithm for pressure-velocity coupling. The time step was 0.002s and the mesh was updated at each time step matching the manikin movement.

5.3 Results

5.3.1 Air Flow Patterns Across a Vertical Cylinder

The averaged velocity field on the centre plane of the vertical cylinder (shown in Figure 4.4) was compared with measured data by Rostamy et al. (2012). The immediate downstream flow that originated around the free end (top cylinder surface, free from other surfaces), and persisting in the stream-wise direction was observed in the simulated results. There are two downstream vortices within the wake; one was the tip vortex at the free end which both turbulence models capture, and the other was the base vortex near the cylinder-floor junction which only the RNG k-ε model captured. The saddle point separating the two vortices was slightly captured by the RNG k-ε model and not at all by the $k\omega$-SST model. Both turbulence models showed minor differences in the prediction in the v and w velocity components.

Figure 5.3 shows the comparisons of the normalized streamwise and vertical velocities on 3 vertical lines behind the cylinder at y/D = 1, y/D = 2 and y/D = 3 between PIV measurement data by Rostamy et al., CFD simulations using

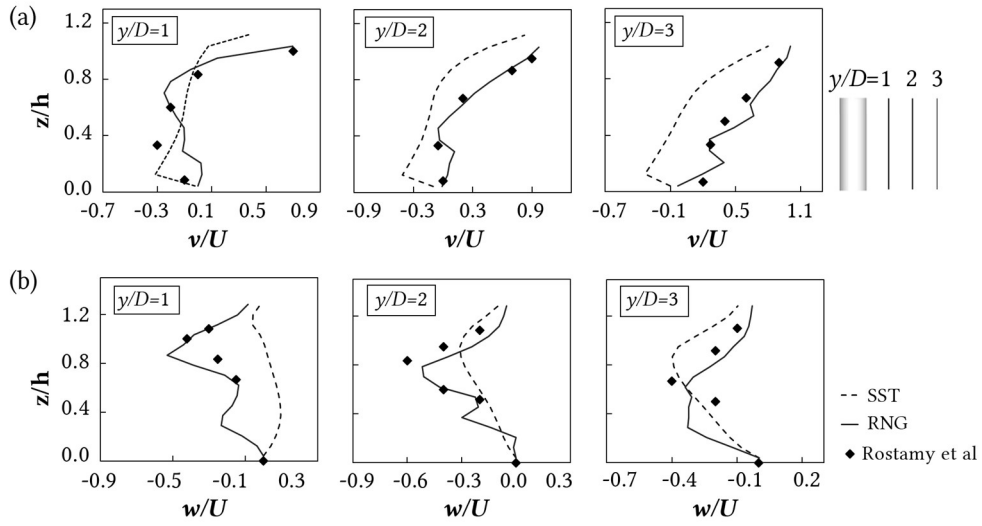

Figure 5.3 Comparisons of (a) normalized v-velocity component (v/U), (b) normalized w-velocity component (w/U) on 3 vertical lines behind the cylinder at y/D = 1, y/D = 2 and y/D = 3 between PIV measurement data by Rostamy et al., CFD simulations using RNG turbulence model and CFD simulations using kω-SST turbulence model.

RNG k-ε turbulence model and CFD simulations using $k\omega$-SST turbulence model. The RNG k-ε model had shown a good agreement with the measured data from the near-body to the downstream region, despite a small deviation of the streamwise velocity v/U close to cylinder-floor junction close to where vortices from different directions converged.

Overall the RNG k-ε model showed better performance over the $k\omega$-SST in predicting the velocity distribution in the lower half of the near wake region.

5.3.2 Flow Pattern Comparison Between Vertical Cylinder and Manikin

For simplicity, vertical cylinders and idealized geometries have been used as a surrogate for realistic human body geometries, leading to different flow dynamics. We compared the discrepancies in flow behaviour between the cylinder and manikin by using a free stream velocity of U = 3.6 m/s for the manikin to achieve a consistent Reynolds number with the cylinder. The streamline and velocity distributions for the manikin are shown in Figure 5.4. Qualitatively we find multiple recirculation regions in the near wake of the manikin

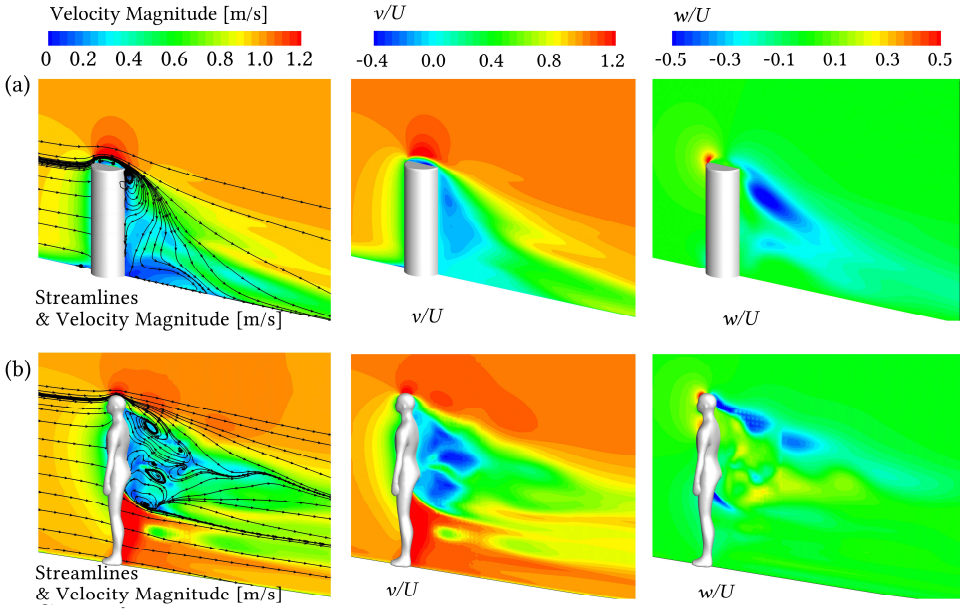

Figure 5.4 CFD simulation results of streamlines, normalized v-velocity component (v/U), normalized w-velocity component (w/U) of a (a) cylinder and (b) stationary manikin on the centre plane

which are not observed in the cylinder. This is caused by the presence of the air gaps between the arm and body, and legs. For the cylinder, flow separation occurred at the leading edge of the top surface, resulting in a small recirculation region and reattachment towards the trailing edge. The flow separated again below the trailing edge and a large recirculation region formed behind the cylinder. At similar positions to the cylinder, the manikin head with its streamlined shape, produced no separation at the front of the head, and only separated at the back of the head forming a main recirculation region similar to the cylinder.

More complex recirculation regions were produced behind the manikin due to the asymmetrical manikin shape. An anti-clockwise recirculation developed at the upper leg gap, which counteracted with the downwash of air, forming a pair of counter-rotating vortices behind the torso. The streamwise and vertical velocity fields (normalized by the freestream velocity magnitude *U*) showed some similar patterns in the upper third of the manikin and cylinder. For the remaining region below, there were significant flow differences due to the additional air gaps from the presence of the arms and legs.

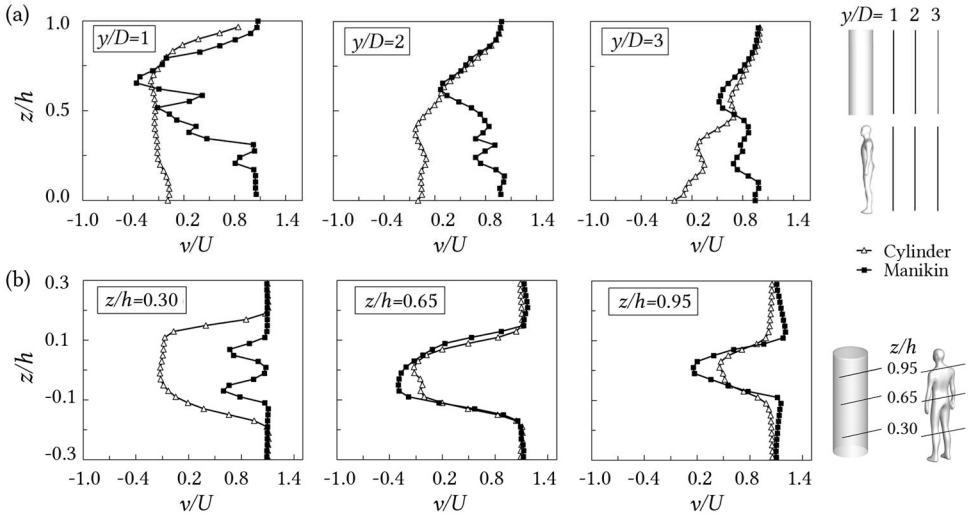

Figure 5.5 Comparisons of normalized streamwise velocity components (v/U) (a) on 3 vertical lines behind the stationary cylinder and manikin at y/D = 1, y/D = 2 and y/D = 3 and (b) on 3 horizontal lines at heights of z/h = 0.3, z/h = 0.65 and z/h = 0.95 behind the stationary cylinder and the manikin at y/D = 1.

Normalized streamwise velocity v/U profiles shown in Figure 5.5a were taken along three vertical lines progressively downstream at y/D = 1, 2, 3 from the manikin in the wake region along the centre plane (x = 0). The velocity profiles between the two bodies are similar in the upper body because of the similar bulk shapes. The profiles consistently deviated from each other below z/h = 0.5 (halfway mark of the geometries) where the manikin shape showed an increase in the streamwise velocity. This led to a deviation in streamwise velocity of up to 90% caused by the gap between the legs in the manikin allowing oncoming wind to pass through. Downstream from the body the flow begins to recover and the differences caused by different geometry shapes diminishes.

Profiles were also taken along three horizontal lines from the floor upwards at distances of z/h = 0.3 (knee), 0.65 (waist), 0.9 (head) behind the manikin at a distance of y/D = 1 downstream of the manikin (Figure 5.5b). Discrepancies in the velocity profiles were largest reaching 42% at knee height, z/h = 0.3 (velocity behind the cylinder decreased to -0.1 m/s and the manikin decreased to 0.7 m/s). The wake width at this position for the manikin was thinner and its velocities greater than for the cylinder. At waist height at z/h = 0.65, the velocity profiles were almost the same due to the similar solid shaped bodies, while at head height at z/h = 0.95, the velocity profiles deviated slightly due to the presence of the head in the manikin model.

5.3.3 Differences Between Rigid Motion and Swinging Motion

Figure 5.6 shows velocity contours and vectors on the mid-plane (x = 0m) and at the plane through the right leg (x = 0.11 m) under a rigid and swinging motion at different time steps. The velocity contours are not shown for velocities below 0.10m/s. The induced velocities were created from the relative motion between stationary and fixed stagnant fluids. In the upper body this is evident from the high velocities along the body and a trailing wake forms. Vectors show the fluid moves upwards and around in a semi-circle from the head returning into the wake as it becomes entrained into the flow. Velocity vectors in the wake move back into the wake towards the manikin. In the front of the body the vectors are directed forwards suggesting that the fluid is pushed away as the body moves through the flow field.

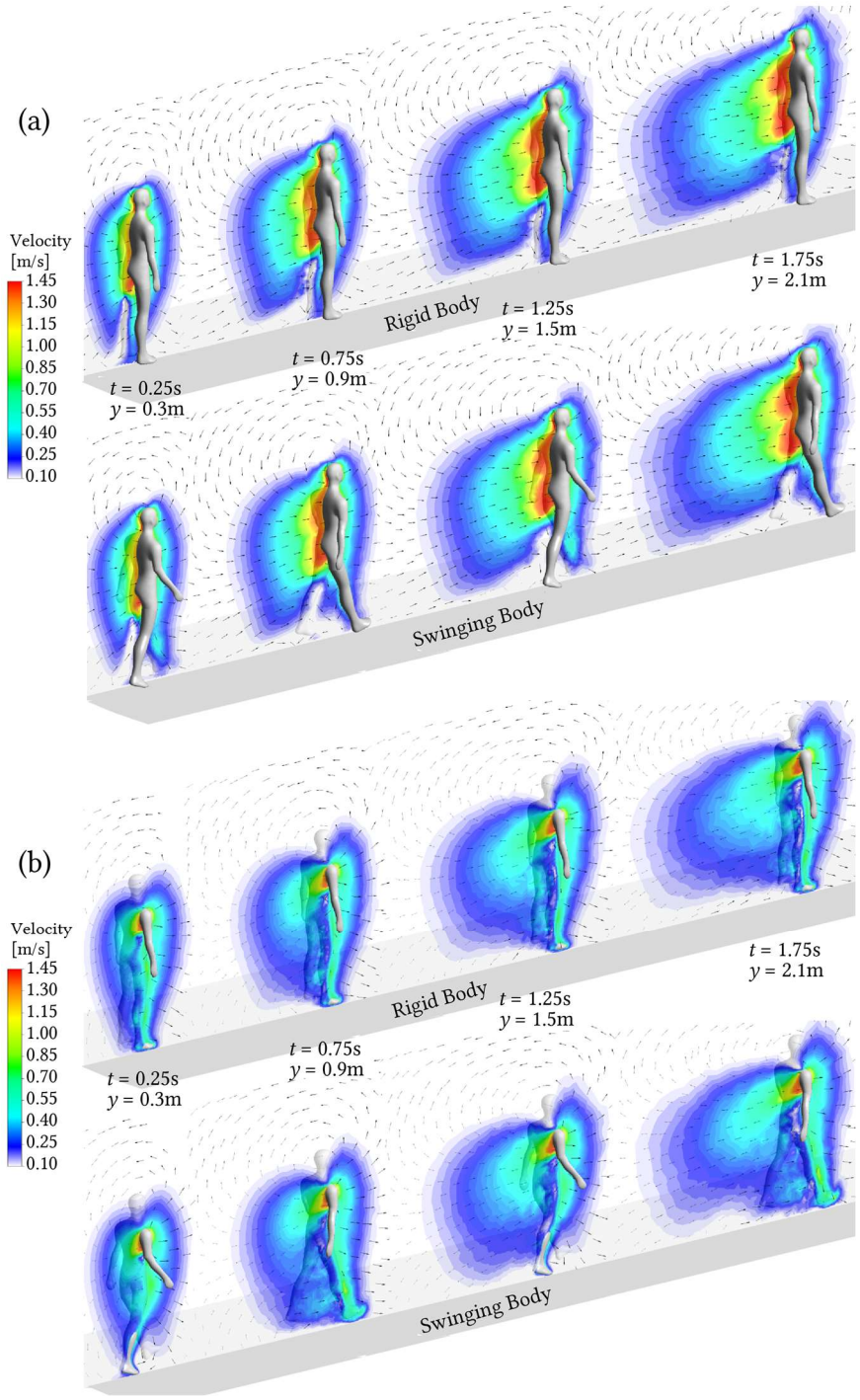

Figure 5.6 Velocity contour and vectors on the (a) centred plane, x = 0m and (b) on the right leg at plane x = 0.06 m under rigid motion and swinging motion

The mid plane contours show little difference in the flow field in the upper body caused by the different walking motion shearing forces induce velocities. In the lower body where the legs swing, the contours form around the swinging leg which is not found for the rigid body. The velocity contours on the right leg at plane x = 0.11m shows high velocity at the gap between the arm and body. This suggests that high velocities are formed at separation regions around the body through the relative motion of the moving body. The shape of the velocity wake shows slight differences.

The major differences between the wake flow generated by the two types of motion occurred at the legs. The velocity at the legs is constant for the rigid body but there is a high to low velocity cycle for the swinging body as the legs move. When the right leg was at the stance phase (as a pivot leg) while the other leg was swinging forward (at t = 0.25s and t = 1.25s in Figure 5.6b), the airflow around the stance leg has the lowest velocities during the gait cycle. When the right leg turned to become the swinging leg (t = 0.75s and t = 1.75s in Figure 5.6b), the velocities of the airflow around the swinging leg got increased and were stronger than the velocities under the rigid motion. Therefore, the airflow generated by the rigid motion would have relatively symmetric flow patterns around both legs while the swinging motion would generate alternating flow patterns with different strength and direction at the legs within a gait cycle. The interaction and counteraction between the airflow generated by both legs would result in distinct flow patterns for the two types of motion thus would further influence the transport mechanisms if contaminates were introduced in the lower region.

To quantify the differences between the rigid and swinging motions we track the flow velocity during walking at three pairs of locations, each at 20 mm from the limb surfaces on: *i)* the inner and outer arm *ii)* the inner and outer thigh and *iii)* the inner and outer ankle. The instantaneous velocity comparisons are shown in Figure 5.7 where in both models the manikin moved for three seconds at a constant velocity of 1.2m/s. After three seconds the manikin came to a stop and the simulation continued for a further three seconds. The rigid body motion shows rapid fluctuating velocities with a consistent amplitude and frequency induced by the flow separation. The phenomenon is similar to vortex shedding characteristics produced by bluff bodies that produce periodical irregularities on the flow field. If we consider the arm, the thigh and

the ankle as cylinders with diameters of 0.1m, 0.2m and 0.08m, their corresponding Reynolds numbers of 9,000, 16,000, 6,400 were in the sub-critical Reynolds numbers range, where shedding tends to be organized with an almost constant non-dimensional vortex shedding frequency of St = 0.19 ~ 0.21 (where St is the Strouhal number) according to external flow over a cylinder (Blevins, 1990).

In the swinging motion, there are high frequency oscillations that are embedded within larger velocity oscillations that coincide with the pendulum gait cycle motion. The instantaneous velocities between the different locations varied significantly. At the inner arm and inner thigh where it is close to the

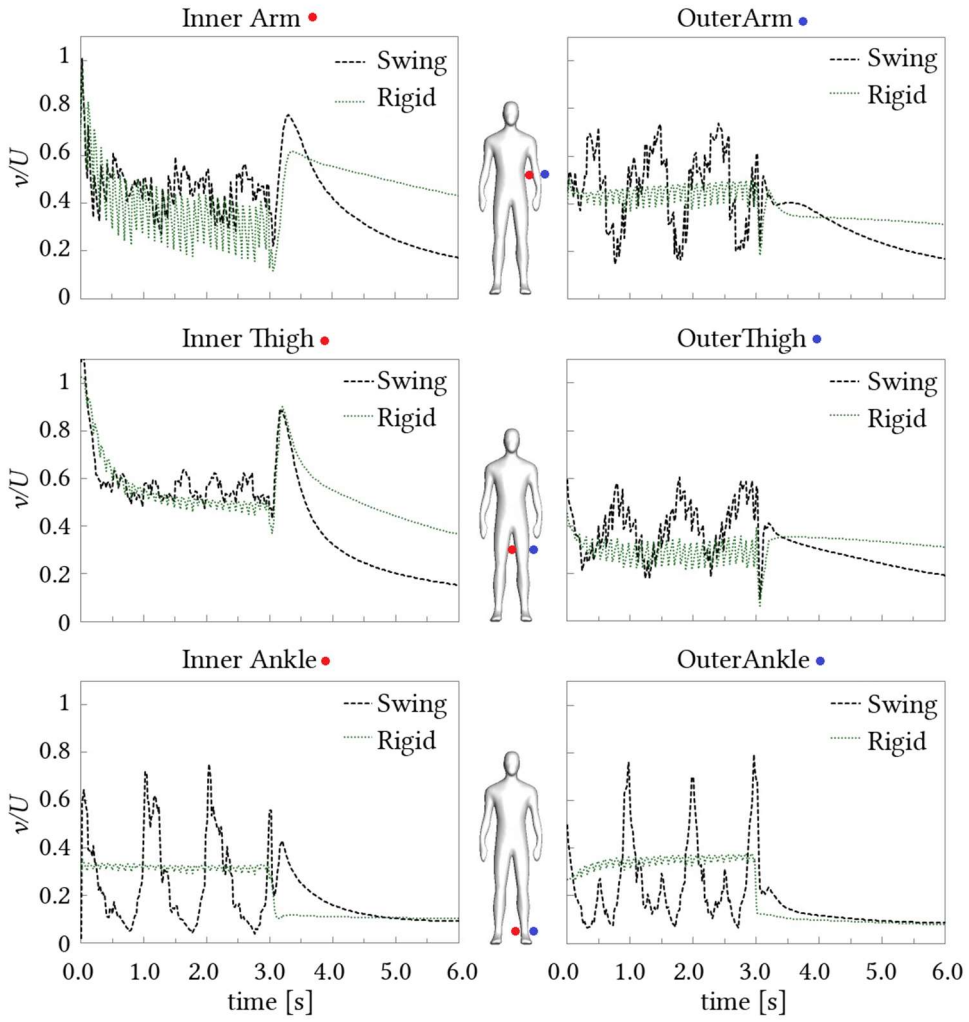

Figure 5.7 The comparisons of velocities detected around the rigid body and the swinging body with 20mm to the inner side and the outer side of the arm, thigh and ankle surfaces

pivot point of the swinging motion, the large-scale velocity fluctuation is relatively flat. In these regions we can observe the small scale rapid velocity fluctuations. However further away from the pivot point, such as in the outer arm, and in the ankle regions, the gait cycle motion dominates the flow velocity damping out a lot of the small-scale fluctuations. Taking a gait cycle (a period of 1 second) for example, the left leg was swinging during t = 0.75s to t = 1.25s and turned to stance phase during t = 1.25s to 1.75s, then the gait cycle repeated. The velocities observed at the inner and outer ankle showed the velocities increased to maximum during the swinging phase (t = 0.75s to t = 1.25s), and then dropped to the lowest as the left leg became the stance leg (t = 1.25s to 1.75s).

Comparing to the rigid motion, the swinging motion gets increased velocities with the swinging leg as it moved forwards by pushing the air out and drawing it air around the ankle entraining it into the wake. As the leg comes to rest to act as the pivot foot for the next step, the velocity approaches zero. Same patterns of velocity variations can be observed around the arms and thighs as the airflow is influenced by swinging limbs. The most obvious velocity discrepancies between the walking models occurred in the lower half of the body, where the rigid motion generated weak airflow while the swinging motion produced much stronger periodical air movements due to the vigorous movement of the feet. The maximum velocity around the swinging ankle could be 2.5 times larger and the minimum velocity could be 4 times smaller comparing to the velocities at the same position under rigid motion.

When the manikin came to a stop at t = 3s, the residual momentum from the wake passes propagated through the narrow gaps at the inner arm and inner thigh, hence generating an immediate velocity jump. The swinging motion had experienced a larger increase in velocities at those areas due to the inertia yielded by the pendulum limb motion. While at the points at the outer arm and outer thigh, the wake dropped off much quicker in the swinging motion than in the rigid motion.

5.3.4 Thermal Effects on the Motion-Induced Wake Flow

The effect of walking on the thermal plume was investigated under the swinging walking motion. To begin the modelling, the thermal environment around

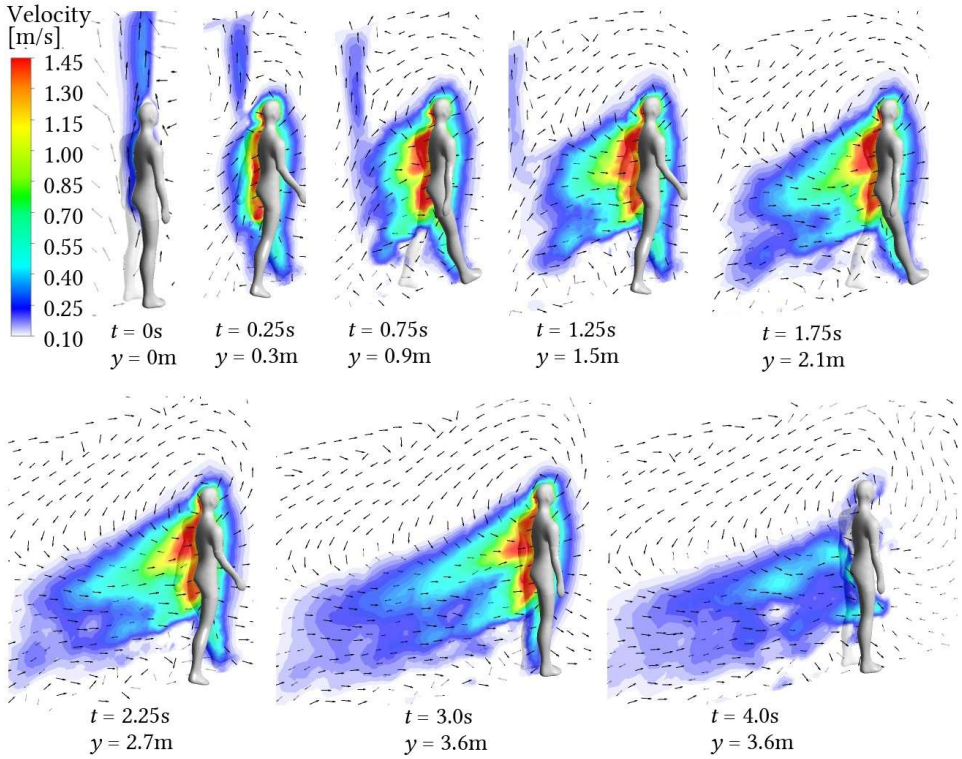

Figure 5.8 The velocity field on the mid-plane (x = 0m) under the (a) isothermal and (b)thermal conditions at t = 0s to t = 4.0s

the body under steady state was established. A thermal plume was formed where it was weak at the bottom of the body and became stronger in the upper body. The plume rises vertically above the manikin head with a maximum velocity of 0.25 m/s at 0.18m above the head. This is consistent with the experimental findings of 0.24 m/s (Craven and Settles, 2006) to 0.255 m/s (Zukowska et al., 2007) as the maximum thermal plume velocity. The swinging motion was then introduced into the thermal domain where the thermal plume does not move with the manikin. Instead it trails behind slowly remaining connected to the manikin wake flow (based on flow velocities > 0.1m/s) until t = 1.25s in Figure 5.8. The velocity vectors in the thermal plume are directed upwards and nearby flow are entrained in the plume. An anti-clockwise recirculation was formed from the rising thermal plume which countered the clockwise recirculation coming from the downwash flow from the manikin. This led to a greater downwash flow, and the wake is narrowed compared to the isothermal case where the wake is more circular.

The transient velocity variation at points in front of the head, shoulder, thigh, and ankle for thermal and isothermal manikin cases were tracked and shown in Figure 5.9. During walking (t = 0s to t = 3s), the thermal manikin showed a smaller stream-wise velocity (v/U in the y direction) but a larger vertical velocity (w/D in the z direction) compared to the isothermal case. This suggests the airflow is influenced by thermal effects with the increased vertical velocity driven by the buoyancy flow that starts from the feet and increases with the

Figure 5.9 The velocity variation against time at different detection points near the body under the thermal and iso-thermal conditions

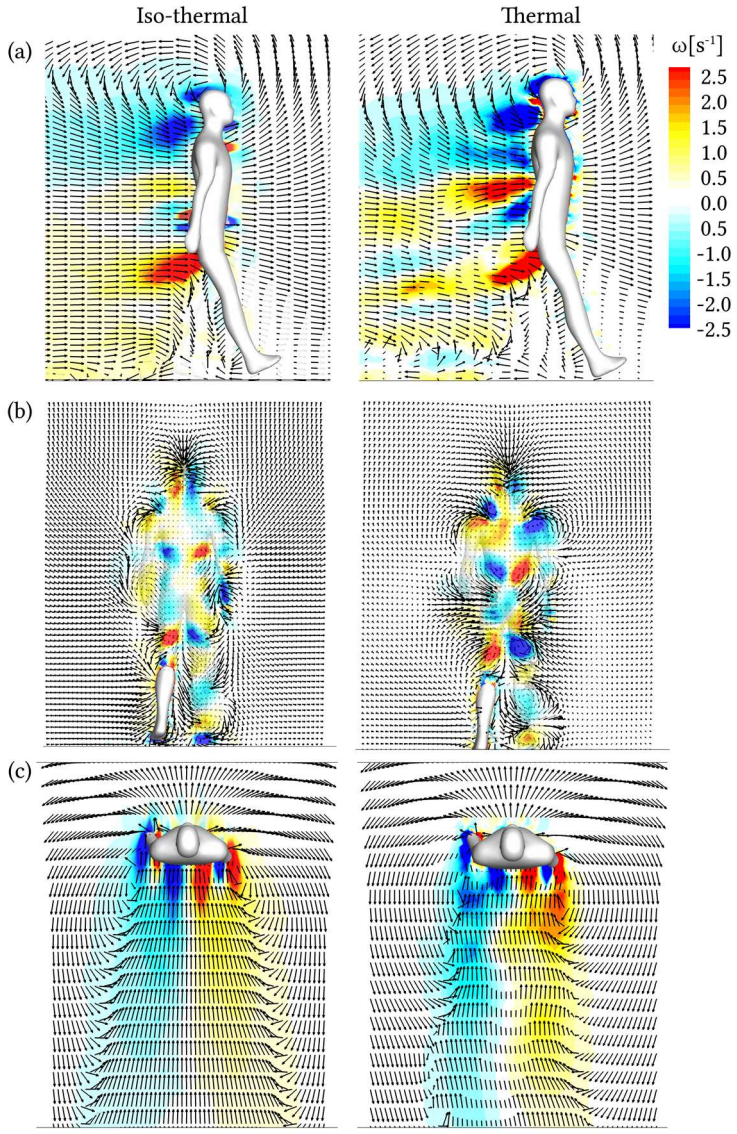

Figure 5.10 the contour of vorticity magnitude (a) ω_x on the mid-plane across the body (x = 0 m), (b) ω_y on the vertical plane 0.2 m behind the manikin (y = 3.1 m) and (c) ω_z on the horizontal plane through the waist (z = 1.1 m) at t = 2.75s.

manikin height. The airflow in the lower body is dominated by the alternating acceleration and deceleration of the swinging limbs and pivot phases. In this region we found that the vertical velocity component for both models is similar. When the manikin stopped walking, the velocity in the thermal condition increased in the streamwise and vertical (w/U) direction up to 2-4 times the average velocity during the walking. While in the lower body, thermal effects around the legs was not evident, as the buoyant effects has not grown sufficiently. Furthermore, when the streamwise velocity of swinging motion is less

than the rigid motion, we find this is compensated by an increase in vertical velocity, and vice-versa.

Contours of vorticity magnitude ω_x, ω_y, ω_z at time t = 2.75s are shown in Figure 5.10a on a midplane across the body at x = 0 m, Figure 5.10b a vertical plane 0.2 m behind the manikin at y = 3.1 m and Figure 5.10c a horizontal plane through the waist at z = 1.1 m. The vorticity measured the local rotation of the airflow when moved by an infinitesimal distance in a direction perpendicular to it. For the thermal case, a strong negative vorticity concentration convected from the head and shoulders shown on the mid plane, indicating an anti-clock-wise rotation at the back of the upper body where the significant downwash occurred. Additionally, a strong positive vorticity protruded from the leg gap shown by a clock-wise rotation against the downwash of air behind the upper body. Recirculation regions were formed behind the solid torso and several pairs of counter-rotating vortices were observed behind the head, torso and legs, on the vertical plane. Compared to the isothermal body, the thermal plume generated stronger rotating flows in the same area, especially behind the forearm and thigh where the swinging arms and legs interacted with each other. The asymmetric vortex shedding in the horizontal plane interacted with the downwash, thus inducing lateral and vertical spreading from the upper body towards the downstream region. The counter-rotating vortex shedding then stretched downwards and further into the wake. Downstream of the thermal body, the vortices showed a narrowed and subdued span-wise vortex shedding.

Vortex structures of the manikin within a full gait cycle (1.75s to 2.75s) are shown in Figure 5.11 as iso-surfaces of λ_2 coloured with velocity magnitude. Unlike the stationary bluff bodies where a long wake region is stretched downstream from an oncoming flow, the swinging walking motion generated small vortices that trailed the body. The vortex cores generate mainly behind the torso and on the legs during upright position. At the swinging limbs, larger vortices formed when the limbs finished the swinging phase. When manikin stopped moving (t = 3s), the vortex cores propagated through the gaps between arms and thighs. This explains the notable velocity rise for the velocity profiles in Figure 5.10 detection points at the inner side of the thigh and the arm after the manikin stopped moving.

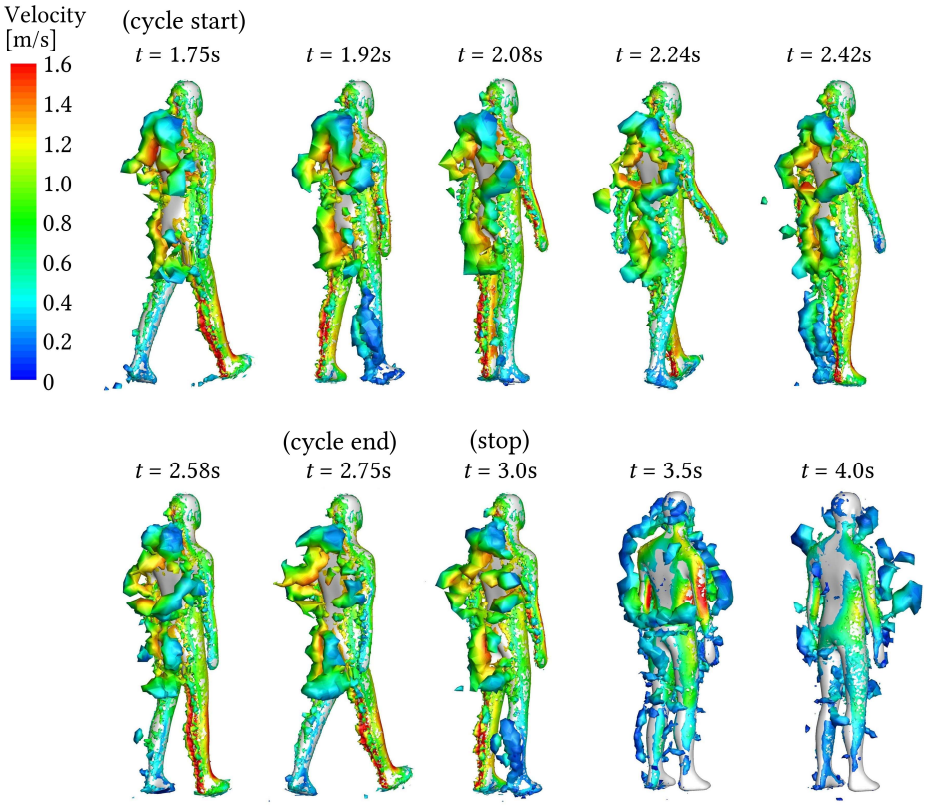

Figure 5.11 The vortex structures of the manikin within a full gait cycle (1.75s to 2.75s) and after its stop (3.0 s to 4.0 s)

5.4 Conclusion

This chapter presented unsteady simulations of the wake flow induced by a moving manikin with a focus on comparing the discrepancies generated in the flow field by simplified geometry, swinging limbs and thermal conditions. The key points are summarised as follows:

- By comparing a cylinder and a manikin with a similar aspect ratio, the main discrepancies were found behind the head and legs, where the body shape differed most. The wake showed similar patterns behind the upper part of the cylinder and the solid torso of the manikin, while at the lower region, there were distinct differences due to the air gaps from the arms and legs. The results showed the need for using a realistic geometry of human for analysing the airflow features of the human-induced wake.

- Using the swinging body motion produced a velocity fluctuation corresponding to the gait cycle, with peak values 2-4 times larger than the airflow velocity induced by the rigid motion in the same areas. The main discrepancy occurred in the lower half of the body influenced by the swinging legs.
- Heat transfer effects are negligible on the fluid flow during the walking motion of 1.2m/s. However, after the manikin has stopped moving it becomes important when considering the wake flow dynamics, especially in the upper body where thermal plume manifests.

Chapter 6
Particle Suspension Induced by Realistic Manikin Motion

The main findings of this chapter have been published in:

- **Tao, Y.,** Inthavong, K. & Tu, J. Y. (2017). Dynamic Meshing Modelling for Particle Suspension Caused by Swinging Manikin Motion. *Building and Environment*, 123, 529-542.
  DOI: 10.1016/j.buildenv.2017.07.026, ***IF = 4.539***

- **Tao, Y.,** Inthavong, K., Petersen, P., Mohanarangam, K., Yang, W., Tu, J. Y. (2016). Experimental and CFD modelling of indoor air and particle re-dispersing from a moving manikin. *20th Australasian Fluid Mechanics Conference (AFMC)*, 5-8 Dec, Perth, Australia.

Human-induced wake flow characteristics and its impact on particle re-dispersion from floor boards was investigated by performing CFD simulations with dynamic-meshing of a moving thermal manikin model. The manikin motion with swinging limbs was achieved by the re-meshing method to update the grid with each time step. The characteristics of the wake flow field generated by three walking speeds (0.8m/s, 1.2m/s and 1.8m/s) were compared. Particle transport from the floors and its re-dispersion was tracked by the Lagrangian approach. The results focused on the significant airflow patterns in the indoor flow field and how it would influence the particle suspension. The residual flow disturbances after the manikin stopped walking and its interaction with the thermal plume continued to influence the particle to spread and deposit over time. The particle concentration entering the frontal zones of the body during the walking was evaluated to show the level of occupants' exposure to contaminants.

6.1 Introduction

Human activity has a significant influence on indoor airflow patterns by producing distinct wake flow regions and unsteady vortex shedding over the body(Heist et al., 2003, Johnson et al., 1996, Ge et al., 2013, Li et al., 2014). Its impact on indoor contaminant transport and dispersion has received a lot of attention (Ferro et al., 2004, Mazumdar et al., 2011, Miguel et al., 2005, Tian et al., 2016, Wang and Chow, 2011) especially in indoor environments such as aircraft cabins, hospital wards, surgical rooms, and clean rooms, where occupants' exposure to airborne contaminants are of concern (Oberoi et al., 2010, Inthavong et al., 2009, Se et al., 2010, Gao and Niu, 2005, Mazumdar et al., 2010). The occupant induced wake exhibits fluid dynamics found in separated flows over bluff bodies, where a mixing zone of vortices entrain air into a reverse flow region (Flynn and Ljungqvist, 1995, Mahjoub Said et al., 2008, Zhang et al., 2016).

Simplified geometries such as vertical finite cylinders and cuboids have been used as substitutes for human bodies (Poussou et al., 2010, Thatcher et al., 2004). However, this leads to discrepancies in flow features due to the simplified geometry (Edge et al., 2005, Tao et al., 2017a). For example, when legs are considered as two cylinders instead of one single thick cylinder, there is increased mixing in the wake produced by the gap between the legs accelerating flow (Edge et al., 2005). An issue arising with flow over a stationary manikin is the flow separation at the feet which neglects disturbances caused by the manikin motion; thus, the near wake flow characteristics during walking are only partially represented. Another factor to consider is the effects of heat transfer leading to thermal plumes from the human body. Murakami et al. (1999) investigated the thermal and dynamic effects of wind on stationary bodies and revealed a thin layer of warm rising air around the body under a stagnant or weak wind environment; but this disappeared when the wind velocity increased.

Similarly, the effects of the induced wake from moving bodies wields significant influence on particle dispersion and re-suspension in indoor air quality studies (Inthavong et al., 2013a, Li et al., 2014, Gao and Niu, 2005, Zhou et al., 2011). Early experimental studies investigated the effects of airflow patterns around manikins on contaminant concentrations (Heist et al., 2003, Johnson

et al., 1996). Numerical studies visualised the influence of unsteady vortex shedding from flow over static bodies on contaminant transport (Murakami et al., 1999, Edge et al., 2005, Ge et al., 2013). Recently a growing number of computational studies using Computational Fluid Dynamics (CFD) have laid emphases on the effects of human activity on the wake dynamics (Choi and Edwards, 2008, Choi and Edwards, 2012, Brohus et al., 2006, Hang et al., 2014, Wu and Gao, 2014) which use dynamic meshing techniques. This advances modelling capability and can capture transient effects of a moving manikin.

Poussou et al. (2010), Brohus et al. (2006) used dynamic meshing to qualitatively capture the wake flow from moving blocks. However, realistic anthropomorphic manikins provide a better representation of the flow behaviour where results in the near body regions can be discerned (Han et al., 2013, Tao et al., 2016, Gao and Niu, 2005, Mazumdar et al., 2010). While these studies have advanced the modelling capability and complexity by integrating dispersed particle modelling for inhalation exposure assessments, the study of particle suspension from floors influenced by a moving manikin with swinging motion, and heat transfer is yet to be investigated. The advancements in modelling can lead to enhanced evaluation of airborne contaminant exposure influenced by occupant activity which is also prevalent in indoor and urban environments (e.g. pollutants, and exhaust fumes in pedestrian/urban streets).

In this chapter, an anthropomorphic manikin was modelled with realistic walking and swinging motion, and thermal effects. The numerical setup was first validated with benchmark test comparisons with experimental data of a simplified cylindrical body, before being applied to the moving manikin model. The results focused on the spatial and temporal characteristics of the wake flow induced by three walking speeds (0.8m/s, 1.2m/s and 1.8m/s) and their effects on particle dispersion and occupant exposure to contaminants.

6.2 Method

6.2.1 Computational Models

To validate the numerical model setup, a transient simulation of near wake flow around a vertical cylinder was first performed. The transient solution was time-averaged and its velocity field was compared with PIV measurements by (Rostamy et al., 2012). A circular cylinder with diameter of 31.5mm and an aspect ratio (height/diameter, *h/D*) of 3.0 was used - which is similar to the manikin (*h/D* = 2.93). The computational domain around the cylinder was 1.96m × 0.91m × 1.13m. The free stream velocity was *U* = 20m/s giving a Reynolds number of 42000 based on the cylinder diameter. To resolve the turbulent boundary layer, ten prism cell layers were created on the cylinder surface with a first grid spacing of 1×10^{-4}m. This produced a dimensionless wall distance *y+* of less than 5 which is within the viscous sub-layer and ensured sufficient grid points were within the buffer region where turbulent production rapidly

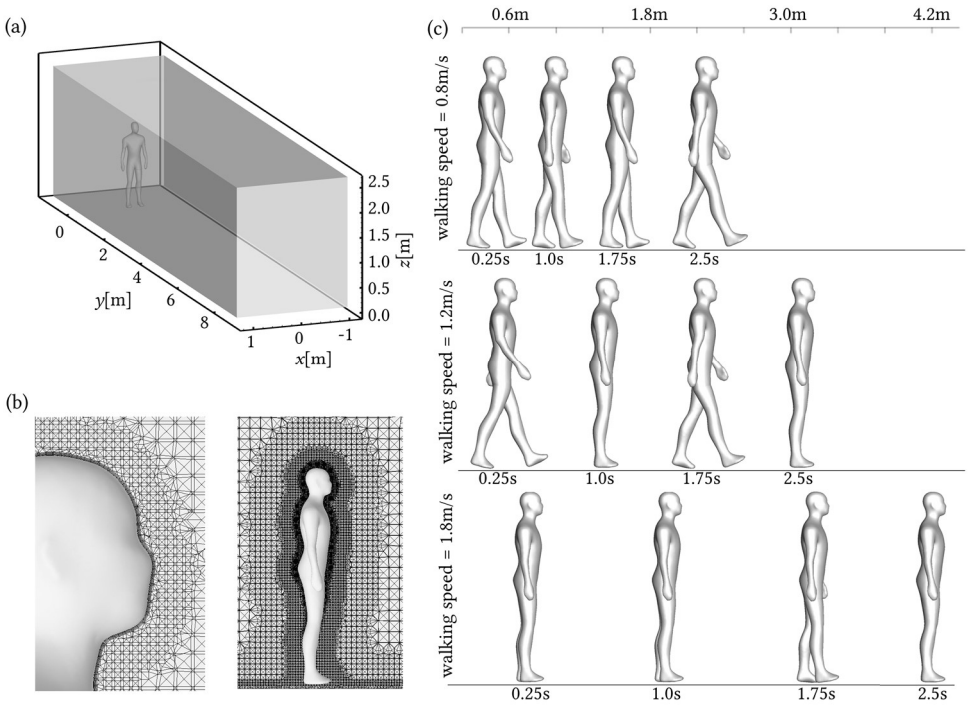

Figure 6.1 (a) Computational domain of the room, x - y - z- coordinates are in meters; (b) Prism layers and tetrahedral mesh generation around the manikin body; (c) gait phases at the same time steps under 3 walking speeds (speed of 1.8m/s stopped walking at 2.33s)

increases. A structured hexahedral mesh with 3.1 million cells was generated and a time step of $t = 1\times 10^{-3}$s was used.

The manikin model had dimensions of 1.7m-height, 0.58m-width and the computational domain was 2.6 m (x-coordinate) ×10.0m (y-coordinate) × 2.7 m (z-coordinate). The coordinate system located the manikin at an initial standing position at x = 0m, y = 0m, facing the $+y$ direction 1m from the back wall (Figure 6.1a). Unstructured tetrahedral cells and prism layers were generated for the domain Figure 6.1b). The near-wall mesh surfaces were also created with ten prism layers with $y+ < 5$. For the dynamic meshing the domain was re-meshed at each time step updating the moving manikin position and stance. The distances travelled at the same time steps under three walking speeds are compared in Figure 6.1a. In each of the models, the manikin walked to 4.2m and the simulations continued until the flow field dissipated.

To reduce the computational demand of the dynamic meshing, walking postures were simplified and the arms and legs were treated as rigid swinging pendulums with its pivot taken at the shoulder and hips respectively. The total flexion angle for the arms and legs were 60˚ and 40˚ based on (Han et al., 2013) and the rotating limb angular velocities were formulated from the length of limbs, walking speed, and it's swinging period. The number of steps per second (called cadence) and the walking speed of a person are subject to human factors. According to gait parameters presented in (Al-Obaidi et al., 2003) , a normal walking speed of 1.2m/s with a cadence of 2 steps per second was chosen as a baseline walking speed. To cover the range of a typical gait cycles related to different walking speeds, we used a cadence of 1.33 steps/second for 0.8m/s walking speed and 3.0 steps/second for 1.8m/s walking speed. Stride lengths of each gait were kept constant under the different walking speeds. The gait cycle defining the angular limb velocities, and dynamic mesh motion was inputted through a User-Defined-Function (UDF) in the commercial CFD software ANSYS Fluent v14.5.

In numerical studies, the body temperature is usually set in the range of 30.3˚C to 33.7˚C (Murakami et al., 1999, Salmanzadeh et al., 2012, Li et al., 2013) and in this chapter the manikin had a constant surface temperature of 32˚C. The air temperature was set to 22˚C. Since our objective was to compare the thermal plume around the manikin during walking, the convective heat transfer

from the body surface was the main contributor, and radiation, evaporation, and respiration were not considered. Likewise, clothing was not considered. A grid independence study was conducted by consecutively reducing individual cell spacing by a factor of 1.3. We started with a grid of 1.1 million and subsequent grids of 2.0 million, 4.3 million, and 8.3 million were created. Velocity profiles along a horizontal and vertical line behind the manikin showed convergence between mesh size 4.3 million and 8.3 million. For computational efficiency and accuracy, the 4.3-million model was chosen for the remainder of this case.

6.3 Results and Discussion

6.3.1 Airflow Modelling Validation

The time-averaged velocity field on the centre plane of the vertical cylinder simulation (Figure 4.4) was compared with its corresponding measured data by (Rostamy et al., 2012). The immediate downstream flow that originated at the free end (top cylinder surface, free from other surfaces), and persisting in the stream-wise direction was observed in the simulated results. The experimental results show two downstream vortices within the wake; one at the tip vortex at the free end which both turbulence models capture, and the other at the base vortex near the cylinder-floor junction which only the RNG k-ε model captured. The saddle point separating the two vortices was slightly captured by the RNG k-ε model and not at all by the k-ω SST model. Both turbulence models showed minor differences in the prediction in the v and w velocity components. Overall the RNG k-ε model showed better performance over the k-ω SST in predicting the velocity distribution in the lower half of the near wake region.

6.3.2 Flow Characteristics of Human Wake Flow

6.3.2.1 Spatial distribution

The fluid dynamics of the human wake are shown through velocity contour and vector plots (Figure 6.2) on the *x*-plane after the manikin has come to a stop (after walking 4.2m). The total walking duration varied based on the

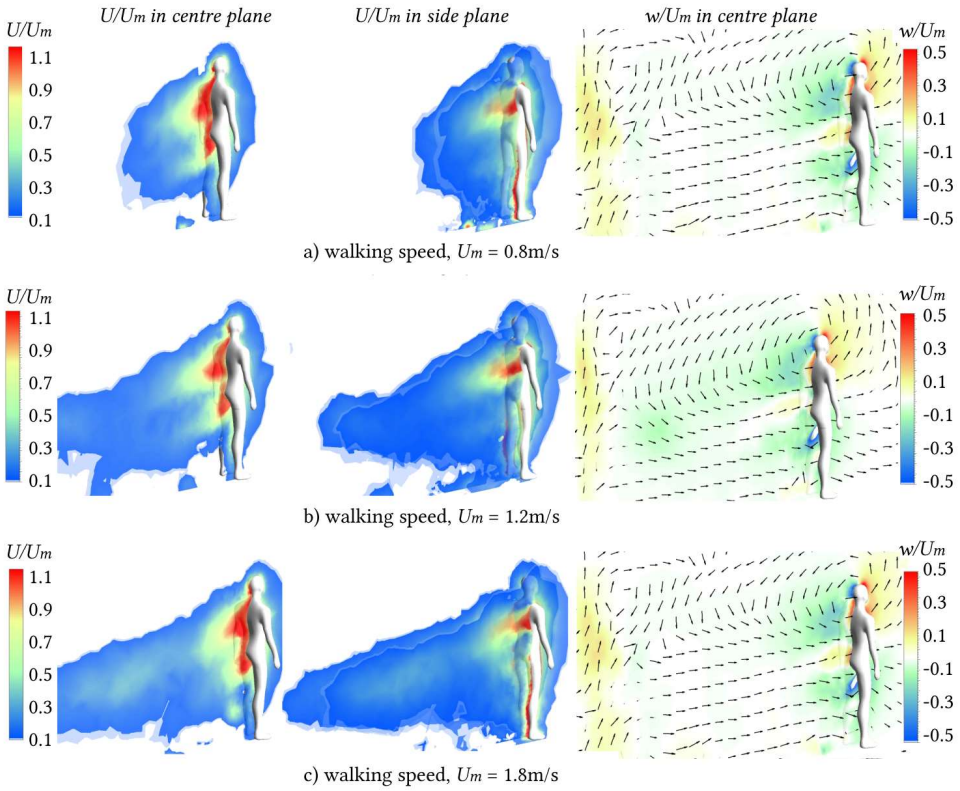

Figure 6.2 Non-dimensionalized velocity field (U/U_m) and non-dimensionalized vertical velocity field (w/U) on the vertical middle plane (x = 0m) under walking speeds of (a) 0.8m/s, (b) 1.2m/s and (c) 1.8m/s

walking speeds of 0.8m/s, 1.2m/s and 1.8m/s. The velocity magnitude (U) and vertical velocity (w) contours were non-dimensionalized by the walking speed (U_m), and these were capped for velocities below U/U_m=0.10 to provide distinct variation between the wake flow and the ambient surrounds. Due to the pressure build up at the manikin frontal body (stagnation points) and the pressure difference at the rear, airflow is driven from the front to the rear. In the centre plane, the disturbed air formed a triangular region of flow behind the solid body with peak velocities of approximately U/U_m=1.2 found proximal to the manikin backline and buttocks. The gap between the legs accelerated the

air through and this counteracted against the wake downwash from the upper body, thus forming a region of weak airflow behind the lower leg region. Two side planes offset from the centre and located at the shoulders on either side of the body shows accelerated flow through the gap between the arm and body. High velocity is found along the calf of the leg that is completing its step and about to produce the flat foot pivot position. Based on the gait cycle and walking speed we can see this occurs on the right calf for walking speeds of U = 0.8 m/s and U = 1.8 m/s, and occurs on the left calf for a walking speed of U = 1.2 m/s. The vertical velocity component and vector plot is shown to highlight the flow motion passing over the head and returning back in a circular motion to the back of the body. In all cases the initially developed thermal plume at the starting position still persists. The region between the initial position and the manikin shows flow moving forwards catching up to the manikin body. No vertical velocity components are found in this region.

While it is expected that the size of the wake region increases with walking speed our analysis is to quantify this. We defined the wake length by extracting the flow field velocity contour with the cut-off velocity of U/U_m=0.10. This was evaluated at different x-planes and the maximum wake length distance was used. The wake lengths were 1.38m, 2.77m and 3.68m for walking speeds of 0.8m/s, 1.2m/s and 1.8m/s, respectively (Table 6.1). The growth of wake length from 0.8m/s to 1.2m/s was larger than the growth from 1.2m/s to 1.8m/s despite the walking speeds increasing by a fixed ratio of 1.5. A second wake length metric we can use is the length where the velocity is capped at half of

Walking Speed	$L_{1.0}$	$L_{0.5}$	$L_{1.0}/L_{0.5}$
0.8 m/s	1.38m	0.71m	1.91
1.2 m/s	2.77m	0.79m	3.51
1.8 m/s	3.68m	0.84m	4.38

Table 6.1 Wake length metrics for the three walking speeds

the walking speed, which we refer to as the wake half length ($L_{0.5}$). In this case we take values from a total of five planes centred around the midplane (one midplane and two planes to its left and right sides) and taking its averaged

value. The wake half lengths under the walking speeds of 0.8m/s, 1.2m/s and 1.8m/s were 0.71m, 0.79m and 0.84m. This produces a more normalised value accounting for the different walking speeds. If we take the ratio of the wake full-length to half-length values we get $L_{1.0}/L_{0.5}$ of 1.94, 3.51, 4.38 from slowest to fastest walking speeds. This shows that the induced wake region for slower walking speeds decays more rapidly.

Streamlines originating from the body at different moments of the gait cycle for a walking speed of 1.2m/s were used to determine the local flow behaviour around the manikin (Figure 6.3). The initial stage for the first gait cycle is completed in the first second (cadence of 2 steps/second) and the induced flow field caused by the moving manikin is shown in Figure 6.3a. Streamlines originating from the front-right-hand side of the body wrap around and then curl back into the manikin body. This suggests strong flow entrainment caused by the moving manikin that pushes the air that is in front of it, making way for the manikin to occupy the space. The displaced air then curls back around the body taking up the void space left behind by the manikin. We notice that the streamlines remain close to the body for the very first step (t = 0.25 - 0.5 secs) and grows wider at the second step (t = 0.75 - 1.0 secs). During the third step cycle between t = 2.25 s to t = 3.0 s (Figure 6.3b) the streamlines are wider as it wraps around the body before getting pulled back into the centre. The streamlines move furthest around the middle of the body while it is thinnest near the head and feet. Generally, the streamlines don't show significant updraft to potentially re-disperse floor lying particles into the breathing region. The streamlines near the feet remain close to the floor, while streamlines at knee height will rise as it moves backwards.

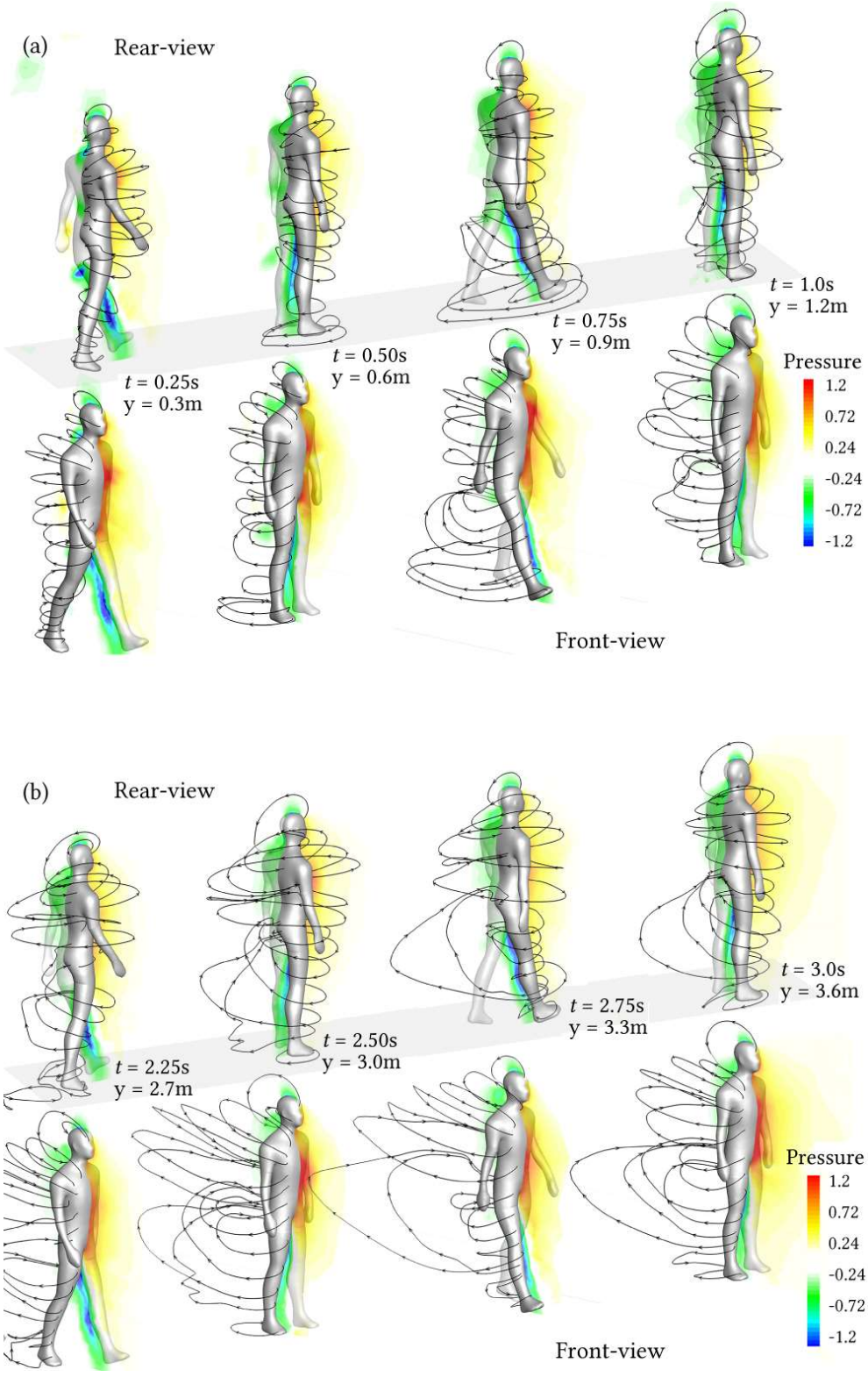

Figure 6.3 3D streamlines generated from the right side of the body under a walking speed of 1.2m/s. A pressure contour is overlayed to demonstrate the regions of high pressure and low pressure, determining the flow direction. (a) First gait cycle which occurs between t = 0.0sec to t = 1.0. (b)Third gait cycle which occurs between t = 2.0sec to t = 3.0

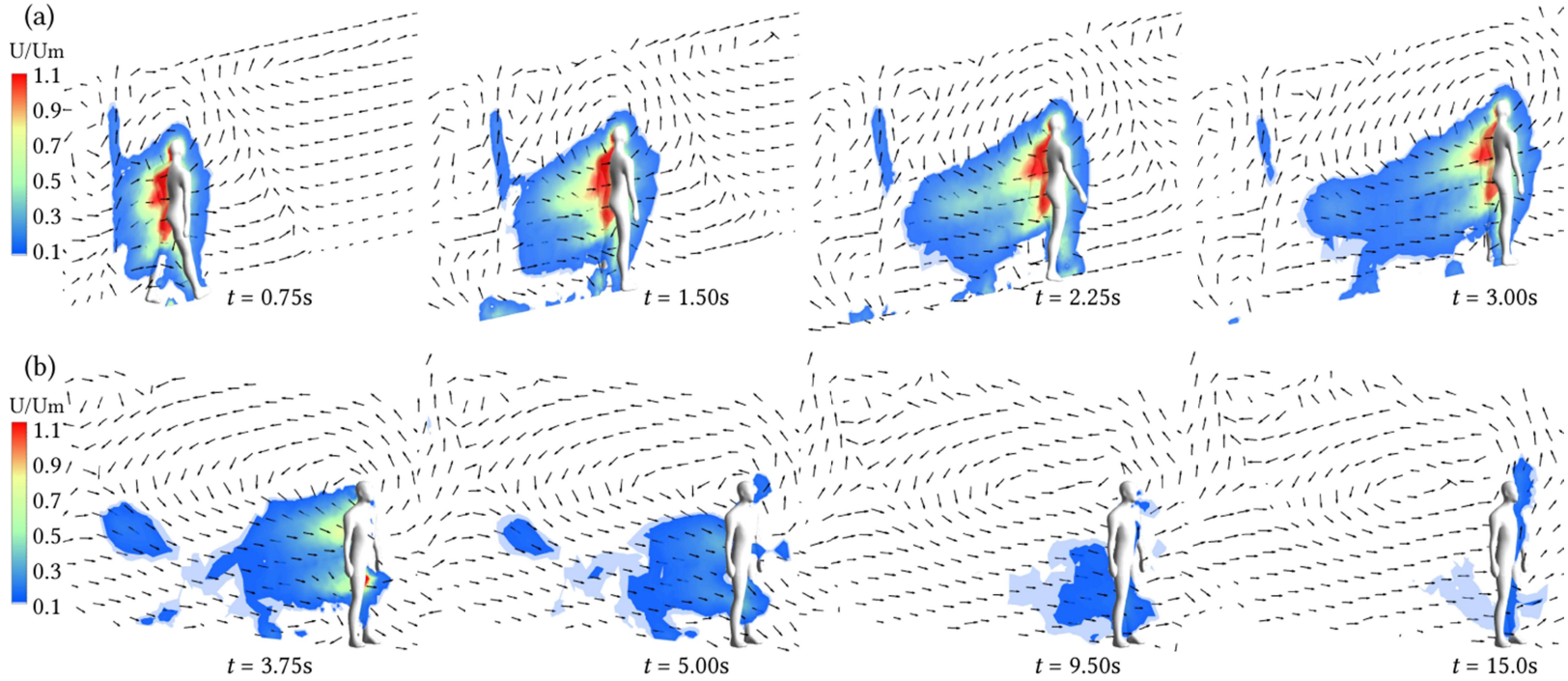

Figure 6.4 Velocity contour and vectors on the mid-plane (x = 0m) (a) during walking period (t =0.75s, 1.5s, 2.25s, 3.0s) and (b) after it stopped (t =3.75s, 5.0s, 9.5s, 15s). The velocity contours had a minimum velocity capped for dimensionless velocities below $U/U_m = 0.10$

6.3.2.2 Temporal development of the wake flow

The transient flow field is shown through the midplane velocity contour and vector plot (Figure 6.4) for the walking speed of 1.2m/s. The walking period occurs in the first 3.5 seconds (Figure 6.4a) where high velocities are found at the manikin body surface from the relative motion between the manikin and surrounding air. In the upper body this is evident from the high velocities along the body and a trailing wake forms. Vectors show the fluid moves upwards and around in a semi-circle from the head returning into the wake as it becomes entrained into the flow. Velocity vectors in the wake return inwards into the manikin body. In the front of the body the vectors are directed forwards suggesting that the fluid is pushed away as the body moves through the flow field. The airflow in the lower body is dominated by the alternating acceleration and deceleration of the swinging limbs and pivot phases and was significantly affected by the swinging leg. After the manikin came to a stop the wake region reduces and its residual momentum carries the fluid forwards moving over the manikin body. Flow accelerated through gaps between the limbs (arms, legs). After 15s we found the thermal plume became evident with a rising flow from the head.

6.3.2.3 Comparisons of instantaneous velocity at different distances

Figure 6.5 compared the instantaneous stream-wise velocity component along horizontal lines on the mid-plane at different heights, z = 0.1 m (ankle height), z = 0.5 m (knee height), and z = 1.5 m (breathing region head height) after the manikin walked for 2.1 meters (half its journey) and 4.2 meters (final location) respectively. Generally, the velocity variation at the ankle and knee heights are small. Larger fluctuations are found in the wake behind the body when the manikin is still walking at y = 2.1 m position compared to when it comes to a stop at y = 4.2 m. At knee height the fluctuations are increased but we don't see any discernible pattern, such as any flow acceleration through the through the legs. Upon inspection the lack of flow between the leg gap is due to the swinging motion of legs during the gait cycle, and in fact the flow passing through never has a chance to develop through the legs. At head height (z = 1.5 m) the instantaneous velocities are much greater ranging from -0.6m/s to 0.6m/s. During walking at position y = 2.1 m, the streamwise velocity is positive as it's pushed forwards from the moving body. It travels over the top of the head where it recirculates and moves into and behind the body represented

by the dip in the curves and the flow velocity changing from 0.6m/s to -0.6m/s for the fastest walking speed. The trailing wake region behind the head dissipates downstream and the velocity decays to zero. The flow patterns between the y = 2.1 m and y = 4.2 m are very similar.

The instantaneous velocities can misrepresent the overall flow behaviour because no other times are considered. On the same horizontal lines (z = 0.1 m, z = 0.5 m, z = 1.5 m), the velocity profiles behind the body within 0.9 meters were time-averaged to examine the flow pattern. To be consistent with Figure 6.5 the velocity was time-averaged during prior one gait cycle (1s) at the positions where the manikin was at y = 2.1 m and y = 4.2 m. Thus, each profile represents a one second time average of the wake 0.9m behind the manikin as it was moving. Figure 6.6 shows the velocity at ankle height (z = 0.1 m) is

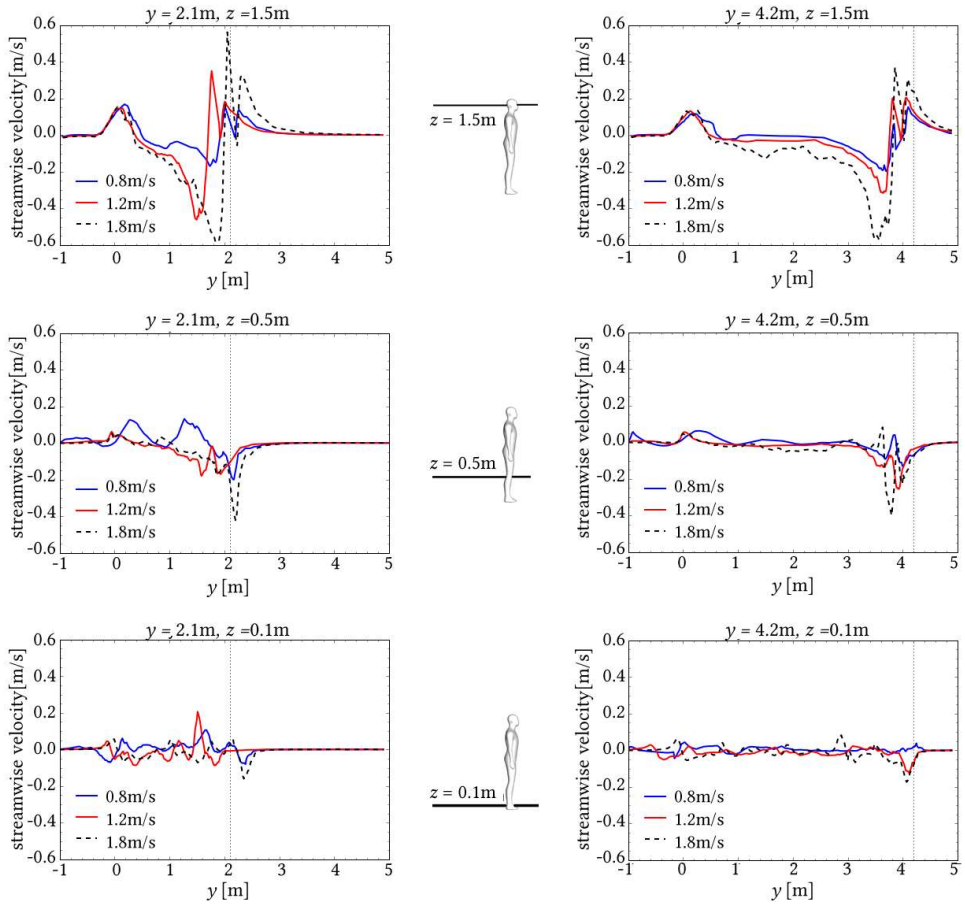

Figure 6.5 Stream-wise velocity along horizontal lines on the centre plane at different heights (z = 0.1m, z = 0.5m and z = 1.5m) after the manikins walked for 2.1 meters and 4.2 meters under different walking speeds (0.8m/s, 1.2m/s and 1.8m/s) The vertical dashed line in each figure represents the position of the manikin.

relatively random with a preference of low negative streamwise velocities for the y = 2.1 m position. For y = 4.2 m the streamwise velocity in the wake becomes positive far away from the manikin. At knee height (z = 0.5 m) the time-averaged velocity profile now shows a clear flow pattern not previously found in its instantaneous profile. There is a negative velocity near the knee suggesting penetration of an air jet through the legs to the rear. The velocity changes to positive further downstream from the knees where flow entrainment is bringing the air back into the wake. At head height (z = 1.5 m) and close to the head, the velocity is very high caused by the moving body inducing the flow.

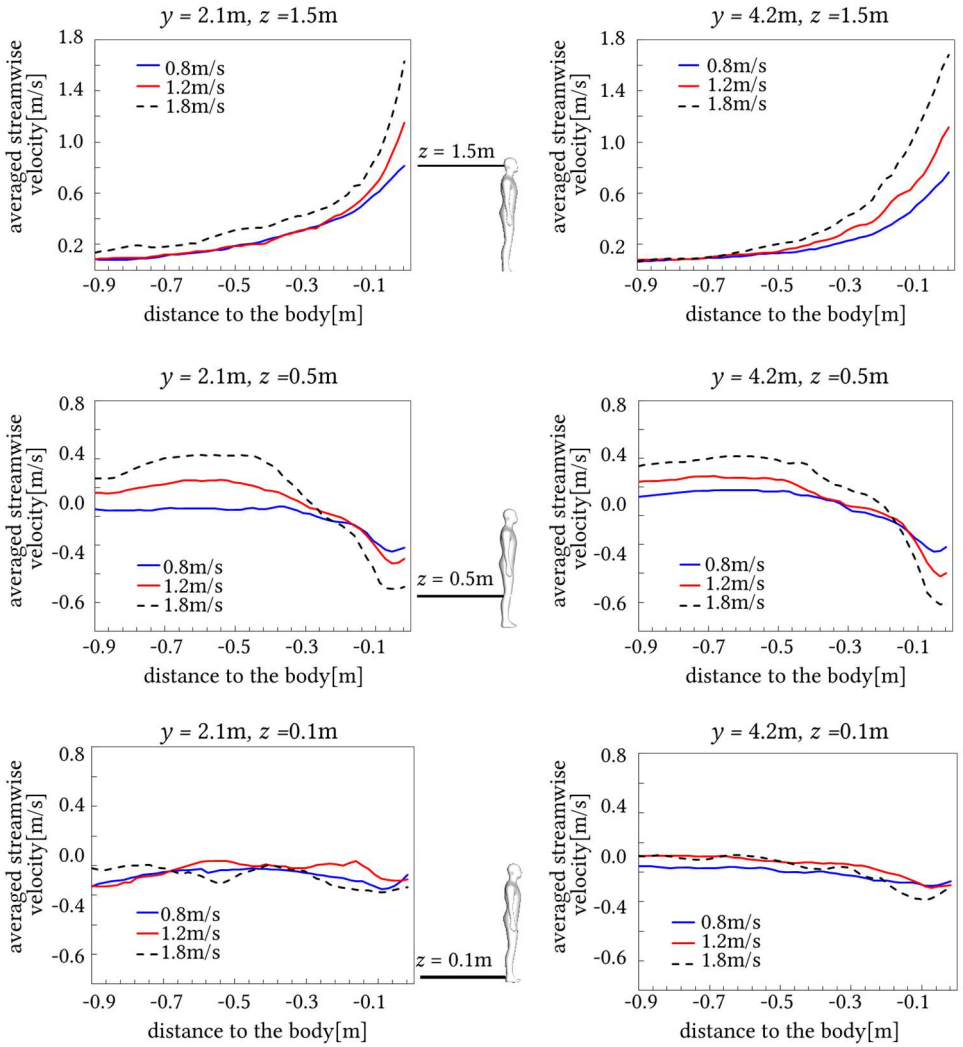

Figure 6.6 Time-averaged stream-wise velocity along a horizontal line extending 0.9m behind the manikin on the central plane at different heights (z = 0.1m, z = 0.5m and z = 1.5m) and corresponding to the positions given in Figure 6.6.

For each of the walking speeds the peak velocities correspond to its walking speed. Downstream from the head, the velocities decrease parabolically as the wake dissipates its energy into the flow field. The profiles show flow entrainment is evident in the far field at knee and ankle height and for the head region this occurs throughout the entire length.

The time-averaged vertical velocity profile (Figure 6.7) provides better insight to enhancements for particle redispersion because it may induce particle lift. At the ankle and knee heights, the peak velocities in the positive (upwards) direction is relatively small with the peak value approximately 0.2m/s. This only occurs while the manikin is in mid-motion at the y = 2.1 m position. At

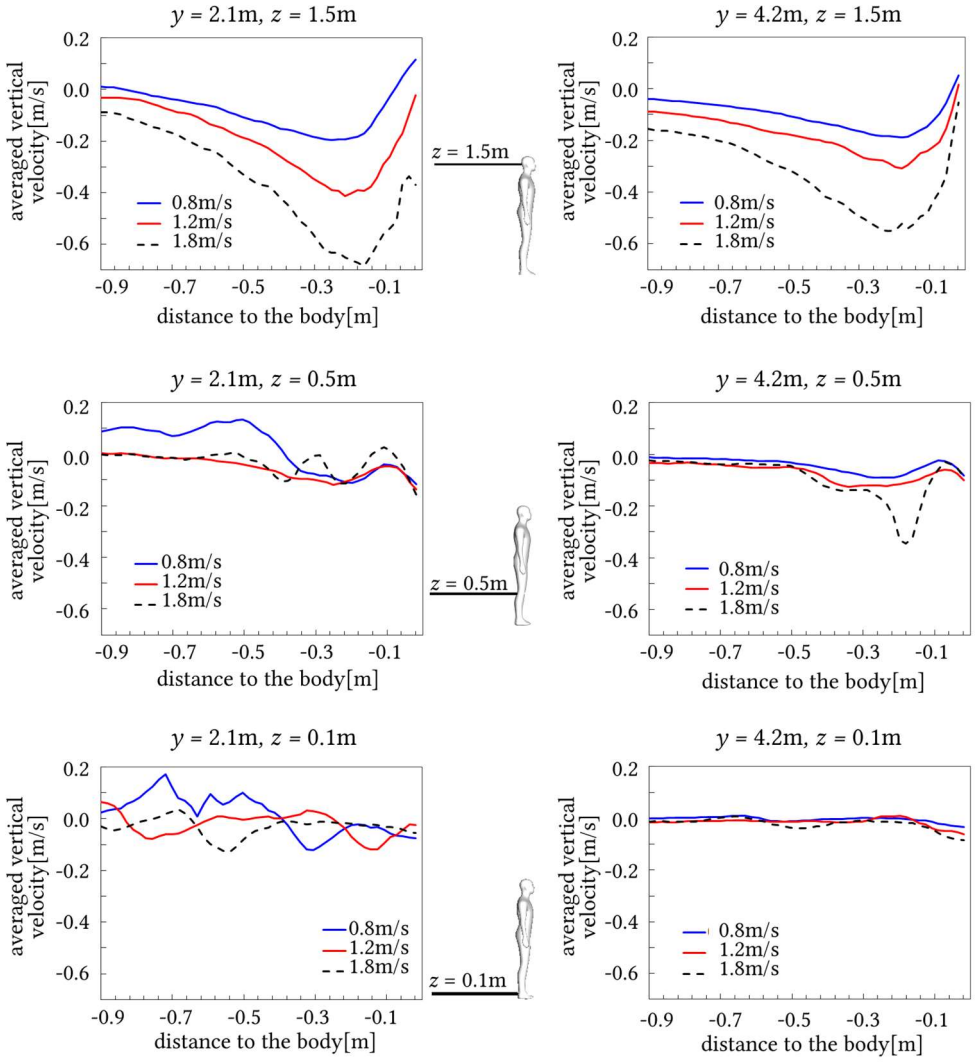

Figure 6.7 Time-averaged vertical velocity component along a horizontal line extending 0.9m behind the manikin on the central plane at different heights (z = 0.1m, z = 0.5m and z = 1.5m) and corresponding to the positions given in Figure 6.6.

the y = 4.2 m position the velocities are very low and even negative (downwards). This suggests particles on the floor may not be sufficiently disturbed and able to lift off the ground into the air. At head height (z = 1.5 m) the velocities are positive (rising upwards) at the top of the manikin head. Moving downstream the velocity changes direction and reaches a maximum negative value as flow separation and recirculation occurs, before dissipating to zero. The velocities are much greater in magnitudes at head height. Therefore, airborne particles at this height will be redispersed and dynamically moving within the wake.

6.4 Effects of Manikin Movement on Particle Dispersion

6.4.1 Average Particle Concentrations at Different Heights

For a given distance travelled, a slower walking speed results in a longer time for the motion-induced wake to develop and interact with particles. Based on the flow field results, the airflow in the front of the feet and legs had negative

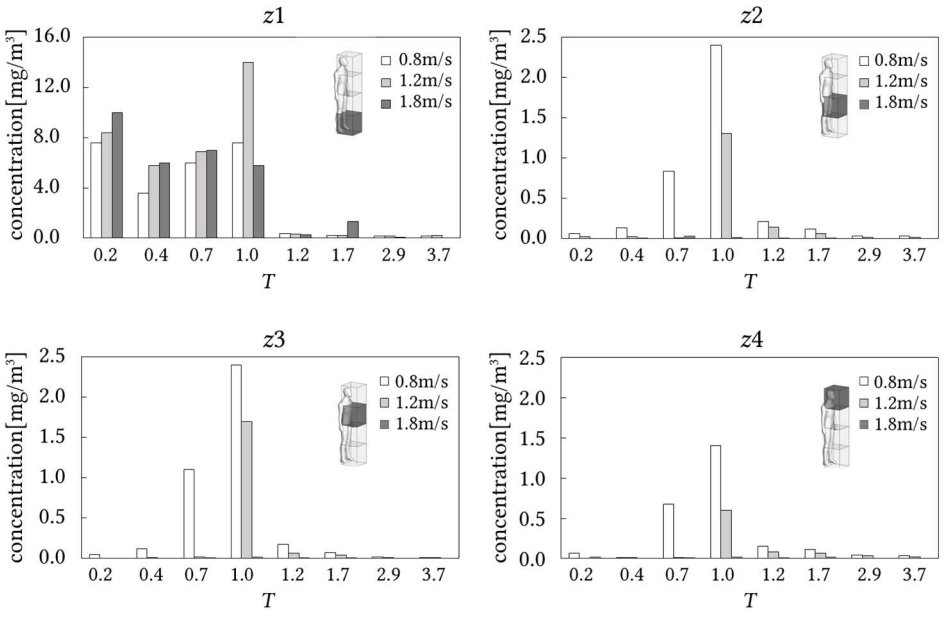

Figure 6.8 Average particle concentration [mg/m³] within the cubic regions in the front of the body at different heights for dimensionless time T = t=(S/U_m), where t is the walking time non-dimensionlized by the walking distance S = 4.2m under various walking speed U_m = 0.8m/s, 1.2m/s and 1.8m/s

vertical velocity components which tended to increase in strength with the walking speed. Since the particles were uniformly distributed across the floor, the lack of significant positive vertical velocities suppresses the possibility of particle suspension. To compare the unsteady influences under different walking speeds, the dimensionless time is defined as $T = t/(S/U_m)$, where t is the real walking time and $S//U_m$ represents the time to travel a distance of S = 4.2 m under different walking speeds ($/U_m$). Thus for all walking speeds, the dimensionless time for the manikin walking period was T = 1. The residual wake movement afterwards was examined until T = 3.7.

Figure 6.8 shows the averaged particle concentration inside four cubic volume regions taken in the front of the body. Each region has width 0.6m, length 0.6m and height of *z1* = 0-0.45 m, *z2* = 0.45-0.90 m, *z3*= 0.90-1.35 m, and *z4* = 1.35 - 1.80 m. The lowest region, *z1* exhibited the greatest concentration levels and in this region the walking speeds correlates with increased particle concentration. At T =1, the highest concentration overall is found and this occurred for a walking speed of 1.2m/s. After the manikin stopped walking there is a rapid reduction in particle concentration.

The remaining volume regions, *z2, z3, z4* showed a significant decrease in concentration where the peak values for all walking speeds was just under 2.5mg/m^3. At head height in the breathing region the concentration reaches 1.5mg/m^3 caused by the downwards velocity component produced by at the head separation. The particle concentration in these regions was inversely proportional to the walking speed where the slowest walking speeds produced the highest concentration levels. The wake flow analysis (Figure 6.3 to Figure 6.7) showed that a higher walking speed generally produced stronger downwash airflow onto the lower body from the flow separation occurring at upper body. The fluid-particle interaction time was longer for the lower walking speed; thus a stronger particle dispersion was observed. The higher walking speed generated larger negative velocity component and a broader wake region with less fluid-particle interaction time which hindered the particles ability to enter the upper body region. We also observe the after effects of the wake and flow disturbances influencing the particle redispersion. The peak particle concentration levels occur at T = 1, suggesting that the particles are transported into the breathing region, after the wake has formed and begins to flow past the body that is now not moving.

6.4.2 **Particle Dispersion During Walking**

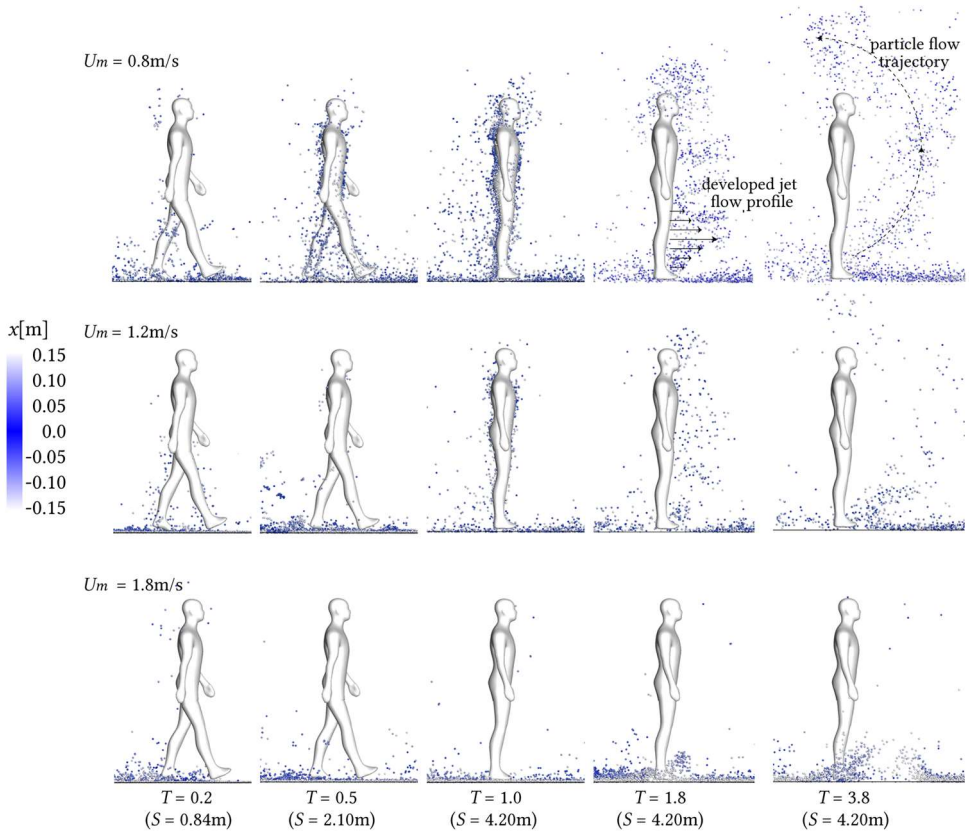

Figure 6.9 Visualisation of particle redispersion caused by the walking manikin (from T = 0.2 (travelled 0.84m) to T = 1.0 (travelled 4.2m)) and after the manikin has stopped walking (from T = 1.0 to T = 3.8). The walking speed was U_m = 0.8m/s, U_m = 1.2m/s and U_m = 1.8m/s and the total travelled distance was S = 4.2m

shows the particle dispersion within -0.15m to 0.15m laterally from the midplane (x -coordinate) of the body. The walking speed of 0.8m/s is shown as this produced the highest particle concentrations. The particles were coloured by its lateral distance from the midplane the x -coordinates (lateral direction) that the deepest colour represents a position closest to the central plane (x = 0 m). During the early walking stage, the floor-distributed particles were vigorously disturbed and became entrained into the flow. The negative stream-wise velocity at knee-height (Figure 6.6, z = 0.5m) is caused by air flow passing through the gap between the legs, transports the suspended particles from in front to the back. Particles are found close to the body, mimicking the wrap around streamlines in Figure 6.3.

When the particles have moved into the wake they gradually propagate to higher regions as the airflow produced by legs flowed upwards into the back. The particles then remain close to the back and transported with the manikin body (from T = 0.50 to T = 1.00). The particles in front of the body move towards the body and also move upwards into the breathing zone under a strong upward airflow induced by the upper body. At T = 0.93 we see the dispersed particles are predominantly wrapped around all different parts of the body.

At T=1.00 the manikin has stopped walking, and the residual airflow continues to transport the particles forwards. From T = 1.20 to T = 3.80 the particles move forward separating away from the body. The jet-like flow through the leg gap accelerates the particles through forming a parabolic profile (T = 1.80). As the airflow continues to move forward and dissipates, the thermal plume from natural convection becomes significant and the particles move forwards and upwards in a circular profile (T = 3.80). As a generalisation we see that after the manikin stopped walking the particles moved forwards with the residual wake momentum, and then upwards due to the thermal plume effect. It is only in the period of T = 0.93 to T = 1.80 that the particles move past the manikin breathing region.

6.5 Conclusion

This chapter presented transient simulations of the wake flow induced by a moving thermal manikin with swinging limbs under different walking speeds. Its influence on particle dispersion from the floor was also investigated. Particle suspension caused by human activity and movement was influenced by the stratified airflow characteristics induced by the different body parts and its kinematics - the leg swing produced downward airflow in front while upward flow in back region, which transports particles toward the upper region during walking. However, a higher walking speed produced stronger downward airflow in the front of the body, which prevented the suspension of floor particles to rise to the upper body regions. The upper body produced upward flow in front of the body which caused particles to rise quickly into the breathing zone. At the back of the upper body a strong downwash was formed and caused particles to almost stick to the back of the body while in the manikin was moving.

The particle concentration comparison showed a higher walking speed produced less vertical transport of particles in front of the body thus helpful to reduce the exposure level to contaminants. While at a lower walking speed at 0.8m/s, particles were continuously transported to the upper region due to more upwards velocities in the wake structure. Additionally, the longer walking time leads to longer fluid-particle interaction and residence time for particle exposure.

This computational study of a very realistic moving manikin redispersing particles of the ground is a first step to better understand the effects of occupant activity on particle exposure and indoor air quality. As it's a first study there remains a caveat on the modelling efforts. This includes the assumption the feet not striking ground, thus no impact of foot strike is considered. Particle source was also limited to the floor region only, and in reality, there is background airborne particle concentrations. Concentration sources could also be localised in one part of a room where a contaminant source may be found. We also only investigated one particle type and size, which was wood dust having spherical diameter of 2.5 μm and density of 700kg/m^3, thus its aerodynamic diameter is 2.09 μm. A wider range of particle sizes will be investigated in future. The manikin body was also one shape and other body shapes will produce different flow fields which will be discussed in the following chapters.

Chapter 7
Smoke Visualisation of Three Moving Manikin Models

The main findings of this chapter have been published in:

- **Tao, Y.,** Inthavong, K., Petersen, P., Mohanarangam, K., Yang, W., Tu, J. Y. (2018). Experimental visualisation of wake flows induced by different shaped moving manikins, *Building and Environment,* 142, 361—370.

  DOI: 10.1016/j.buildenv.2018.06.018. ***IF = 4.539, Q1***

Traditional smoke visualisation is based on stationary objects with a moving fluid. This chapter presents wake flow from moving manikins investigated by a new smoke visualisation technique. Three scaled models $1/5^{th}$ of realistic manikin models were used, including two body shapes (thin and wide) and two gestures (standing and walking). Smoke visualisation was produced by a chemical reaction between acetic acid (CH3COOH) and cyclohexylamine (C6H13N) to generate smoke. Highspeed photography and image processing techniques were used to determine the qualitative and quantitative data on the airflow patterns and separation points from the manikin motion. Detailed flow separation images showed that regular vortices were produced off the head and the shoulder, while flow separating at the hand swirled behind and inwards. Analysis of flow over the head revealed how the separation point shifted from the back of the head to the front as the velocity decreased. When the manikin came to a stop, the results also showed increased airflow activity around the face which increases the risk of inhaled particulate matter from the surroundings. Image processing analysis produced quantitative data which included the vortex shedding frequency coming off the shoulder, and the separation point from the manikin head. It is expected that the experimental results will provide validation data for future computational fluid dynamic (CFD) modelling results.

7.1 Introduction

Human activity has significant influence on indoor airflow patterns due to wake flows and vortex shedding (Flynn and Ljungqvist, 1995, Heist et al., 2003, Johnson et al., 1996, Li et al., 2014) that disturb localised suspended particles (Anthony and Flynn, 2006, Inthavong et al., 2009, Inthavong et al., 2013b, Ferro et al., 2004). Consequently, airborne contaminants are redispersed in the air that can lead to severe and/or fatal consequences in enclosed indoor environments *e.g.* surgery theatre (Brohus et al., 2006), clean rooms (Choi and Edwards, 2008), and confined spaces such as airline cabins (Poussou et al., 2010, Mazumdar et al., 2011). Qian and Ferro (2008) demonstrated the effects of human activity where 'heavy and fast' walking produced higher resuspension rates compared to less-active walking. Similarly studies investigated human interactions with floor type (You and Wan, 2015), dust type and contaminant concentration in dust loads (Gomes et al., 2007).

Early studies of the effect of human bodies on contaminant transport used stationary human models/manikins. Kim and Flynn (1991), Kulmala et al. (1996a)'s stationary manikins were placed in an open-ended wind tunnel, and tracer gases were released from different locations to visualise boundary layer separation, and the size and location of the wake region. Computational Fluid Dynamics (CFD) studies (Edge et al., 2005, Murakami et al., 1999, Hayashi et al., 2002, Ge et al., 2013) have provided detailed flow structures of unsteady wake regions and contaminant transport. For models/manikins that are stationary, the results neglect the effects of movement by the body though (Brohus et al., 2006) applied distributed momentum sources to represent movement. Furthermore, simplified geometries such as vertical finite cylinders and cuboids have been used as substitutes for human bodies (Poussou et al., 2010, Thatcher et al., 2004), and this also leads to discrepancies between realistic and cylindrical geometries (Edge et al., 2005, Tao et al., 2017a).

Recent experimental studies have focussed on the effects of human activity on the fluid wake dynamics by using moving models. Han et al. (2014) used a full-scale thermal manikin and measured the dynamic airflow with hot-wire anemometers and found a limitation of the method was that measurements were taken at a point (from the probe sensor) and thus unable to obtain comprehensive information of the whole flow field. Poussou et al. (2010), Poussou and

Plesniak (2012), Poussou and Plesniak (2015) conducted small-scale PIV and Planar Laser Induced Fluorescence (PLIF) measurements to qualitatively capture the wake flow from a moving block and contaminant transport inside an airline cabin. Luo et al. (2017) conducted PIV measurements on a small-scale cabin with a moving manikin, and observed flow patterns such as symmetric eddies, upward vortex and a strong downwash in the wake flow along the vertical centre plane. Computational studies also observed wake flow patterns and vortices that caused significant dispersion of contaminants in the environment (Brohus et al., 2006, Hang et al., 2014, Oberoi et al., 2010, Tao et al., 2017a, Choi and Edwards, 2012, Choi and Edwards, 2008).

Although PIV experiments provide detailed flow field information, extremely large data sets are needed to achieve statistical average for each image pair covering a small field of view, and at each instantaneous moment in time – and each instantaneous time produces different manikin positions. To date there are limited experimental studies of wake flow induced by a moving human. This is partly due to the challenges in flow visualisation to capture a moving object compared with a traditional fixed object with a steady state flow. Smoke visualisation provides a qualitative understanding of the gross flow field. Recent studies have demonstrated the ability to capture separation points, reattachment points, and vortex shedding phenomena (Sohankar et al., 2015). Moreover, with high speed photography and image processing, quantitative data is produced for validating CFD simulation data of moving human subjects/manikins.

The objective of this chapter is to present an experimental technique for investigating wake flow induced by a moving human manikin. The smoke generation involved a chemical reaction between a chamber filled with saturated air with acetic acid and a manikin dabbed with cyclohexylamine. When the two chemicals came into contact, smoke was produced. High speed photography captured the transient wake flow and the image processing was used to produce quantitative data. This allowed flow visualisation of a moving object which was not possible with traditional smoke visualisation that has a moving fluid flowing past a fixed smoke generation location.

7.2 Method

The techniques of smoke visualization were introduced in Section 3.6. In that setup, three 1/5th scaled manikins (a slim manikin in standing gesture, model

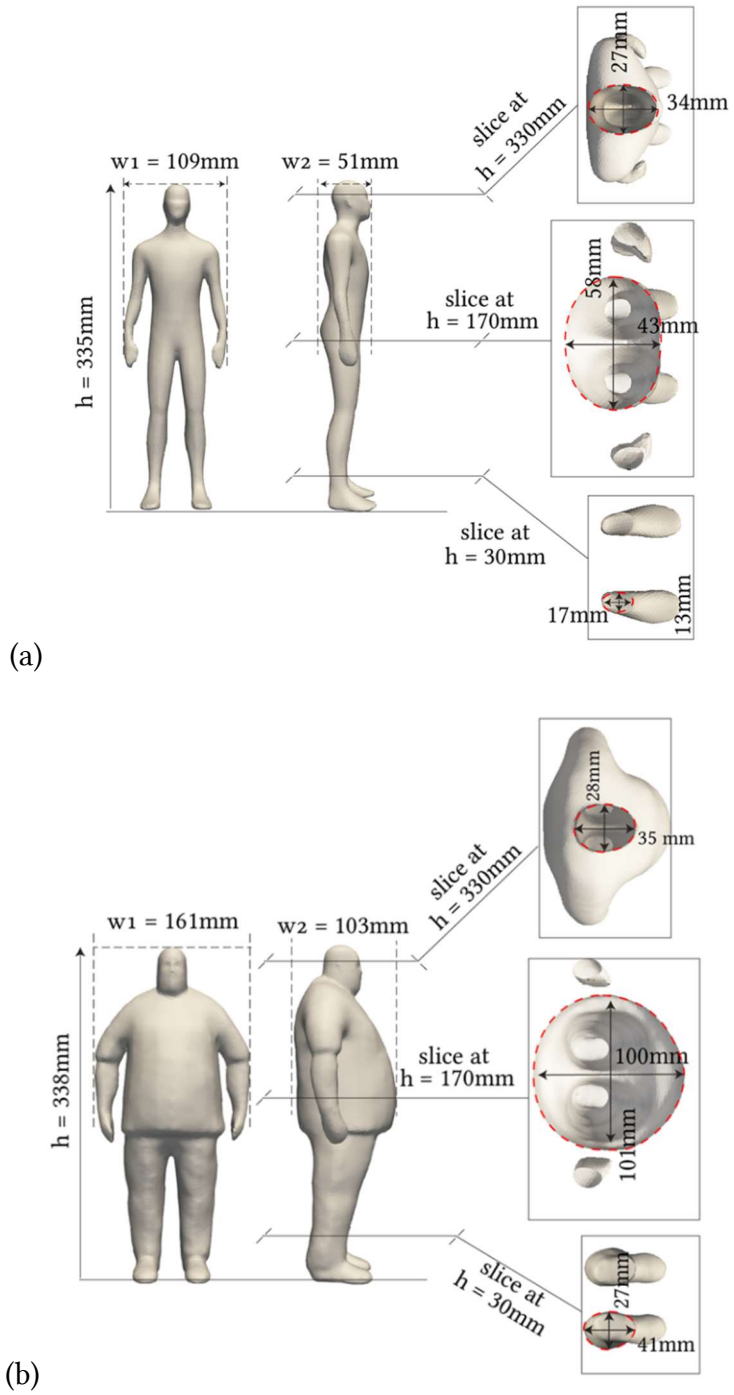

Figure 7.1 Detailed dimensions of the two body types (a) Model #1: slim manikin in standing gesture and (b) Model #3: larger bodied manikin in standing gesture

#1, the same slim manikin in walking gesture, model #2 and a larger bodied manikin in standing gesture, model #3) were 3D printed at RMIT University's Advanced Manufacturing Precinct (Melbourne, Australia) and shown in Figure 3.2. The models come from our library of 3D generated CAD models which include different human manikins in various poses. The manikin selection was based on slim body build with height of 170cm. The second body was selected based on the need for a completely different shape and size to demonstrate the effects caused by different geometries.

Detailed dimensions of the two body types (slim and large bodies) are given in Figure 7.1. This included height, width, breadth, and three transverse plane cross-section slices taken at the ankle, hips, and eye-level. The cross-section slice outlines showed approximate ellipsis. For the slim body the ellipse is aligned anteroposterior at the ankles and head, while at the belly it is aligned laterally. For the large body the ellipse is almost circular. The aspect ratio based on the width is 3.1 for the slim body and 2.1 for the wide body. These dimensions quantify the shape and size of the body which influences flow dynamics and provides analysis for local Reynolds numbers and describing separation points.

The manikins were mounted onto a rack-and-pinion travelator that moved the manikin inside a holding chamber through a sliding door and across the floor of the test chamber. A limitation of this setup was the maximum possible speed of the rack-and-pinion motor which must accelerate to a maximum of 0.95m/s and then decelerate to 0m/s over 700mm.

	Height (m)	slim body		larger body	
		D_h (m)	*Re*	D_h (m)	*Re*
head	0.33	0.029	1861	0.030	1926
waist	0.17	0.047	3017	0.100	6417
ankle	0.03	0.014	899	0.030	1926

Table 7.1 Local Re for ankle, waist, head of the slim and the larger body

7.2.1 **Manikin Movement**

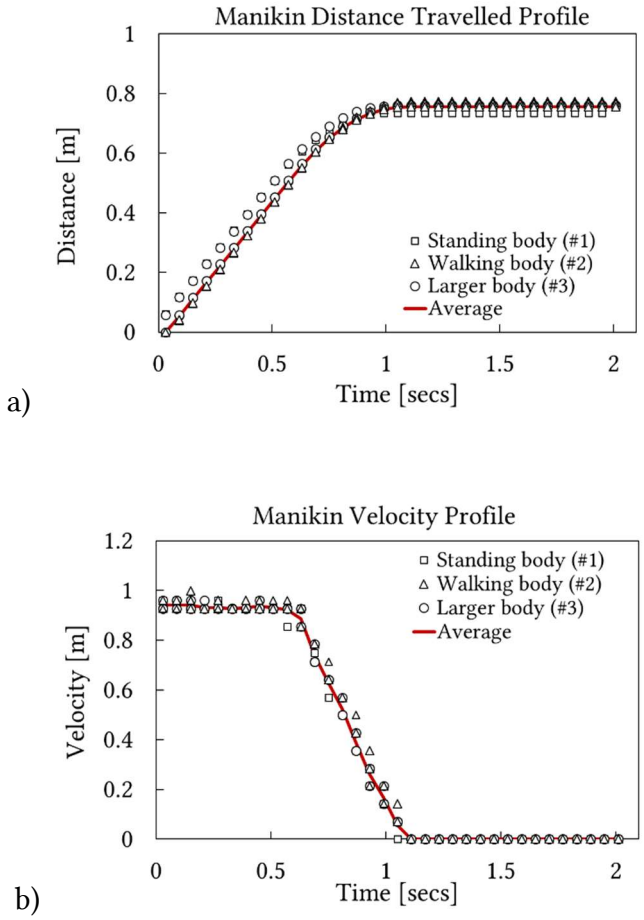

Figure 7.2 (a) the travelled distance profile where the total distance is approximately 765mm and (b) the manikin velocity profile exhibiting regions of peak velocity, deceleration and coming to a complete stop.

The distance travelled by the manikin as a function of time was averaged over multiple runs (nine in total for each manikin) and is shown in Figure 7.2a. The manikin started from rest inside the holding chamber and accelerated to 0.95m/s. Based on a peak velocity of *0.95m/s* the corresponding Reynolds numbers for flow separation across the manikin head, waist and ankle for the slim body are 1861, 3017 and 899 respectively; and for the larger body are 1926, 6417, 1926 respectively. The Reynolds numbers were calculated from hydraulic diameters at each location, of which the height and cross-sectional plane were shown in Table 7.1 and Figure 7.1.

The high-speed camera began recording when the manikin moved 100mm (acceleration period) inside the chamber. This ensured the acceleration period

had been completed, and the manikin was moving at constant velocity. At this point, the manikin was moving at a constant peak velocity u_{peak} = 0.95m/s from t = 0s to t = 0.6s. A constant deceleration at a rate of -1.9m/s^2 occurred thereafter, and the manikin came to a complete stop at t = 1.1s, after travelling 765mm. Statistical analysis of all profiles showed a variation of ± 4 % from the averaged profile, attributed to high mechanical forces associated with rapid acceleration and deceleration over a short distance.

Figure 7.2b shows that over the short distance covered by the manikin, there are three different velocity profiles: constant walking; deceleration; and stationary, which is remarkably common in indoor environments (e.g. offices, hospital wards, clean rooms, and manufacturing spaces). It is expected that within each walking phase, different wake flow characteristics will be generated.

7.3 Smoke Flow Visualisation

Fabric material was stuck onto seven locations on each manikin to visualise different wake features. During manikin motion, smoke originating from different sources mixed and overlapped in the wake, and to minimise this, the seven locations were split into three groups. The grouped locations were:

(i) forehead, left waist and left knee;
(ii) backline; and
(iii) shoulder, hand and feet.

The captured images were also categorised into three walking phases: constant velocity (t = 0s to t = 0.6s); deceleration (t = 0.6s to t = 1.1s); and stationary (t = 1.1s to t = 3.0s).

7.3.1 **Smoke from Forehead, Left Waist and Knee**

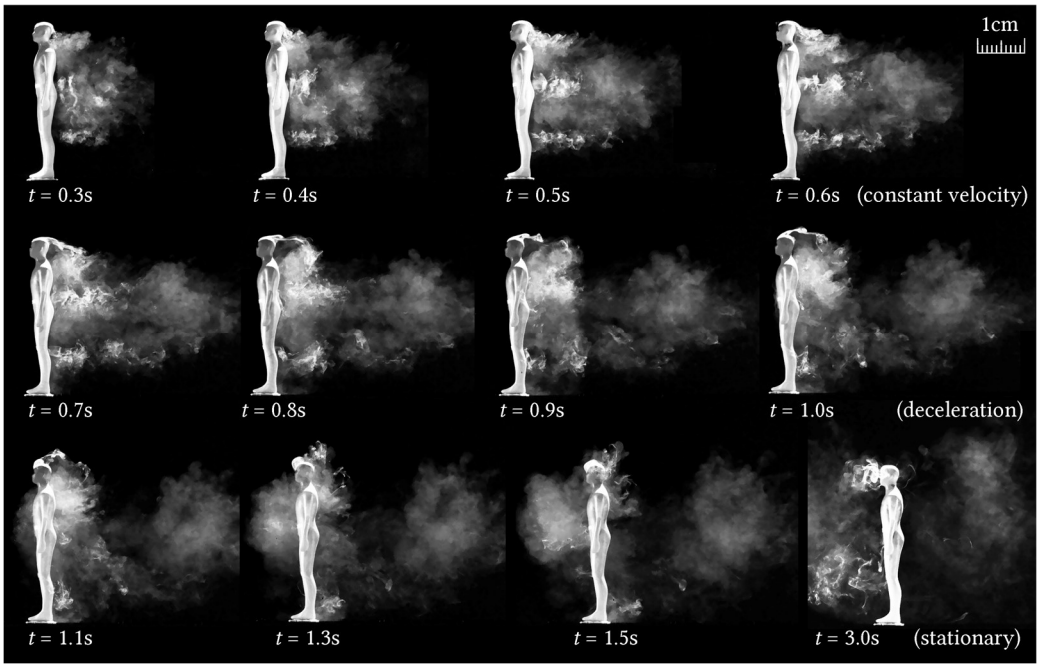

Figure 7.3 smoke generated at (i) the head, left thigh and left knee during maximum speed (0.3s to 0.6s); deceleration (0.7s to 1.0s) and stopped (1.1s to 3.0 s) for the slim body.

The results for the slim manikin at the (i) forehead, waist, and knee location are shown in Figure 7.3. As the manikin entered the chamber, smoke was produced in a small region, and formed a larger trailing wake filled by new vortices shed from the body. The wake region resembled a triangular shape (t = 0.5, 0.6s), which consisted of the downwash smoke shed from the head towards the back, and the smoke from the left waist and knee shed downstream. The smoke generated from the left knee rotated slightly upwards at the back and merged into the wake region.

Flow separation from the head was captured clearly. A delayed separation occurred at the back of the head during the constant velocity period. During the deceleration period the manikin momentum reduced, and the separation point at the head shifted forwards (early separation). The near wake behind the body also reduced as it continued to move forward, colliding into the body and rolling upwards.

After the manikin stopped moving the wake moved past the torso on both sides of the body. The wake continued forward and rolled up the back of the

body and over the head. The smoke rolled from the back of the head and over to the front, where the separation point was at the forehead. The smoke plume surrounded the manikin face and breathing region, which enhances contaminant inhalation exposure. Some smoke remained wrapped around the face up to t = 3.0s.

7.3.2 **Effect of Body Shape - Slim and Larger Manikins**

The larger body (model #3) with an aspect ratio (height/width) of 2.1 had a taller wake region generated from the head, the hand and the knee (Figure 7.4) compared to the slim body (model #1, which had an aspect ratio of 3.1, see Figure 7.3). The slim body formed a triangular shaped wake which ended at the shins, while the larger body had a wake region that almost reached the ground. The wake of the larger body is similar to airflow patterns of a solid cylinder mounted on the ground (Wang et al., 2009), where the wake generated at the knees formed span-wise vortices that roll downstream. Flow dynamics near the ground are influenced by a base vortex which is found close

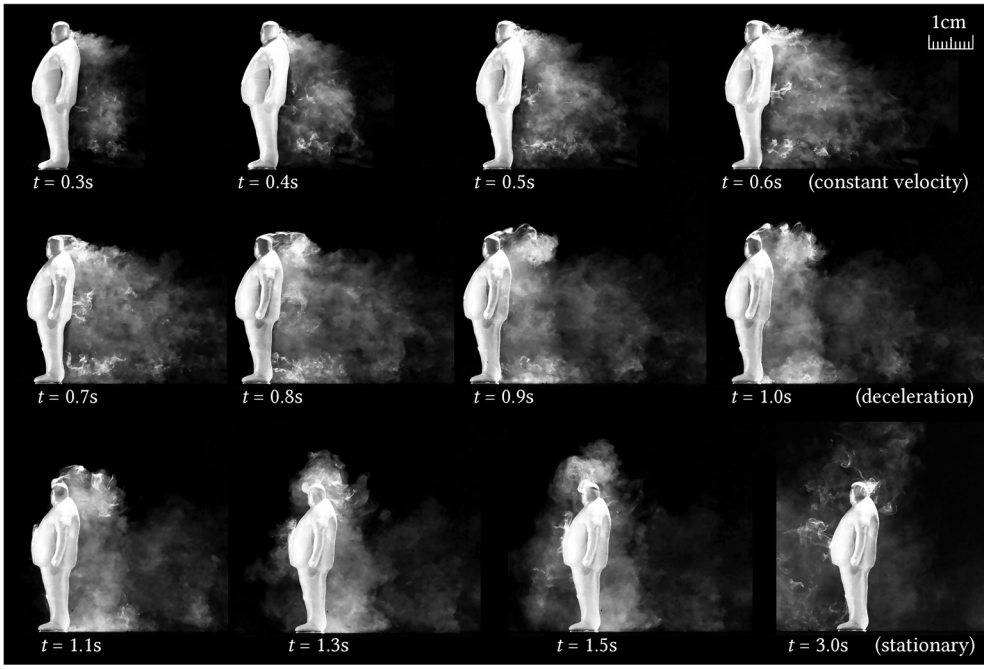

Figure 7.4 smoke generated at (i) the head, left thigh and left knee during maximum speed (0.3s to 0.6s); deceleration (0.7s to 1.0s) and stopped (1.1s to 3.0s) for the larger body

to the junction of the body surface and ground. For example, observations of the wake region from cylinders (Rostamy et al., 2012), showed upwash flow in the region close to the ground and downstream of cylinders. The upwash flow effect weakens with reduced aspect ratio. This was consistent with observations from the manikins where downstream of the slim body, the smoke was pushed towards the mid-height of the body, while the upwash was negligible downstream of the larger body, thus the generated smoke stayed attached on the ground. When the manikins decelerated, the slim body had a majority of the smoke accumulate behind the back below the shoulder. In the lower half of the slim body, the smoke followed the shins and gradually moved down to the feet (Figure 7.3). For the larger body, the accumulated smoke ascended behind the head, while in the lower body it remained attached on the ground behind the feet (Figure 7.4).

The differences in body shapes showed distinct differences in flow patterns in the wake region. For contaminants originating around the body, a larger body would have a more remaining close to the ground due to the weaker upwash in the downstream near-ground region.

7.3.3 **Smoke from Backline**

Figure 7.5 shows smoke produced from (ii) the back line for the slim body which was weak between t = 0.0s to 0.4s, indicating low convective flows. Between t = 0.4s to t = 0.6s, the smoke ascended with a clockwise rotation and rolled up the back of the head and accumulated there. Meanwhile a small region of the smoke moved downwards behind the thigh. This suggests two directions of rotation: i) a strong clockwise upwards rotation behind the upper body as air from the front meets the flow from the back forming a strong downwash towards the back; ii) and a weak rotation behind the lower body brought the smoke down, influenced by the jet pushing through the gap between the legs and this formed an anti-clockwise rotation towards the back.

During deceleration (t = 0.7s to 1.0s), the downwash towards the back reduced in strength. The reduced momentum caused less smoke to follow up the head, similar to the wake separation observed in Figure 7.3. The smoke rotated up gradually and diffused behind the head.

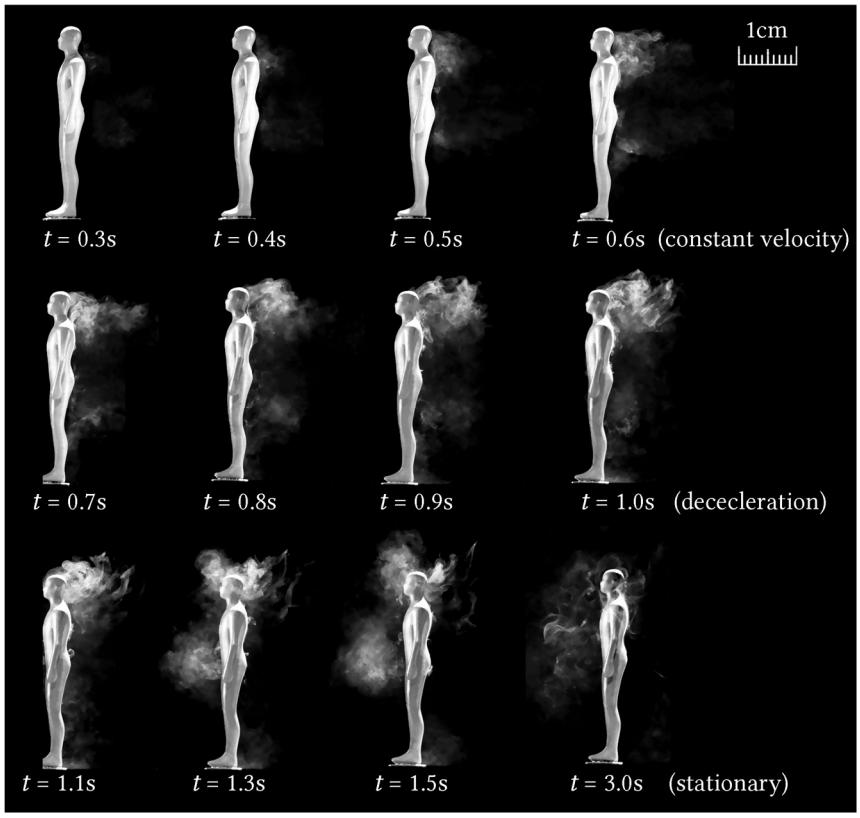

Figure 7.5 smoke generated at (ii) the backline during maximum speed (0.3s to 0.6s); deceleration (0.7s to 1.0s) and stopped (1.1s to 3.0s) for the slim body.

When the manikin came to a complete stop, the smoke generated at the back passed overtook the body. The existence of the back to the shed airflow, part of the smoke swirled upwards and forwards through the gap between the arms and the torso. Although the chemicals originated from the back, the smoke ended up wrapping the face after the manikin stopped moving. This indicates increased exposure risk to contaminants especially when a walking person comes to a stop.

Figure 7.6 shows smoke generated from the backline for the larger body. Similar wake flow patterns to the slim body were observed during constant velocity and deceleration except that the larger body had more smoke shed towards the ground. This was consistent with the observation in Figure 7.4 that a larger body with a lower aspect ratio produced a weaker upwash flow close to the ground thus more smoke remained close to the ground.

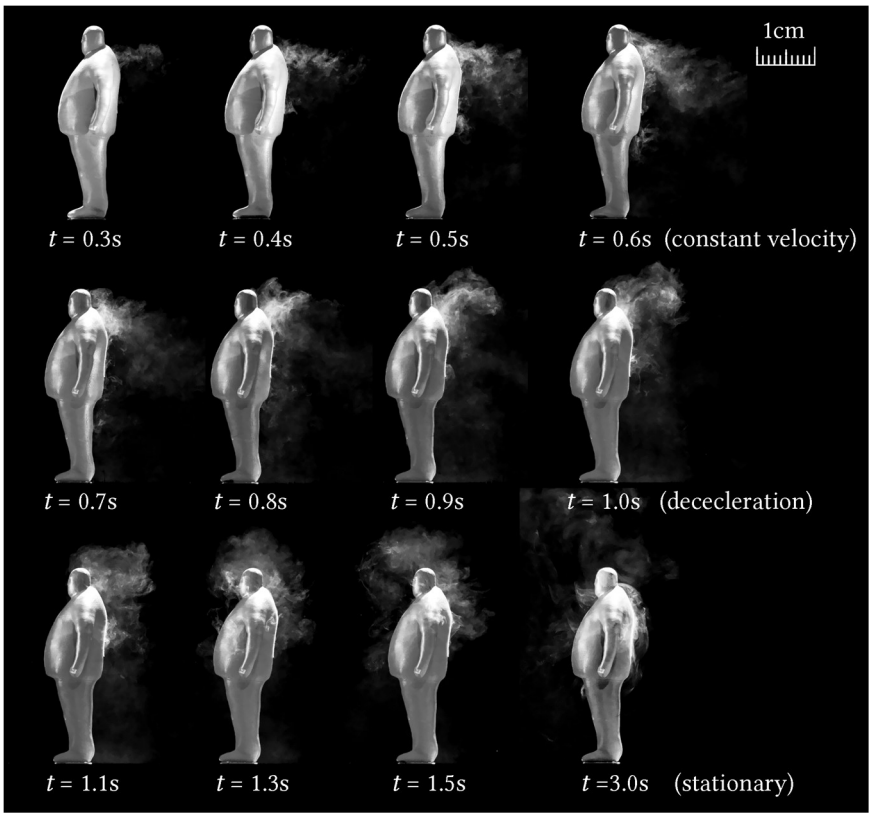

Figure 7.6 Smoke generated at (ii) the backline during maximum speed (0.3s to 0.6s); deceleration (0.7s to 1.0s) and stopped (1.1s to 3.0s) for the larger body.

When the larger manikin stopped moving, the residual smoke moved higher in front of the body compared to that of the slim model (Figure 7.5). Comparing the images at t = 1.3s and t = 1.5s, the slim body had equal portion of smoke surrounding the front of the torso and head, whereas the larger body had most of the smoke surrounding the head. This was attributed to the larger torso that blocked flow passage restricting the smoke to ascend. It appears that during the stationary phase the larger body encountered a more severe level of exposure. The smoke surrounds the head and disappears over time (until t = 3.0s).

7.3.4 **Differences Between the Standing and Walking Poses**

Smoke generated from the hand was similar for both the standing and walking manikins (before t = 0.6s). During deceleration and stationary periods, differences behind the arm were evident where the angled arm of walking model (#2) produced wake flow that ascended more towards chest height

At the lower body, the wake generated at the feet of the standing manikin (#1) fluctuated near the ground. While in the walking posture (#2), the left leg with heel raised had air flowing upwards (Figure 7.7). The observation showed that if the arm was swinging, it was likely to bring more smoke to the chest after coming to a stop compared with a fixed straight arm. When the heel was close to the ground (standing or swinging leg), flow disturbances stayed low to the ground; while when the heel was lifted, i.e. the gap between the foot and the ground was greater, the disturbed air followed the heels and brought the smoke upwards. During the deceleration, the uplifted heel rolled more smoke into the calf (back of shins). The different stance in models suggests that the inclusion of kinematic motion of swinging legs would increase particle suspension from the ground due to the stronger upwash flow.

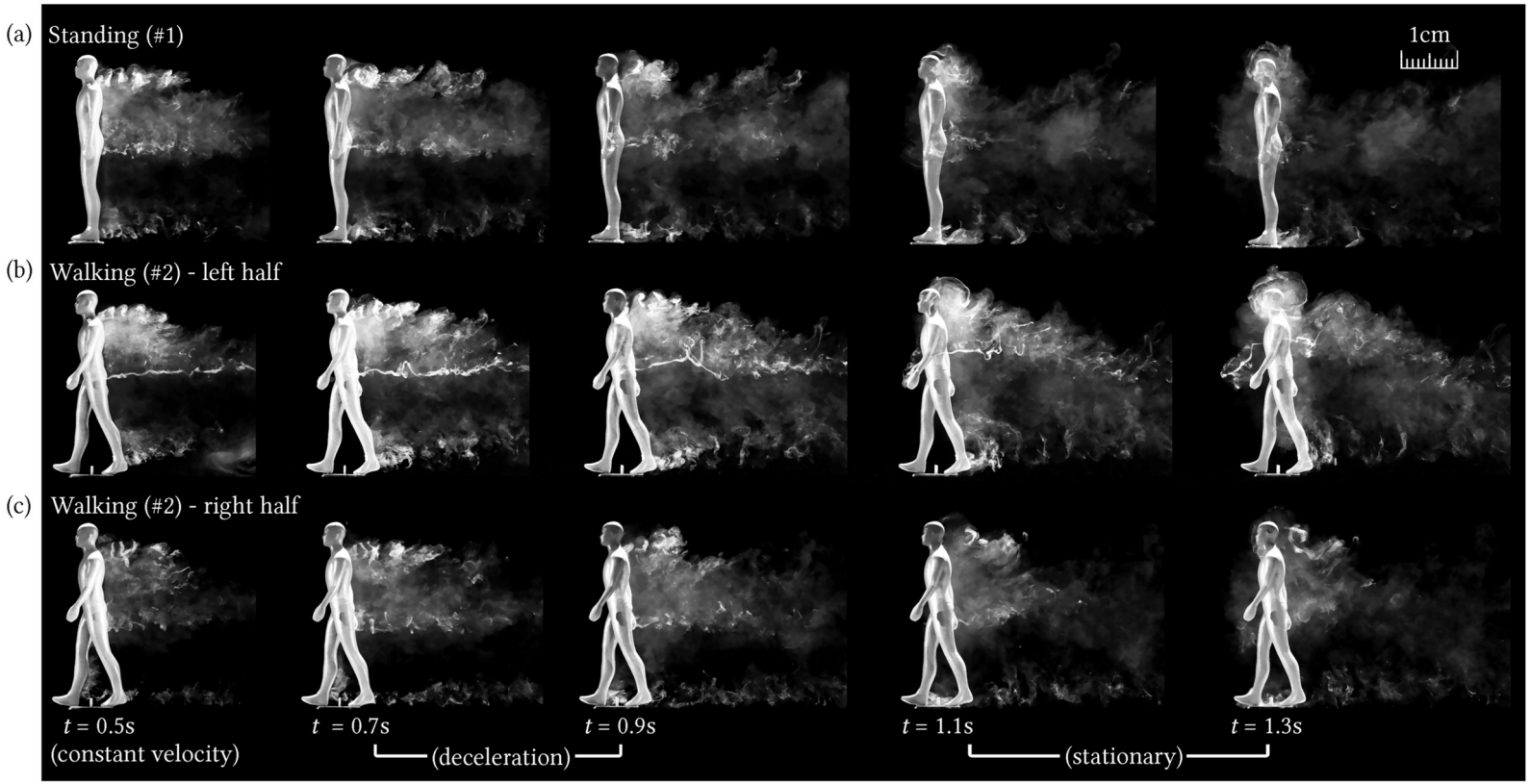

Figure 7.7 Smoke generated from the (a) standing (b) walking left half (c) walking right half body during peak velocity (0.5s),

7.3.5 Quantitative analysis – Vortex Shedding Frequency

Figure 7.8 vortex shedding at the shoulder of (a) a slim body; (b) a larger body

Distinct vortex shedding was captured coming off the left shoulder and formed rolling clockwise rotations (Figure 7.8). Downstream of the body, the vortices rotated downwards and became entrained in the near wake region of the moving body. The vortex shedding frequency was computed by observing the number of vortices passing through a certain position (relative to the body) over a given amount of time. As the wake developed gradually in the early moments of its motion, the duration between t = 0.3s to 0.6s was chosen to sample the vortex shedding.

The vortex shedding interval from the shoulder was approximately 0.039s for the slim body (#1) and 0.035s for the larger body (#3), corresponding to frequencies of vortex shedding from the shoulder at 25.5 Hz and 28.9 Hz respectively, and the vortex shedding interval from the ankle was approximately 0.023s for the slim body (#1) and 0.027s for the larger body (#3), corresponding to frequencies of vortex shedding from the ankle at 43.5 Hz and 37.0 Hz respectively (Table 7.2). For geometries with regular shapes, a characteristic length can be defined to determine the Strouhal number (St). However, for anthropomorphic manikins the characteristic length is not well defined, and

therefore the frequency is only given. With the counted shedding frequency, a suitable time-step size can be defined to resolve the vortex shedding in computational studies, and we suggest $\Delta t = 0.001$s, which was approximately 1/20th to 1/40th of the shedding period observed from the smoke visualisation. This time-step size was deemed small and efficient enough to capture the vortex shedding caused by a moving manikin in this scaled model.

Slim Body				Larger Body			
Time [s]	Shedding Intervals [s]	Interval Average [s]	f [Hz]	Time [s]	Shedding Intervals [s]	Interval Average [s]	f [Hz]
Left shoulder							
0.339				0.368			
	0.0370				0.0350		
0.376				0.403			
	0.0410				0.0330		
0.417				0.436			
	0.0410	0.039	25.5		0.0350	0.035	28.9
0.458				0.471			
	0.0390				0.0360		
0.497				0.507			
	0.0380				0.0340		
0.535				0.541			
Left ankle							
0.445				0.445			
	0.022				0.027		
0.467				0.472			
	0.024				0.030		
0.491				0.502			
	0.024	0.023	43.5		0.028	0.027	37.0
0.515				0.530			
	0.022				0.028		
0.537				0.558			
	0.023				0.022		
0.560				0.580			

Table 7.2 Summary of vortex shedding rate for the slim body and the larger body

7.4 Separation Angle from the Head

We applied an image-processing algorithm in MATLAB based on (Inthavong et al., 2012, Fung et al., 2013) using threshold segmentation on each image (pixel size: 1280×704) to identify the separation angle across the top of the head. Figure 7.9a shows an example, taken at time $t = 0.5$s. The head was partially segmented (using an image mask) out of each image to provide a clear

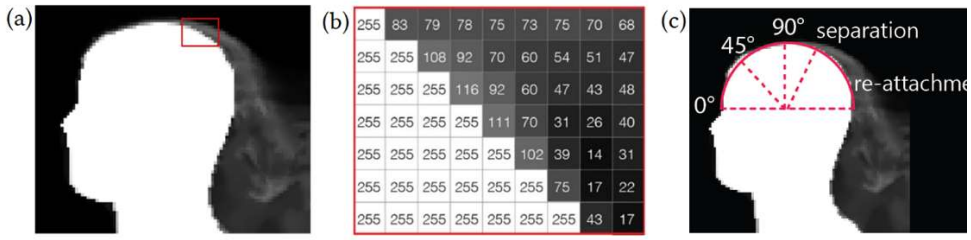

Figure 7.9 Image processing steps for determining the separation angle point along the head. The pixel values in panel (b) are greyscale values where 255 = white and 0 = black

boundary around the head shown in panel Figure 7.9a. The algorithm searches along the edge boundary to detect pixel greyscale values. Separation was determined if within three horizontal pixels to an edge pixel (greyscale = 255) there was a greyscale value of less than 80 (Figure 7.9b). A virtual semi-circle was fitted around the top half of the head at eye-level so that an angle from the front of the head could be calculated (Figure 7.9c). A separation angle was calculated for each image and averaged out over 50-images.

The separation angle profile over time is shown in Figure 7.10. During the peak velocity (t = 0.0s to 0.60s), the separation angle was approximately to 110° for the slim body and the larger body (Figure 7.10a and b). At moderate Reynolds numbers, the separation angle of flow over spheres were between 80˚ to 90˚(Rodriguez et al., 2011). However, the head of the manikins was not a smooth spherical shape; instead it had nose, eye indents and was slightly narrowed at the side forehead area. The less smooth surface and unsymmetrical shape might lead to a delayed separation angle different from that of a sphere. During the deceleration (t = 0.60s to 1.1s), the separation point moved towards the front of the head and significantly earlier than 90°. The flow switches directions from the relative oncoming flow caused by the moving manikin to a reversed flow due to the trailing wake moving into the back of the head. Before a complete stop, the separation angle dropped to an average of 70°.

After the manikin came to a complete stop, the separation angles were not captured as the images showed that the smoke turned into a plume and concentrated around the top of the head and rising. There is no clear stagnation point or developing boundary layer at either side of the vertical smoke plume, and therefore, the separation angle was not applicable.

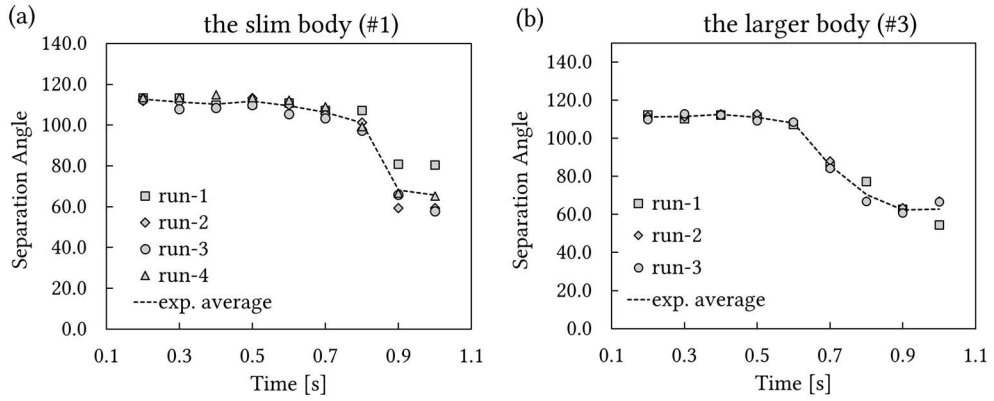

Figure 7.10 Flow separation angle profile across the top of the head for (a) the slim body and (b) the larger body

7.5 Conclusion

A smoke visualisation technique was presented for visualising a moving object through a stagnant environment. With high speed camera and image processing techniques to capture the generated smoke tracing the moving object, qualitative insight into the wake formation and its transformation during the manikin motion were presented. The key points are summarised as follows:

- A larger body shape generated weaker upwash flow located downstream of the body and near the ground. This was due to the body's smaller aspect ratio compared to a slim body. If the smoke is considered as contaminants originating from the body, there would be less contaminants following the larger body as a larger amount remained close to the ground behind the body.
- A walking manikin pose influenced the vortex shedding. Uplifted heels induced upwash flow behind the feet and ascended the residual wake after the manikin came to a stop. The result suggests a swinging arm

and leg motion would cause greater upwash flow at the feet and hand compared to a commonly adopted rigid body model.

- The wake flow that formed behind the manikin continued to travel under its own momentum and pass the manikin when it had stopped moving. The smoke moved upwards and surrounded the head, regardless of where the smoke was generated, e.g. from the head, shoulder or the back of the body. This suggests enhanced exposure to contaminants since more airflow is moving into the inhalation zone when manikin came to a stop.
- During the motion, quantitative data was analysed such as the separation angle from the manikin head, and vortex shedding frequency which can be used as validation of computational modelling.

In the experiments, manikins came out from the holding chamber and entered the main chamber through a sliding door. Flow entrainment effects from opening the sliding door on the manikin flow field were minimal. We found that the manikin moving at 0.95 m/s dominated any residual flow entrainment from the sliding door. Furthermore, smoke visualisation did not occur until further downstream away from the sliding door due to the manikin speed, and the results shown in this chapter started from t = 0.3s, which would fully exclude the potential impact of the operation of the sliding door.

The smoke visualisation was designed to create a new technique that can supplement hot-wire and PIV measurements. It is most suited for small-scale studies for visualising the flow structures when an object itself moves through still air. To observe the flow effects from specific isolated points and visualise the subsequent mixing that occurs in its wake. However, the thermal condition of the human body was not considered in the experimental setup, thus the airflow pattern observed in the smoke visualisation did not reflect the realistic interaction between the human thermal plume and the human wake flow. Another major limitation is achieving dynamic similarity between large-scale models and the actual experiment used. Our results were $1/5^{th}$ scaled in dimensions but maintained the highest walking speed of 0.95 m/s; thus, the Reynolds number matching was $1/5^{th}$ of the dynamic similarity. In the near future, a larger scale model will be used to achieve larger Reynolds numbers.

Chapter 8
CFD Modelling of Three Moving Manikin Models

The main findings of this chapter have been published in:

- **Tao, Y.,** Inthavong, K., Petersen, P., Mohanarangam, K., Yang, W., Tu, J. Y. (2018). Vortex structures, and wake flow analysis from moving manikin models. *Building Simulation*, submitted.

- **Tao, Y.,** Inthavong, K., Petersen, P., Mohanarangam, K., Yang, W., Tu, J. Y. (2018). Numerical Simulation and experimental validation of wake flows induced by moving manikins. COBEE2018 – the 4th international Conference on Building Energy & Environment, 5-9 Feb, Melbourne, Australia

Vortex shedding in the wake flow generated by moving bodies influence pollutant dispersion in indoor environments. In this study, three scaled models $1/5^{th}$ of realistic size were used, including two body shapes (thin and wide) and two body poses (standing and walking). The airflow from moving bodies was simulated using computational fluid dynamics (CFD) with dynamic meshing to account for the manikin movement. Experimental data from a smoke visualisation technique was used to provide validation data for computational simulations. Flow separation angle over the head was computed through image processing, which found separation points shifting from the back of the head to the front as the velocity decreased. The vortex structures were visualised using an omega vortex identification method and was compared with experimental visualisations. The location and main patterns of the vortex structures matched with the smoke visualisation, which can help identify the transport of pollutants from and around the body during walking and coming to a stop. Results showed that larger bodied manikins had a longer time of airflow surrounding the breathing region after the motion came to a stop, and thinner

bodied manikins have reduced time of exposure to airborne contaminants after re-dispersion caused by the motion.

8.1 Introduction

Flow induced by moving human bodies experiences boundary layer separation, producing vortex shedding in the wake region. The regular vortex patterns in the wake redistribute airborne pollutants in many indoor environments such as manufacturing, hospital wards, clean rooms and airline cabins raising respiratory health concerns of occupant exposure (Anthony and Flynn, 2006, Inthavong et al., 2009, Inthavong et al., 2013b, Ferro et al., 2004, Tao et al., 2016, Gao et al., 2012).

Vortex shedding in the wake has shown to influence pollutant dispersion and caused complex behaviour due to advection and turbulent diffusion (Tominaga and Stathopoulos, 2013). For example, Edge et al. (2005) found increased spreading of pollutants attributed to combined effects of the left-right vortex shedding and the downwash effect from the wake coming from a stationary human body. Khare and Marr (2014) demonstrated particle re-suspension/dispersion occurring from the floor induced by the wake produced during human walking. Similar fluid-particle behaviour of airflow over bluff bodies were found in street canyons where wind moving over a building generated a trailing vortex, and pollutant dispersion was perturbed by the vortices in the wake flow of the buildings (Park et al., 2015, Tsai and Chen, 2004). These studies suggest unsteady vortices in the wake region over bluff bodies are a key factor in influencing pollutant transport.

To address the influence of vortices produced by human activity, experimental and Computational Fluid Dynamics (CFD) studies have investigated the fluid dynamics of human wake flow and its impact on the transport of indoor pollutants. Early experimental studies (Kulmala et al., 1996b, Kim and Flynn, 1991) used a manikin installed in an open-ended wind tunnel, and tracer gases were released from different locations to visualise the boundary layer separation, and the size and location of the wake region. CFD studies (Edge et al., 2005, Murakami et al., 1999, Hayashi et al., 2002, Ge et al., 2013, Se et al., 2010) explored the unsteady wake regions from a human body and the subsequent transport of pollutants. However, many earlier experimental and CFD studies

used stationary human models which ignores flow separation at the feet and neglects flow unsteadiness caused by the manikin motion. This leads to the near wake flow characteristics during walking being only partially represented. Furthermore, simplified geometries such as vertical finite cylinders and cuboids have been used as substitutes for human bodies (Poussou et al., 2010, Thatcher et al., 2004), and this also leads to discrepancies between realistic and cylindrical geometries (Edge et al., 2005, Tao et al., 2017a, Tao et al., 2017b).

Consequently, in recent years a growing number of experimental and computational studies have focused on the effects of human activity on the wake dynamics. Han et al. (2014) used a full-scale thermal manikin and measured the dynamic airflow with hot-wire anemometers. They noted the limitation of the method was that measurements were taken at a point (from the probe sensor) and thus unable to obtain comprehensive information of the whole flow field. Poussou et al. (2010) conducted small-scale Particle Image Velocimetry (PIV) and Planar Laser Induced Fluorescence (PLIF) measurements to qualitatively capture the wake flow from a moving block and pollutant transport inside an airline cabin. Saarinen et al. (2018) conducted a Large-Eddy Simulation as well as a smoke visualisation of contaminant transport between hospital isolation rooms, and offered qualitative comparisons of vortex shedding induced by occupant motion and operation of doors. Luo et al. (2017) conducted PIV measurements on a small-scale cabin with a moving manikin, and observed flow patterns such as symmetric eddies, an upward vortex and a strong downwash in the wake flow along the vertical centre plane. Computational studies also observed similar wake flow patterns and vortices in the wake region causing significant dispersion of pollutants (Brohus et al., 2006, Oberoi et al., 2010, Tao et al., 2017a), particularly some achieved the realistic motion with swinging limbs (Choi and Edwards, 2012, Choi and Edwards, 2008, Hang et al., 2014, Tao et al., 2017a).

To visualise the vortex structures inside the wake, the vorticity parameter, using the q-criterion or λ_2 methods, has been widely used to depict the vortex dynamics or to identify vortex cores in the wake region (Edge et al., 2005, Choi and Edwards, 2012, Poussou and Plesniak, 2012). However, this method can be difficult to accurately distinguish the actual rotational motion of the vortex (Kolář, 2007). The selection of the vorticity value in either the q-criterion or λ_2

methods for vortex identification lacks a clear physical meaning. Additionally, inappropriate values can lead to strong vortices being captured while weak ones are skipped. Moin and Kim (2006) suggest that it is only suitable for vortex visualisation, and that it cannot identify the accurate positions and regions of the vortices. In this paper we use an omega vortex identification method proposed by Liu et al. (2016) which is based on a physical meaning of its omega criterion.

To validate the computational results of flow separation and visualisation of the wake, a smoke flow visualisation technique (Inthavong et al., 2017) was performed on a dynamic model to provide qualitative understanding of the gross flow field. Recent studies have demonstrated the ability of smoke visualisation to capture separation points, reattachment points, and vortex shedding phenomena (Sohankar et al., 2015). Moreover, with high speed photography and image processing, quantitative data was extracted for validating CFD simulation data of moving human subjects/manikins.

The objective of this study was to present a computational investigation of the wake flow induced by a moving human manikin. Computational modelling using the dynamic mesh method was performed to simulate the fluid dynamics of moving manikins through an indoor space. To identify how the wake flow from moving manikins affected pollutant transport in the near body region, a vortex identification method was used to visualise the vortex structure generated by the moving body. Experimental visualisation data from Chapter 7 (published in (Tao et al., 2018)) was used to validate the computational modelling method through qualitative and quantitative.

8.2 Method

8.2.1 Computational Models

The computational domain replicated the smoke visualisation experiments published in Tao et al. (2018). The experiment used a $1/5^{th}$ scaled model in an indoor room with dimensions of 0.8m (x-coordinate) × 1.1m (y-coordinate) × 0.6m (z-coordinate), and three manikins (a slim manikin in standing pose, model #1, the same slim manikin in walking pose, model #2 and a larger bodied manikin in standing gesture, model #3) were mounted onto a rack-and-pinion

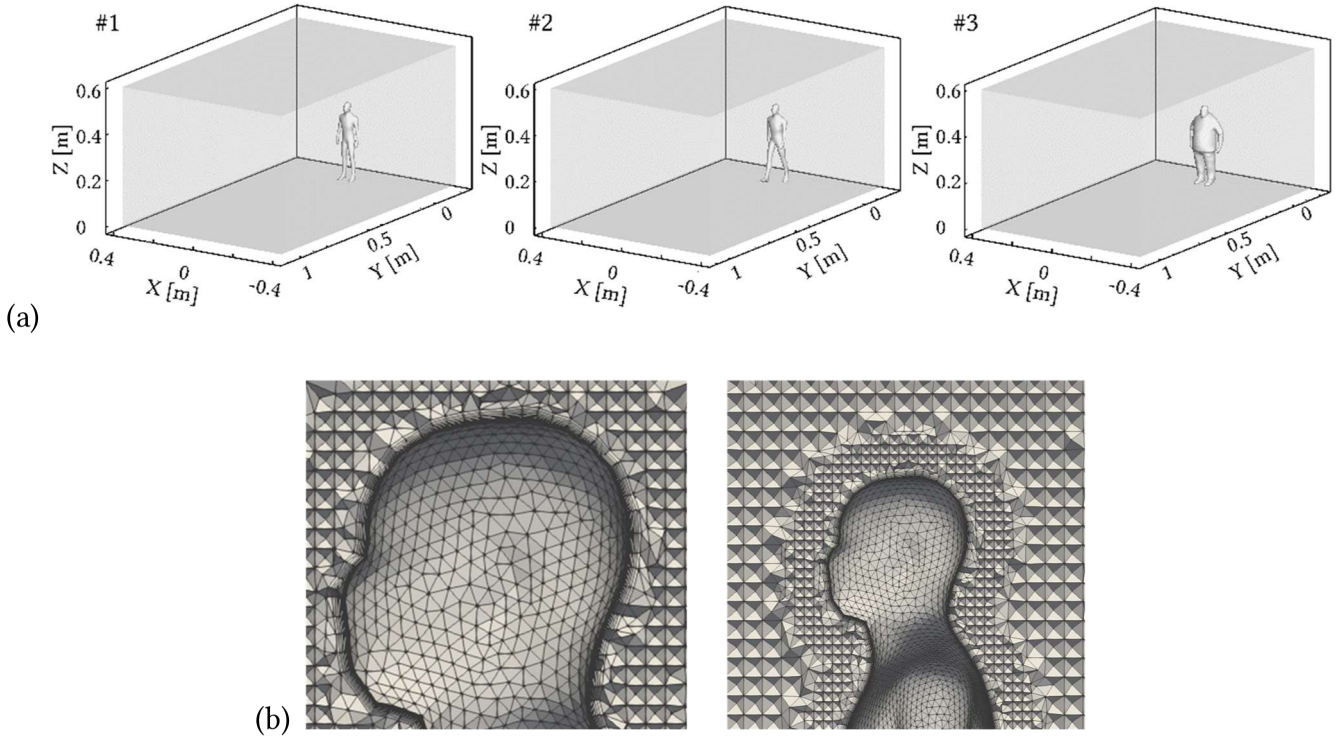

Figure 8.1 CFD models of (a) the computational domain of three manikins (#1, #2, #3); (b) the mesh setup of manikin #1 – slim standing body.

door and across the floor of the test chamber. Smoke was visualised from light reflecting off the opaque amine salts that were formed as the by-product of the chemical reaction between the cyclohexylamine and acetic acid. The settling velocity of the amine salt particles is extremely low and therefore are ideal as a tracer gas.

The computational domain had the same dimensions of 0.8m (x-coordinate) × 1.3m (y-coordinate) × 0.6m (z-coordinate) except with an extra 0.2m extension in the y-coordinate to allow a structured grid between the manikin and the rear wall during the dynamic meshing (Figure 8.1). The manikins were centred laterally in the domain and offset inside the y-coordinate by 0.2m and moved with the same velocity profile as the experiment tests. The mesh of the computational domain was generated using the software ANSYS ICEM. The manikin surface was created with unstructured tetrahedral cells and 10 prism layer cells with a grid spacing of 1×10^{-4}m with $y+ < 5$ (for boundary layer separation), while the external room contained structured hexahedral cells (Figure 8.1b). For the dynamic meshing the domain used layering mesh method at each time step updating the moving manikin position.

A grid independence study was conducted by consecutively reducing individual cell spacing by a factor of 1.3. We started with a grid of 1.1 million and subsequent grids of 2.0 million, 4.3 million, and 8.3 million were created. Velocity profiles along a horizontal and vertical line behind the manikin showed convergence between mesh size 4.3 million and 8.3 million. For computational efficiency and accuracy, the 4.3-million model was chosen for the remainder of this chapter.

Detailed dimensions of the two body types (slim and large bodies) are given in Figure 7.1. The aspect ratio (defined as the ratio of the body height to the body width) is 3.1 for the slim body and 2.1 for the wide body. These dimensions quantify the shape and size of the body which influences flow dynamics and provides analysis for local Reynolds numbers and describing separation points.

8.2.2 **Velocity Profiles**

The distance travelled by the manikin as a function of time was averaged over multiple runs from the experiment (Tao et al., 2018) and is shown in Figure

7.2a. The manikin started from rest inside the holding chamber and accelerated to 0.95m/s. Several points were chosen to represent the velocity profile of the manikin in the CFD simulations (CFD sample points in Figure 7.2b).

8.2.3 **Fluid Modelling**

Numerical simulations were carried out using the commercial CFD software ANSYS Fluent. The manikin motion was achieved by the layering dynamic mesh method, by using which the grids split or collapse at the wall boundaries in this case. For a general scalar ϕ on an arbitrary control volume $\boldsymbol{V}$ with a moving boundary, the integral form of the conservation equation is given as:

$$\frac{\partial}{\partial t}\int_V \rho\phi dV + \int_{\partial V} \rho\phi(\vec{u} - \vec{u}_g)\cdot d\boldsymbol{A} = \int_{\partial V} \Gamma\nabla\phi \cdot d\boldsymbol{A} + \int_V S_\phi dV \qquad (7.1)$$

where, ϕ represents a scalar, ρ is the fluid density, $\vec{u}$ is the flow velocity vector; $\vec{u}_g$ is the grid velocity of the moving mesh, $\boldsymbol{A}$ is the boundary of the control volume V, Γ is the diffusion coefficient, S_ϕ is the source term.

The realistic manikin exhibited an irregular shape, and flow separation across different sections of the body can be considered locally. If we consider horizontal separation at the waist (hydraulic diameter D_h = 0.047 m), and head (D_h = 0.029 m) for the slim body, then the resulting Reynolds number at peak velocity of 0.95m/s are 3206, and 1972. External flow over cylinders exhibit turbulence for Re > 20,000 suggesting that a laminar flow model could be feasible for capturing the flow separation from the moving manikin. However, the motion-induced wake by the anthropomorphic geometry might exhibit more complex airflow behaviours. Thus, the RNG k-ε turbulence model was also employed to give comparisons, based on cases related to human activities in indoor environments (Poussou et al., 2010, Wu and Gao, 2014, Hang et al., 2014, Mazumdar et al., 2011). Prism layers were created on the manikin model producing $y+$ < 5, and the enhanced wall function was used for the near-wall treatment.

To solve the equations, the SIMPLE algorithm was adopted to couple the pressure and velocity field in the RANS equations. Second-order discretization scheme was employed to solve convection and diffusion terms for flow variables. A transient flow simulation was performed with a time step size of Δt =

Thermal manikin conditions were not considered, according to the findings from Wu and Gao (2014), Oh and Kato (2018) that when an on-coming wind begins to appear at 0.2 m/s, the wind penetrates the thermal boundary layer leading to collapse of the rising plume. When the freestream velocity becomes larger than 0.4 m/s for a 1:1 scaled human body, the wake flow dominates the thermal plume and the micro airflow/environment near the body. Visualisation and comparisons of airflow interaction between the wake and thermal plume confirm the dominant effect of the freestream velocity during walking motion (Tao et al., 2017b).

An increase of wind velocity or walking speed increases heat transfer rates, and possibly thermal comfort, while the thermal plume effect on the freestream flow will be less effective. As the focus of this study was mainly on the wake structure, and that the velocities are greater than 0.2m/s, we used iso-thermal conditions of the manikins as a reasonable simplification for our experiments and CFD simulations.

8.2.4 **Vortex Identification Method**

The omega vortex identification method proposed by Liu et al. (2016) was applied to capture the vortex structures from the numerical simulations. Compared to the λ_2 and Q-criterion methods, the new omega vortex identification method proposed a physical representation of Ω where a vortex is formed when the vorticity is strong and deformation is weak. The Ω vortex identification method is derived by splitting the vorticity into a vortical and non-vortical component as:

$$\nabla V = A + B = \frac{1}{2}(\nabla V + \nabla V^T) + \frac{1}{2}(\nabla V - \nabla V^T) \tag{7.2}$$

where ∇V is velocity gradient tensor, A is the strain rate tensor/deformation and B is the rotation rate tensor/whole vorticity. The square of Frobenius norm of A and B is then introduced as:

$$a = trace\,(A^T A) = \sum_{i=1}^{3}\sum_{j=1}^{3}\left(A_{i,j}\right)^2 \tag{7.3}$$

$$b = trace\,(B^T B) = \sum_{i=1}^{3}\sum_{j=1}^{3}\left(B_{i,j}\right)^2 \tag{7.4}$$

The ratio Ω is defined as:

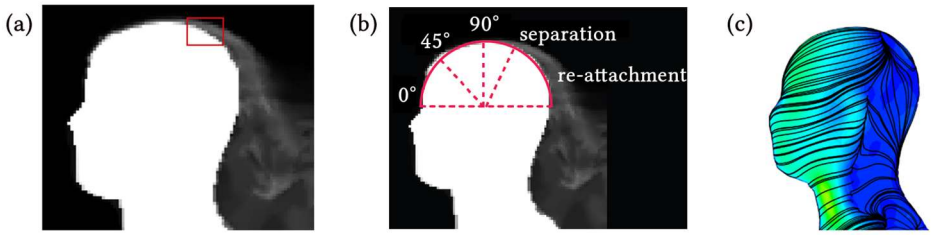

Figure 8.2 The head with a white image mask; (b) the angle started from the forehead (Tao et al., 2018) and (c) the surface streamlines on the head in the CFD simulation shows the location of separation.

$$\Omega = \frac{b}{a+b} \tag{7.5}$$

According to Liu et al. (2016)'s study, the physical meaning of Ω is its representation of when the vorticity overtakes its deformation, thus a value of Ω=0.52 was found to properly defined the vortex, although a small change of Ω to 0.51 or 0.53 might also be appropriate. This value was demonstrated on boundary layer transition and a micro-vortex generator. Within this small range, the identified vortical structures are insensitive to the change in Ω, although some minor structures vanish as Ω increases beyond the range. In this chapter the Ω value from 0.5 to 0.8 were tested and the value of Ω = 0.52 was confirmed appropriate to represent the vortex structures in our cases.

8.3 Results

8.3.1 Validation - Separation Angle from the Head

Flow separation off the head was analysed in (Tao et al., 2018) through an image-processing algorithm in Matlab using threshold segmentation (Inthavong et al., 2012, Fung et al., 2013) to identify the separation angle across the top of the head (Figure 8.2). A semi-circle was fitted around the top half of the head at eye-level so that an angle from the front of the head could be calculated (Figure 8.2b). The separation points from CFD simulation results were

found at the lowest shear stress value at the same location – the centreline of the head surface. Visualisation of surface streamlines also confirmed the location of separation points.

The separation angle profile obtained from the smoke visualisation and CFD simulations over time is shown in Figure 8.3. During constant velocity (t = 0.0s to 0.6s), the separation angle from the smoke visualisation was approximately 110° for both the slim body and larger body (Figure 8.3a and b). During deceleration (t = 0.60s to 1.1s), the separation point moved forwards to the front of the head and significantly earlier than 90°. As the manikin motion decelerated, the flow switched directions from oncoming to a reversed flow, and the trailing wake moved into the back of the head. Before a complete stop, the separation angle moved to 70°. After the manikin came to a stop, the separation angles were not captured as the images showed that the smoke turned into a plume and concentrated around the top of the head and rising. No clear stagnation point or developing boundary layer at either side of the smoke plume was found and therefore, the separation angle was not applicable.

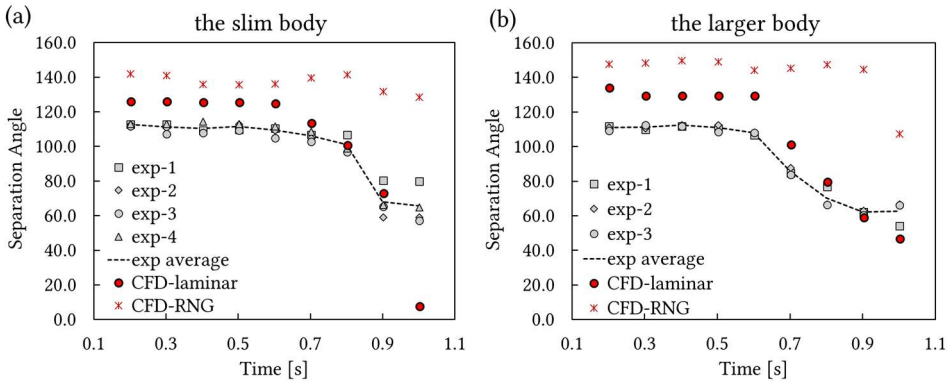

Figure 8.3 (a) Flow separation angle profile across the top of the head of (a) the slim body (experimental test ran for 4 times) and (b) the larger body (experimental tests ran for 3 times).

The angle predicted by the laminar CFD simulation produced a similar trend with the experimental result. During the constant peak velocity, the CFD predicted an average separation angle of 130° for both slim body and larger body. When the deceleration started (from t = 0.6s), the separation moved earlier and the angle was 60° ~ 70° at t = 0.9s. The error between the laminar simulation results and experimental results were up to 18%. When using the RNG k-ε

turbulence model, the predicted separation angle deviated more from the experimental results, especially when the manikin stopped moving. This may be due to excessive variation of dissipation from the walls that led to the inaccurate prediction of the development of turbulence. Therefore, the results from simulations using the laminar model are analysed in the following sections.

The agreement in separation angle trending profile from the head between the smoke visualisation and the laminar CFD simulations showed the computational method used for the models can reflect the flow characteristics caused by separation.

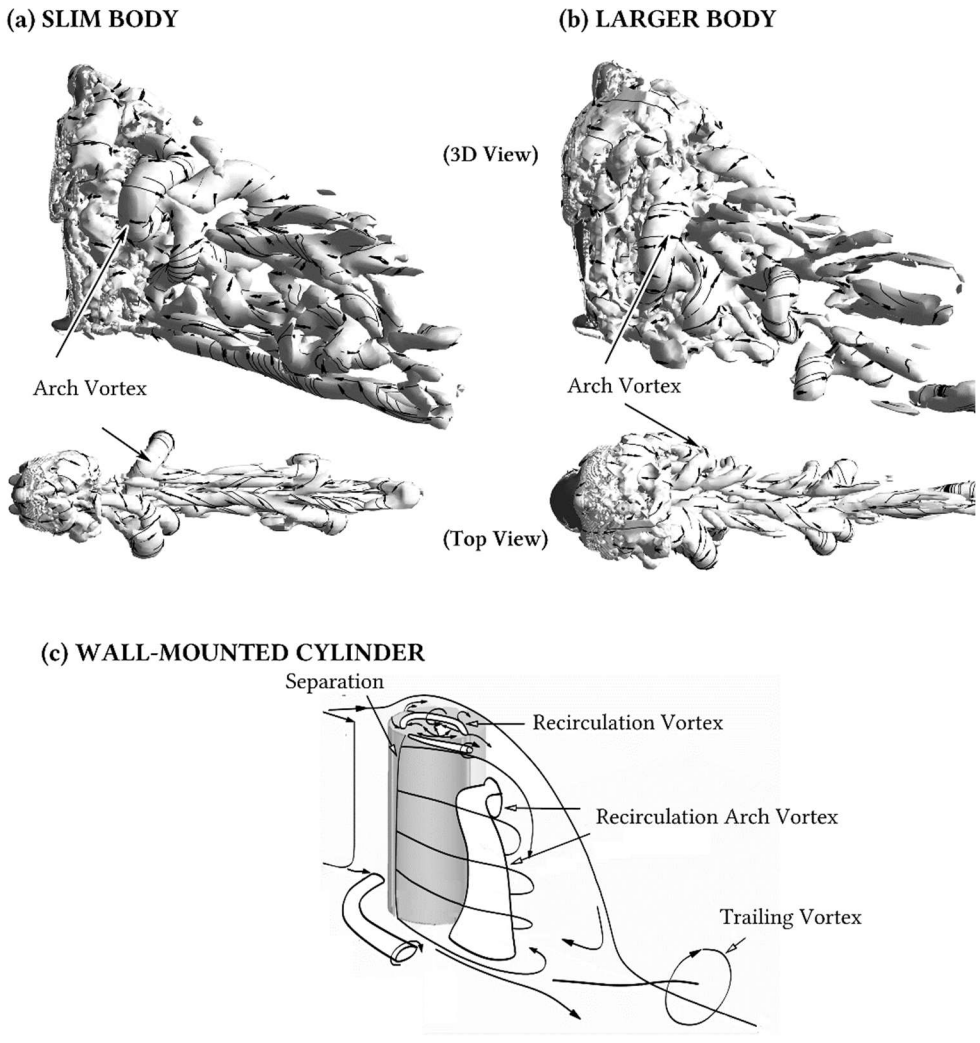

Figure 8.4 Vortex structures featured with streamlines downstream the manikins at t = 0.6s (peak velocity) in three-dimensional view and top view for (a) the slim body, (b) the larger body, and (c) a time-averaged flow topology for flow over a cylinder investigated by (Octavian et al., 2011)

8.3.2 3D View of Vortex Structures

Figure 8.4 shows vortices behind (a) the slim body and (b) the larger body, at t = 0.6s (peak velocity) in a three-dimensional view and a top view, and compared with a time-averaged flow topology (artificial structures) for (c) flow over a cylinder investigated by (Octavian et al., 2011). For a cylinder, characteristic flow features in the wake include boundary layer separation, shear layer instability and the subsequent vortex formation; and these are strongly affected by downwash effects from the flow over the top free end (Octavian et al., 2011).

Comparably, when the manikins moved through a stagnant environment, vortices were formed behind the body, characterised featured by a recirculation vortex on the top of the head, separation from the side of the bodies, and the arch vortex detaching off the moving bodies. The arch vortex behind a slim body is clearly defined with a coherent structure which detached periodically (in Figure 8.4a), whereas the arch vortex behind the larger body (Figure 8.4b) was more immersed within the near wake of the body, which exhibited a larger amount of vortices attaching to the near body region during walking.

8.3.3 Wake Vortex Structures of the Slim Body

Figure 8.5 compared smoke visualisation (Tao et al., 2018) and the three-dimensional iso-surfaces of Ω = 0.52 (coloured by velocity magnitude) in the wake of the moving slim manikin. In the smoke visualisation, the cyclohexylamine was dabbed on locations on the body (the head, the thigh and the knee) thus reflected local wake flow structures, whereas the computational simulation presented all vortex structures generated by the motion.

At the beginning of the motion with constant velocity of 0.95 m/s (t = 0.2s to 0.6s), the separation over the head occurred at the back and vortices formed downstream at shoulder height. Smoke generated from the thigh and knee, formed mixed vortices behind the buttocks and the knees with a distinct shedding pattern. Similar patterns were observed in the computational results, where behind the torso the main structure showed two strong arch vortices forming behind the arms oscillating during the motion. As the manikin moved forward, the arch vortices stretched downstream, detached from the near

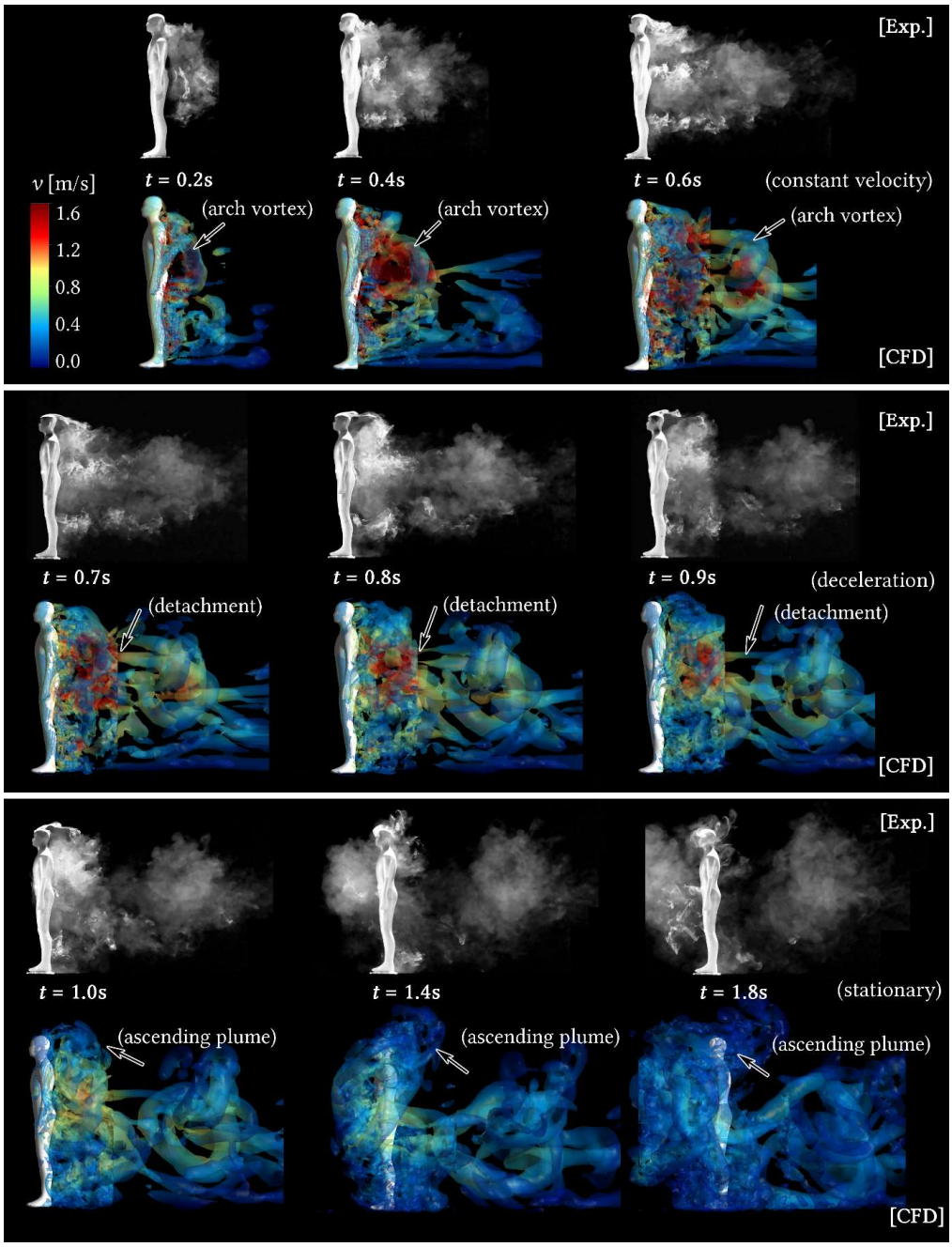

Figure 8.5 Comparisons of vortex structures from smoke visualisation and computational simulations (Ω = 0.52 and coloured by velocity magnitude (v) from t = 0.2s to 0.6s (under constant peak velocity), t = 0.7s to 0.9s (deceleration) and t = 1.0s to 1.8s (stationary)

wake, and new arch vortices formed in its place, while old ones dissipated. Behind the lower body, the vortices were weak and was disturbed by the flow generated from slimmer cylindrical shaped legs.

During deceleration (t = 0.6-1.0s), the reduced momentum resulted in earlier separation from the head, and airflow started to recirculate higher behind the

head. Moreover, a detachment in the wake was observed in both smoke visualisations and simulations. In the smoke visualisations it was shown by the residual smoke detaching from the moving manikin. In the simulation, the large vortex structures detached from the body and there was a gap between the near-body wake and the downstream wake. The change in wake structure reflects the ability to transport pollutants. If pollutants were generated from the body at a constant rate and carried by the motion, smaller arch vortices during deceleration would trap more pollutants around the body and transport less downstream.

After the manikin stopped (t = 1.0–1.8s), a part of the smoke propagated to the front of the body and was pushed upwards over the head and surrounded the head/breathing zone for almost as long as the moving duration. During that time most of the smoke was pushed forward by the momentum in the residual wake and plume which was ascending due to the circulation over the head.

8.3.4 Wake Vortex Structures of the Larger Body

Figure 8.6 shows the wake flow for the larger body where more vortices were found near the ground in the wake region compared to the slim body. For the larger body, arch vortices shifted from the middle of the back to behind the lower body during walking and deceleration (0.2 to 1.0s). The arch vortices behind the body didn't stretch as far as that of the slim body as they shifted downwards and more were interrupted by the vortices from the lower body. There was increased mixing of vortices close to the ground thus the detachment of the wake during the deceleration was less distinct compared to that of the slim body.

When the larger manikin stopped, the residual wake pushed the smoke forward and upwards. Since the vortex shedding with high velocities behind the larger body occurred at a lower height, the residual wake also passed forward almost below the chest. However, from t = 1.4s to 1.8s, the ascending smoke around the head of the larger body kept arising whereas that of the slim body already dissipated at the same time. Although the bulk of vortex shedding behind the larger body distributed at a lower height, the part of residual wake that passed towards the head tend to engulf the breathing zone for a longer time. The vortex structures from CFD matched reasonably well with the

smoke visualisation, which validated the computational method in its ability to capture the location and vortex patterns.

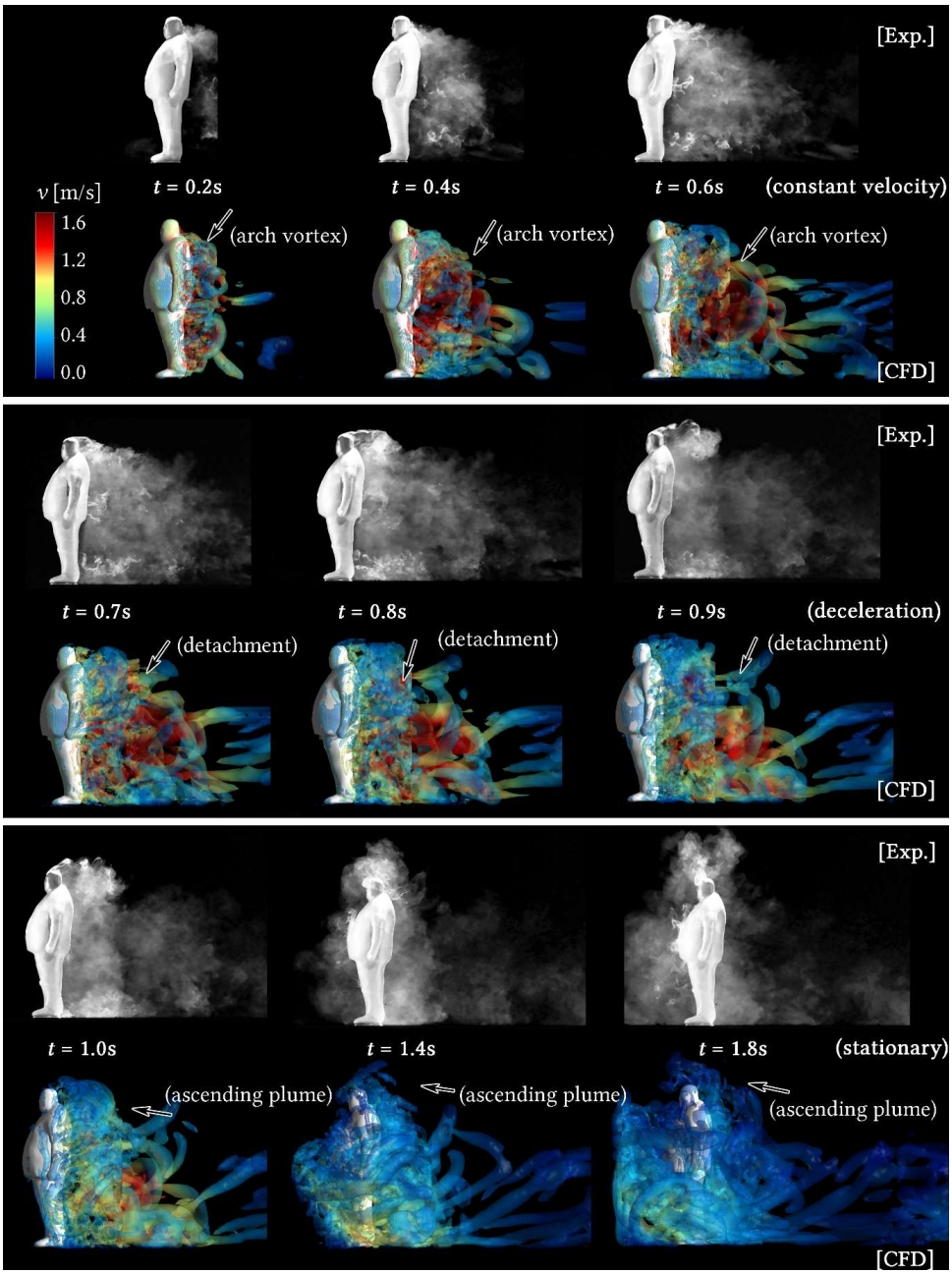

Figure 8.6 Comparisons of vortex structures from smoke visualisation and computational simulations (Ω = 0.52 and coloured by velocity magnitude (v) from t = 0.2s to 0.6s (under constant peak velocity), t = 0.7s to 0.9s (deceleration) and t = 1.0s to 1.8s (stationary)

8.3.5 Transient Flow Behaviour - Slim vs Larger Bodies

Figure 8.7a shows the velocity magnitude contours induced by the slim body and the larger body in the mid-plane. The region of highest velocities differed

between the two bodies due to the different aspect ratio (*h/D*) value. The slim body (*h/D* = 3) had high velocity from the buttock to the shoulder while the larger body (*h/D* = 2) had a larger area of high velocity region from the thigh to the shoulder.

During constant peak velocity (0.2s – 0.6s), the slim body had strong airflow tightly following the body, while the larger body had strong airflow detached a little away from the body and extended further downstream. During deceleration (0.6s – 1.0s), the reduced momentum influenced peak velocities behind the back, but the size of the wake region didn't shrink immediately. Particularly behind the larger body, the high velocity region shifted towards the ground rather than dissipating locally as found for the slim body. From deceleration to stationary, the wake behind the larger manikin dissipated slower than the slim body, and most of the airflow behind the larger body went towar、ds the ground.

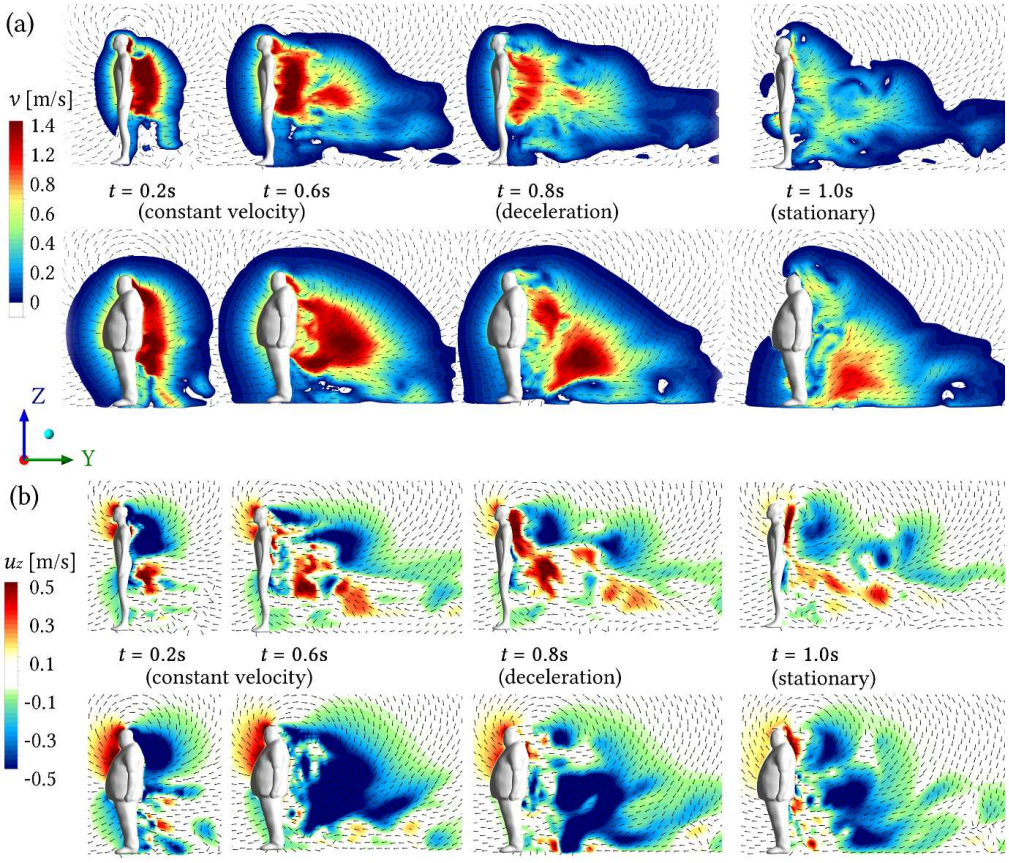

Figure 8.7 (a) Velocity magnitude (v) and vectors at the mid-plane of the slim body and the larger body (b) vertical velocity component (u_z) and vectors on the mid-plane of the slim body and the larger body at t = 0.2s, 0.6s, 0.8s and 1.0s

Comparison of the vertical velocity component u_z in the mid-plane (Figure 8.7b), showed a dominating downward velocity component behind the larger body. For the slim body, the airflow was balanced by downwash from the head and upwash behind the back and from the gap between the legs, whereas the larger body produced a dominant downwash flow over a large region pushing the wake towards the ground.

The velocity magnitude and the vertical velocity (u_z) at t = 0.5s (constant peak velocity) were taken at vertical lines (height from z/h = 0 to 1.6) on the mid-plane behind the body with distances of y/h = 0.01, y/h = 0.3, y/h = 0.6 and y/h =0.9. Comparisons were made between the slim body and the larger body (Figure 8.8). All velocity profiles were similar between the models in the upper body from the head to the waist (z/h = 0.6). Differences were found behind the legs, where high velocity magnitudes ended quickly behind the torso of the slim body due to the counter action from the jet flow between the legs, while behind the larger body high velocities shifted towards the back and the ground due to the stronger vortices behind the larger body.

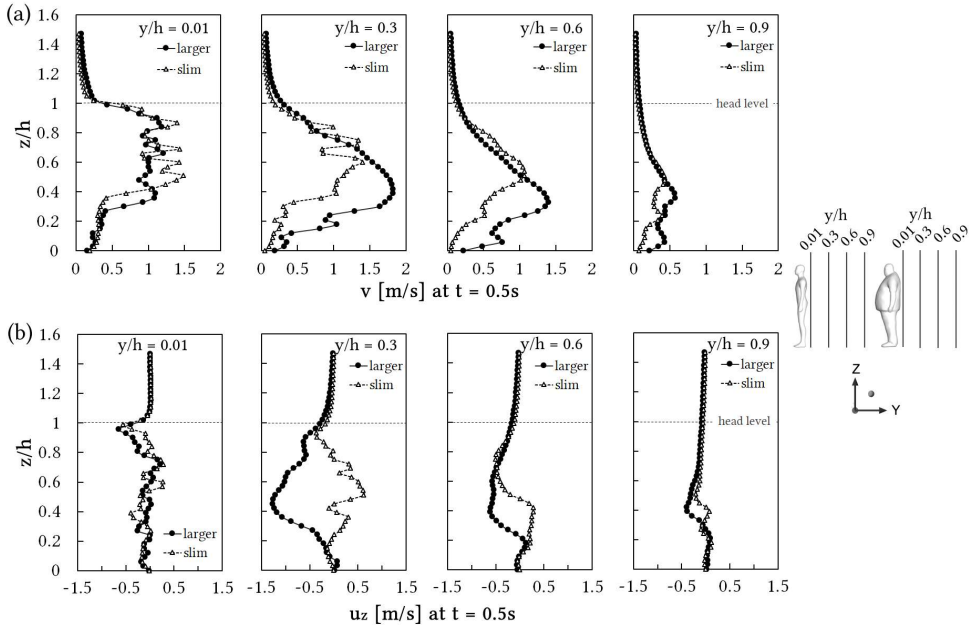

Figure 8.8 The comparisons of (a) velocity magnitude (v) and (b) the vertical velocity component (u_z) between the slim body and the larger body at lines on the mid-plane behind the body with distances of y/h = 0.01, y/h = 0.3, y/h = 0.6 and y/h =0.9 at the peak velocity (t = 0.5s).

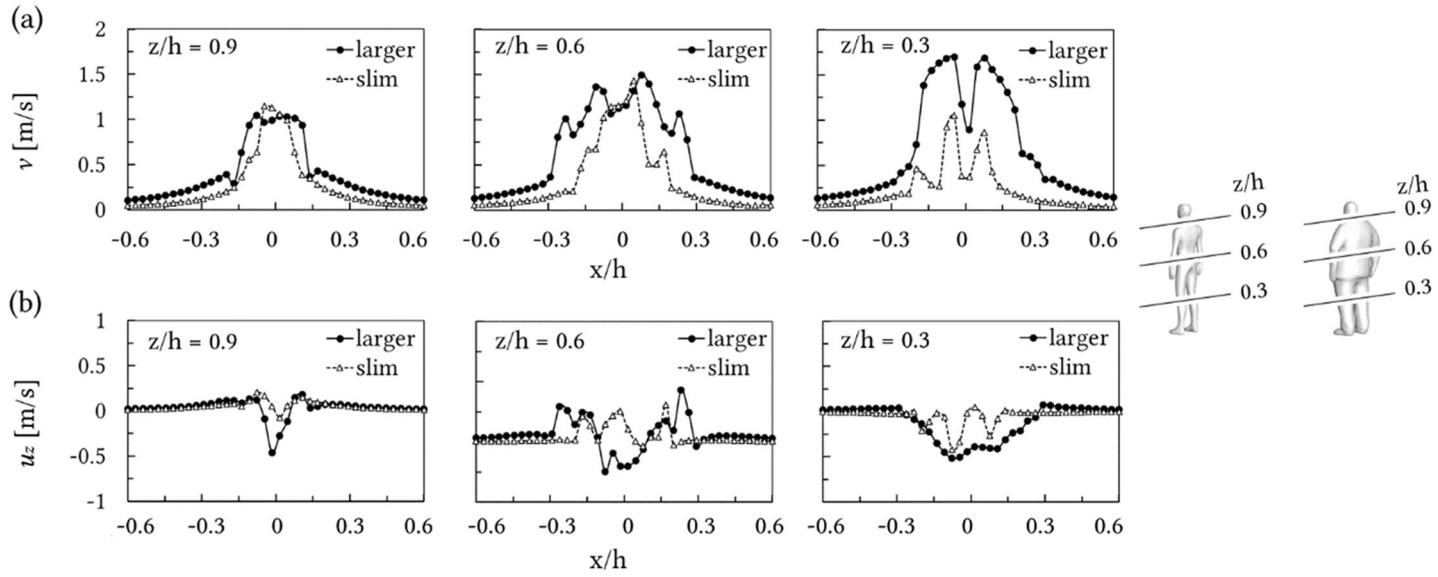

Figure 8.9 The comparisons of (a) velocity magnitude (v) and (b) vertical velocity (u_z) between the slim body and the larger body at horizontal lines y/h = 0.01 behind the body at z/h = 0.9 (head), z/h = 0.6 (waist) and z/h = 0.3 (knees) at the peak velocity (t = 0.5s)

The vertical velocity component u_z close to the bodies (y/h = 0.01) was similarly disturbed. Further downstream (y/h = 0.3, 0.6), the larger body generated negative vertical velocity components (i.e. towards the ground) behind the legs while the slim body generated upward vertical components at the same region. This was also attributed to the gap between the legs, where a counter-rotating flow was generated and dominated for the slim body, while behind the larger body the downwash from the upper body dominated.

Similarly the velocity magnitudes and the vertical velocity (u_z) at t = 0.5s were taken at the horizontal lines (x/h =-0.6 to 0.6) on the vertical plane y/h = 0.01 behind the body at z/h = 0.9 (head), z/h = 0.6 (waist) and z/h = 0.3 (knees) as shown in Figure 8.9. The larger body had a width at the waist (101mm) almost twice as large as that of the slim body (58mm), which caused the large difference in velocity fields behind the body. If we consider the half-velocity widths (region with velocities higher than the ½ maximum velocity along the same line), then the larger body has a region that is almost double that of the slim body, i.e. in the span-wise direction the velocity distribution was proportional to the shape (frontal widths) of the bodies.

When the manikin stopped moving (from t = 1.0s), the residual wake propagated forwards through gaps and over the body. Figure 8.10 compared the velocity magnitudes and vertical velocity component along the vertical line close to, and in front of the manikins at t = 1.0s, 1.4s and 1.8s. The larger body generated stronger airflow in front of the lower body (Figure 8.10a), and slightly stronger upwash flow in front of the upper body (Figure 8.10b) compared to the slim body.

Over time, the residual wake from the slim body dissipated as the velocity field started to diminish from 1.4s, while for the larger body there was continued increase in the velocity field between 1.4s to 1.8s. This was due to relatively smaller passages of unobstructed airflow due to the larger torso blocking the flow, and stronger turbulent flow in the wake region due to the larger body size. This indicated that when a larger body came to a stop, this resulted in a stronger flow field in front of the body for a longer time, and a longer period of upward airflow towards the head which increased the potential for inhalation exposure.

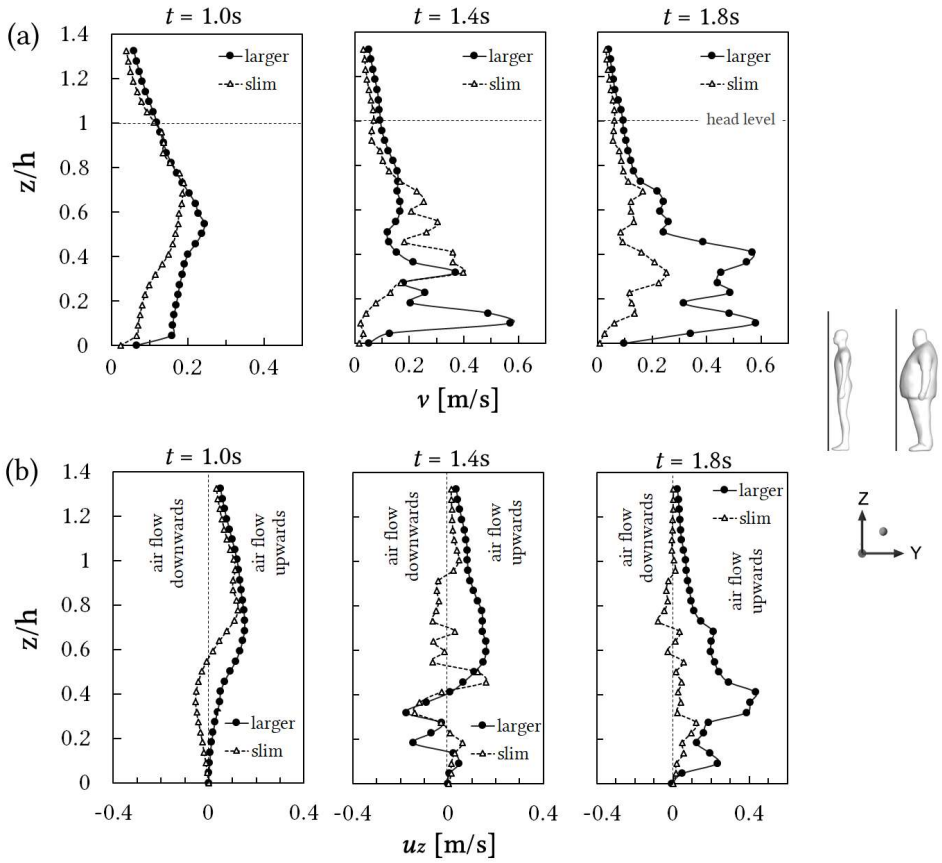

Figure 8.10 The comparisons of (a) velocity magnitude (v) and (b) vertical velocity (u_z) between the slim body and the larger body at the vertical line in front of the body at t = 1.0s, 1.4s and 1.8s.

8.3.6 Transient Flow Behaviour - Standing vs Walking Bodies

The comparisons of vertical velocity component (u_z) contours and vectors of the slim body in the standing and walking poses were made at the plane across the left leg (in a stance phase) (Figure 8.11a) and the right leg (in a swing phase) (Figure 8.11b).

At the left leg (Figure 8.11a), strong downward flow was generated closely behind the leg in the standing pose, whereas in the walking pose the left leg generated a continuously upwash and weaker downward flow behind the legs during the motion. When it decelerated from t = 0.6s to 1.0s, the circulation

behind the upper body in the standing pose was stronger with higher velocity components than in the walking pose, while at the lower body the walking pose had larger region with stronger upwash and weaker downwash on the left side. At the right leg (Figure 8.11b), the lifting of the right leg in the walking pose (swinging phase) contributed to less downwash in front of the leg and stronger upwash downstream the lower body than the standing pose during motion. When it decelerated from t = 0.6s to 1.0s, the flow field around the lifted right leg diminished quickly due to larger space between the legs.

The posture change came with varied angle between the heel and the ground and enlarged gap between legs. The results had suggested the phases of gait cycle exerts influences on the wake flow field. The posture of walking phases would potentially induce more contaminates from the floor to suspend when heels were lifting from the floor during the walking under the constant velocity. As the stance and swinging movement occupies most of the time during the gait cycle of human walking, the influence of realistic walking of

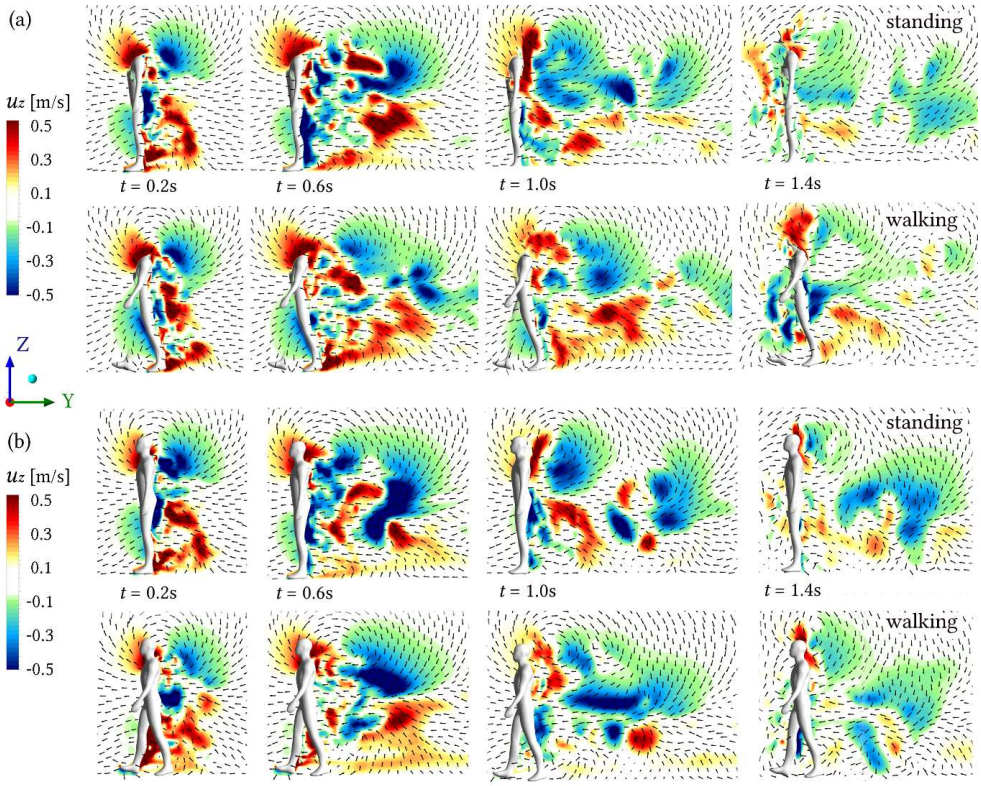

Figure 8.11 Vertical velocity component and vectors of the slim body in standing pose and walking pose at the plane across (a) the left leg and (b) the right leg at t = 0.2s, 0.6s, 1.0s, 1.0s.

occupants would exert manifest influences on contaminant transport comparing to models without swinging motion.

8.4 Conclusion

Unsteady CFD simulations using dynamic mesh method was applied for three different manikin models. Qualitative insight into the wake formation and vortex structures during the manikin motion were presented. The key points are summarised as follows:

- During the motion, the separation angle from the manikin head were quantified from computational simulations at the same locations as in the smoke visualisations. The comparisons showed reasonable agreement from the laminar model on the shift of angles due to the change in moving speeds.
- In the smoke visualisation, observations over time showed the entrainment of smoke particles into the wake flow and followed the movement of the body. This matched with the visualisation of vortex structures from the simulations in terms of the size and locations of the major patterns.
- The characteristic arch vortices in the wake region transported the smoke/pollutant downstream to the far wake. The reduction of walking speed shrunk the size of arch vortices thus hindered the spread of smoke/pollutants.
- Vortices generated by a larger body were larger and active closer to the ground due to a smaller aspect ratio, which was consistent with the findings of cylinders that the vortex size appeared to be a function of aspect ratio, with larger vortex and weaker upwash from the ground occurring for the smaller aspect ratio.
- When manikins stopped walking, the residual wake pushed the smoke/pollutants to surround the head for a longer time. Although the larger body had vortex structures shifting towards the ground which helped to keep the potential transport of pollutants at a lower height, the bigger blockage from the larger body had caused the smoke/pollutant to ascend around the head for a longer time.

- The CFD modelling revealed details of the flow field and provided reasonably good agreement to the experimental observations in terms of the separation points and the vortex structures in the wake region. The experimental and numerical study provided meaningful data for studying the transient moving effects of an object on wake flow development.

In this chapter, the thermal condition of the human body was not considered, thus the airflow pattern observed in the smoke visualisation and CFD simulations did not reflect the realistic interaction between the thermal plume and the wake flow. The thermal plume was considered to have minor influence on the wake flow structures, and iso-thermal conditions were considered capable of revealing the significant patterns of motion-induced wake.

Another major limitation is achieving dynamic similarity between large-scale models and the actual experiment used. Our results were $1/5^{th}$ scaled in dimensions but maintained the highest walking speed of 0.95 m/s; thus, the Reynolds number matching was $1/5^{th}$ of the dynamic similarity. Secondly, despite that the walking time of 2s in the experiment which is equivalent to scaled-up walking distance of 3.83m These limitations present challenges for future studies were larger scaled up models, and chambers can be used to address these issues.

Chapter 9
Conclusion

The motion-induced wake flow and its influence on contaminant transport have received increasing attention in recent years due to growing concerns about the health effects of occupant exposure to contaminants. This study has integrated CFD simulation and experimental measurements to provide more fundamental and in-depth analysis to the wake characteristics and induced contaminant transport. With developing computational resources, the complicated body geometry, realistic motion types and the transient walking process have been analysed and visualised. Moreover, the application of smoke visualisation on moving bodies has been explored as a supplemental way to provide not only visualisation of the wake structure, but also quantified results from image post-processing. In this computational and experimental study, we laid a solid foundation to the characteristics of realistic motion-induced wake flow and provided an understanding of the effects of body motion on particle exposure and indoor air quality. The main contributions from this thesis are:

(a) The experimental and numerical study provided meaningful data for understanding the spatial and temporal characteristics of the wake flow development of a moving object;

(b) The smoke visualisation technique on moving anthropomorphic manikins reproduced the motion-generated wake. It also provided a new perspective on visualisation of the dynamic wake structure;

(c) The CFD modelling revealed details of the flow field and provided reasonably good agreement with the experimental observations in terms of the location and main patterns of the vortex structures in the wake region, which can help quantify the transport of pollutants from and around the body and predict occupant exposure to contaminants;

9.1 Summary of the Contributions

The original summary of contributions in each chapter of this thesis are:

9.1.1 Wake Flow Patterns and Particle Dispersion Induced by Rigid Body Motion

Chapter 4 presents unsteady simulations of the wake flow induced by a rigid moving manikin in a confined room. Its influence on particle dispersion from a local source on the ground was discussed. The simulated flow field showed the fundamental flow patterns in the wake region. The airflow induced by the lower part of the legs induced an upward trend of airflow, which became the major contributor for particles to lift off the ground. The particles on the floors were significantly disturbed by the motion induced flow, thereby lifting off the ground and dispersing into the ambient air. This chapter provided some insight into the flow and particle dynamics. The particle suspension and its factor was significantly influenced by the moving manikin. Conclusions arising from this chapter are as follows:

- The recirculation region after the free end of the head, an upward flow in front of the upper body and a downwash flow at the back where highest velocity in the flow field occurs. At the lower part of the body, the wake flow gradually became horizontal due to the suppression by the airflow from the upper body.

- A pair of counter-rotating vortices was formed behind the moving manikin, one convecting off the head and another protruding from the gap of legs and extending downwards in the wake region.

- The slower walking speed induced less amount of suspension when the manikin walked through the same position, but the particles were more scattered within the indoor space due to a longer period of interaction between the body and particles, thus generating high concentration of particles near the breathing region which would cause hazard inhalation issues. When the manikin walked through more quickly within the same distance, more particles lifted off the floor, the dispersion was less scattered with particles ascending to a lower height.

- Comparisons between walking speeds showed a higher walking speed was conducive to avoid high particle concentration in the inhalation region owing to the instant contact between the body and particles.

- When the manikin stopped walking, the residual flow disturbances diminished downward and forward. When the manikin stopped moving, particles continue to spread into the ambient air and deposit towards the lower part of the front body due to the residual flow disturbances, and the particle concentration gradually diminished over time.

9.1.2 Comparisons of Wake Flow Between Swinging and Rigid Motion

In Chapter 5, the unsteady simulations of the wake flow induced by a moving manikin focuses on comparing the discrepancies generated in the flow field by simplified geometry, swinging limbs and thermal conditions. The key points are summarised as follows:

- By comparing a cylinder and a manikin with a similar aspect ratio, the main discrepancies were found behind the head and legs, where the body shape differed most. The wake showed similar patterns behind the upper part of the cylinder and the solid torso of the manikin, while at the lower region, there were distinct differences due to the air gaps from the arms and legs. The results showed the need for using a realistic geometry of human for analysing the airflow features of the human-induced wake.
- Using the swinging body motion produced a velocity fluctuation corresponding to the gait cycle, with peak values 2-4 times larger than the airflow velocity induced by the rigid motion in the same areas. The main discrepancy occurred in the lower half of the body influenced by the swinging legs.
- Heat transfer effects are negligible on the fluid flow during the walking motion of 1.2m/s. However, after the manikin has stopped moving it becomes important when considering the wake flow dynamics, especially in the upper body where thermal plume manifests.

9.1.3 Particle Suspension Induced by Realistic Manikin Motion

Chapter 6 presents the transient simulations of the wake flow induced by a moving thermal manikin with swinging limbs under different walking speeds.

Its influence on particle dispersion from the floor was investigated. Particle suspension caused by human activity and movement was influenced by the stratified airflow characteristics induced by the different body parts and its kinematics - the leg swing produced downward airflow in front while upward flow in back region, which transports particles toward the upper region during walking. However, a higher walking speed produced stronger downward airflow in the front of the body, which prevented the suspension of floor particles to rise to the upper body regions. The upper body produced upward flow in front of the body which caused particles to rise quickly into the breathing zone. At the back of the upper body a strong downwash was formed and caused particles to almost stick to the back of the body while in the manikin was moving.

The particle concentration comparison showed a higher walking speed produced less vertical transport of particles in front of the body thus helpful to reduce the exposure level to contaminants. While at a lower walking speed at 0.8m/s, particles were continuously transported to the upper region due to more upwards velocities in the wake structure. Additionally, the longer walking time leads to longer fluid-particle interaction and residence time for particle exposure.

This computational analysis of a very realistic moving manikin redispersing particles of the ground is a first step to better understand the effects of occupant activity on particle exposure and indoor air quality. As it's a first study there remains a caveat on the modelling efforts. This includes the assumption the feet not striking ground, thus no impact of foot strike is considered. Particle source was also limited to the floor region only, and in reality there is background airborne particle concentrations. Concentration sources could also be localised in one part of a room where a contaminant source may be found.

9.1.4 Smoke Visualisation of Three Moving Manikin Models

A smoke visualisation technique is presented in Chapter 7 for visualising a moving object through a stagnant environment. With high speed camera and image processing techniques to capture the generated smoke tracing the moving object, qualitative insight into the wake formation and its transformation

during the manikin motion were presented. The key points are summarised as follows:

- A larger body shape generated weaker upwash flow located downstream of the body and near the ground. This was due to the body's smaller aspect ratio compared to a slim body. If the smoke is considered as contaminants originating from the body, there would be less contaminants following the larger body as a larger amount remained close to the ground behind the body.
- A walking manikin pose influenced the vortex shedding. Uplifted heels induced upwash flow behind the feet and ascended the residual wake after the manikin came to a stop. The result suggests a swinging arm and leg motion would cause greater upwash flow at the feet and hand compared to a commonly adopted rigid body model.
- The wake flow that formed behind the manikin continued to travel under its own momentum and pass the manikin when it had stopped moving. The smoke moved upwards and surrounded the head, regardless of where the smoke was generated, e.g. from the head, shoulder or the back of the body. This suggests enhanced exposure to contaminants since more airflow is moving into the inhalation zone when manikin came to a stop.
- During the motion, quantitative data was analysed such as the separation angle from the manikin head, and vortex shedding frequency which can be used as validation of computational modelling.

9.1.5 CFD Modelling of Three Moving Manikin Models

Unsteady CFD simulations using dynamic mesh method is applied for three different manikin models in Chapter 8. The smoke visualisation of moving objects through a stagnant environment was used to provide validations for the computational study. Qualitative insight into the wake formation and vortex structures during the manikin motion were presented. The key points are summarised as follows:

- During the motion, the separation angle from the manikin head were quantified from computational simulations at the same locations as in

the smoke visualisations. The comparisons showed reasonable agreement from the laminar model on the shift of angles due to the change in moving speeds.

- In the smoke visualisation, observations over time showed the entrainment of smoke particles into the wake flow and followed the movement of the body. This matched with the visualisation of vortex structures from the simulations in terms of the size and locations of the major patterns.
- The characteristic arch vortices in the wake region transported the smoke/pollutant downstream to the far wake. The reduction of walking speed shrunk the size of arch vortices thus hindered the spread of smoke/pollutants.
- Vortices generated by a larger body were larger and active closer to the ground due to a smaller aspect ratio, which was consistent with the findings of cylinders that the vortex size appeared to be a function of aspect ratio, with larger vortex and weaker upwash from the ground occurring for the smaller aspect ratio.
- When manikins stopped walking, the residual wake pushed the smoke/pollutants to surround the head for a longer time. Although the larger body had vortex structures shifting towards the ground which helped to keep the potential transport of pollutants at a lower height, the bigger blockage from the larger body had caused the smoke/pollutant to ascend around the head for a longer time.
- The CFD modelling revealed details of the flow field and provided reasonably good agreement to the experimental observations in terms of the separation points and the vortex structures in the wake region. The experimental and numerical study provided meaningful data for studying the transient moving effects of an object on wake flow development.

Bibliography

Abdelsalam AM, Boopathi K, Gomathinayagam S, Hari Krishnan Kumar SS, Ramalingam V (2014). Experimental and Numerical Studies on the Wake Behavior of a Horizontal Axis Wind Turbine. *Journal of Wind Engineering and Industrial Aerodynamics,* 128: 54-65.

Al-Obaidi S, Wall JC, Al-Yaqoub A, Al-Ghanim M (2003). Basic Gait Parameters: A Comparison of Reference Data for Normal Subjects 20 to 29 Years of Age from Kuwait and Scandinavia. *J Rehabil Res Dev,* 40: 361-6.

ANSYS I. 2009. *Ansys Fluent 12.0 User's Guide* [Online]. Available: https://www.sharcnet.ca/Software/Ansys/17.0/en-us/help/flu_ug/flu_ug.html [Accessed].

Anthony TR, Flynn MR (2006). Computational Fluid Dynamics Investigation of Particle Inhalability. *Journal of Aerosol Science,* 37: 750-765.

Bjørn E, Nielsen PV (2002). Dispersal of Exhaled Air and Personal Exposure in Displacement Ventilated Rooms. *Indoor Air,* 12: 147-164.

Blevins RD 1990. *Flow-Induced Vibration*, New York, NY (USA); Van Nostrand Reinhold Co., Inc.; None.

Britt H. 1943. *Method of Producing Smoke.*

Brohus H, Balling KD, Jeppesen D (2006). Influence of Movements on Contaminant Transport in an Operating Room. *Indoor Air,* 16: 356-372.

Chang T-J, Hu T-S (2008). Transport Mechanisms of Airborne Particulate Matters in Partitioned Indoor Environment. *Building and Environment,* 43: 886-895.

Chen Q, Chao N-T (1997). Comparing Turbulence Models for Buoyant Plume and Displacement Ventilation Simulation. *Indoor and Built Environment,* 6: 140-149.

Choi JI, Edwards JR (2008). Large Eddy Simulation and Zonal Modeling of Human-Induced Contaminant Transport. *Indoor Air,* 18: 233-249.

Choi JI, Edwards JR (2012). Large-Eddy Simulation of Human-Induced Contaminant Transport in Room Compartments. *Indoor Air,* 22: 77-87.

Chung C-Y, Chung P-L (2007). A Numerical and Experimental Study of Pollutant Dispersion in a Traffic Tunnel. *Environmental Monitoring and Assessment,* 130: 289-299.

Craven BA, Settles GS (2006). A Computational and Experimental Investigation of the Human Thermal Plume. *Journal of Fluids Engineering,* 128: 1251-1258.

Edge BA, Paterson EG, Settles GS (2005). Computational Study of the Wake and Contaminant Transport of a Walking Human. *Journal of Fluids Engineering,* 127: 967-977.

EPA 2013. *The inside Story: A Guide to Indoor Air Quality*, Environmental Protection Agency.

Ferro AR, Kopperud RJ, Hildemann LM (2004). Source Strengths for Indoor Human Activities That Resuspend Particulate Matter. *Environmental Science & Technology,* 38: 1759-1764.

Flynn MR, Ljungqvist B (1995). A Review of Wake Effects on Worker Exposure. *Annals of Occupational Hygiene,* 39: 211-221.

Frederich O, Wassen E, Thiele F, Jensch M, Brede M, Hüttmann F, Leder A. Numerical Simulation of the Flow around a Finite Cylinder with Ground Plate in Comparison to Experimental Measurements. *In:* TROPEA, C., JAKIRLIC, S., HEINEMANN, H.-J., HENKE, R. & HÖNLINGER, H., eds. New Results in Numerical and Experimental Fluid Mechanics VI, 2008// 2008 Berlin, Heidelberg. Springer Berlin Heidelberg, 348-355.

Fung MC, Inthavong K, Yang W, Lappas P, Tu J (2013). External Characteristics of Unsteady Spray Atomization from a Nasal Spray Device. *Journal of Pharmaceutical Sciences,* 102: 1024-1035.

Gao N, He Q, Niu J (2012). Numerical Study of the Lock-up Phenomenon of Human Exhaled Droplets under a Displacement Ventilated Room. *Building Simulation,* 5: 51-60.

Gao NP, Niu JL (2005). Cfd Study of the Thermal Environment around a Human Body: A Review. *Indoor and Built Environment,* 14: 5-16.

Ge Q, Li X, Inthavong K, Tu J (2013). Numerical Study of the Effects of Human Body Heat on Particle Transport And inhalation in Indoor Environment. *Building and Environment,* 59: 1-9.

Ghorani-Azam A, Riahi-Zanjani B, Balali-Mood M (2016). Effects of Air Pollution on Human Health and Practical Measures for Prevention in Iran. *Journal of Research in Medical Sciences : The Official Journal of Isfahan University of Medical Sciences,* 21: 65.

Goldasteh I, Tian Y, Ahmadi G, R. Ferro A (2014). Human Induced Flow Field and Resultant Particle Suspension and Transport During Gait Cycle. *Building and Environment,* 77: 101-109.

Gomes C, Freihaut J, Bahnfleth W (2007). Resuspension of Allergen-Containing Particles under Mechanical and Aerodynamic Disturbances from Human Walking. *Atmospheric Environment,* 41: 5257-5270.

Han Z, Weng W, Huang Q (2014). Numerical and Experimental Investigation on the Dynamic Airflow of Human Movement in a Full-Scale Cabin. *HVAC&R Research,* 20: 444-457.

Han ZY, Weng WG, Huang QY, Fu M, Yang J, Luo N (2013). Aerodynamic Characteristics of Human Movement Behaviours in Full-Scale Environment: Comparison of Limbs Pendulum and Body Motion. *Indoor and Built Environment,* 24: 87-100.

Han ZY, Weng WG, Huang QY, Fu M, Yang J, Luo N (2015). Aerodynamic Characteristics of Human Movement Behaviours in Full-Scale Environment: Comparison of Limbs Pendulum and Body Motion. *Indoor and Built Environment,* 24: 87-100.

Hang J, Li Y, Jin R (2014). The Influence of Human Walking on the Flow and Airborne Transmission in a Six-Bed Isolation Room: Tracer Gas Simulation. *Building and Environment,* 77: 119-134.

Hayashi T, Ishizu Y, Kato S, Murakami S (2002). Cfd Analysis on Characteristics of Contaminated Indoor Air Ventilation and Its Application in

the Evaluation of the Effects of Contaminant Inhalation by a Human Occupant. *Building and Environment,* 37: 219-230.

Heist DK, Eisner AD, Mitchell W, Wiener R (2003). Airflow around a Child-Size Manikin in a Low-Speed Wind Environment. *Aerosol Science and Technology,* 37: 303-314.

Heschl C, Inthavong K, Sanz W, Tu J (2013). Evaluation and Improvements of Rans Turbulence Models for Linear Diffuser Flows. *Computers & Fluids,* 71: 272-282.

Heschl C, Inthavong K, Sanz W, Tu J (2014). Nonlinear Eddy Viscosity Modeling and Experimental Study of Jet Spreading Rates. *Indoor Air,* 24: 93-102.

Hospodsky D, Qian J, Nazaroff WW, Yamamoto N, Bibby K, Rismani-Yazdi H, Peccia J (2012). Human Occupancy as a Source of Indoor Airborne Bacteria. *PLoS ONE,* 7: e34867.

Inthavong K, Ge QJ, Li X, Tu JY (2013a). Source and Trajectories of Inhaled Particles from a Surrounding Environment and Its Deposition in the Respiratory Airway. *Inhalation Toxicology,* 25: 280-291.

Inthavong K, Ge QJ, Li XD, Tu JY (2012). Detailed Predictions of Particle Aspiration Affected by Respiratory Inhalation and Airflow. *Atmospheric Environment,* 62: 107-117.

Inthavong K, Mouritz AP, Dong J, Tu JY (2013b). Inhalation and Deposition of Carbon and Glass Composite Fibre in the Respiratory Airway. *Journal of Aerosol Science,* 65: 58-68.

Inthavong K, Tao Y, Petersen P, Mohanarangam K, Yang W, Tu J (2017). A Smoke Visualisation Technique for Wake Flow from a Moving Human Manikin. *Journal of Visualization,* 20: 125-137.

Inthavong K, Tian ZF, Tu JY (2009). Effect of Ventilation Design on Removal of Particles in Woodturning Workstations. *Building and Environment,* 44: 125-136.

Irwin PA (2008). Bluff Body Aerodynamics in Wind Engineering. *Journal of Wind Engineering and Industrial Aerodynamics,* 96: 701-712.

Johnson AE, Fetcher B, Saunders CJ (1996). Air Movement around a Worker in a Low-Speed Flow Field. *Annals of Occupational Hygiene,* 40: 57-64.

Kawamura T, Hiwada M, Hibino T, Mabuchi I, Kumada M (1984). Flow around a Finite Circular Cylinder on a Flat Plate : Cylinder Height Greater Than Turbulent Boundary Layer Thickness. *Bulletin of JSME,* 27: 2142-2151.

Khare P, Marr LC (2014). Simulation of Vertical Concentration Gradient of Influenza Viruses in Dust Resuspended by Walking. *Indoor Air,* 25: 428-440.

Kim T, Flynn MR (1991). Airflow Pattern around a Worker in a Uniform Freestream. *American Industrial Hygiene Association Journal,* 52: 287-296.

Kolář V (2007). Vortex Identification: New Requirements and Limitations. *International Journal of Heat and Fluid Flow,* 28: 638-652.

KrajnoviĆ S (2011). Flow around a Tall Finite Cylinder Explored by Large Eddy Simulation. *Journal of Fluid Mechanics,* 676: 294-317.

Kulmala I, Saamanen A, Enbom S (1996a). The Effect of Contaminant Source Location on Worker Exposure in the near-Wake Region. *The Annals of Occupational Hygiene,* 40: 511-523.

Kulmala I, Säämänen A, Enbom S (1996b). The Effect of Contaminant Source Location on Worker Exposure in the near-Wake Region. *The Annals of Occupational Hygiene,* 40: 511-523.

Lam HF, Peng HY (2016). Study of Wake Characteristics of a Vertical Axis Wind Turbine by Two- and Three-Dimensional Computational Fluid Dynamics Simulations. *Renewable Energy,* 90: 386-398.

Launder BE, Spalding DB (1974). The Numerical Computation of Turbulent Flows. *Computer Methods in Applied Mechanics and Engineering,* 3: 269-289.

Li C, Ito K (2014). Numerical and Experimental Estimation of Convective Heat Transfer Coefficient of Human Body under Strong Forced Convective Flow. *Journal of Wind Engineering and Industrial Aerodynamics,* 126: 107-117.

Li X, Inthavong K, Ge Q, Tu J (2013). Numerical Investigation of Particle Transport and Inhalation Using Standing Thermal Manikins. *Building and Environment,* 60: 116-125.

Li X, Inthavong K, Tu J (2012). Particle Inhalation and Deposition in a Human Nasal Cavity from the External Surrounding Environment. *Building and Environment,* 47: 32-39.

Li X, Inthavong K, Tu J (2014). Numerical Investigation of Micron Particle Inhalation by Standing Thermal Manikins in Horizontal Airflows. *Indoor and Built Environment,*

Liu C, Wang Y, Yang Y, Duan Z (2016). New Omega Vortex Identification Method. *Science China Physics, Mechanics & Astronomy,* 59: 684711.

López González M, Galdo Vega M, Fernández Oro JM, Blanco Marigorta E (2014). Numerical Modeling of the Piston Effect in Longitudinal Ventilation Systems for Subway Tunnels. *Tunnelling and Underground Space Technology,* 40: 22-37.

Luo N, Weng W, Xu X, Fu M (2017). Human-Walking-Induced Wake Flow – Piv Experiments and Cfd Simulations. *Indoor and Built Environment,* 1420326X17701279.

Luo N, Weng WG, Fu M (2015). Theoretical Analysis of the Effects of Human Movement on the Combined Free-Forced Convection. *International Journal of Heat and Mass Transfer,* 91: 37-44.

Mahjoub Said N, Mhiri H, Bournot H, Le Palec G (2008). Experimental and Numerical Modelling of the Three-Dimensional Incompressible Flow Behaviour in the near Wake of Circular Cylinders. *Journal of Wind Engineering and Industrial Aerodynamics,* 96: 471-502.

Matsumoto H, Ohba Y (2004). The Influence of a Moving Object on Air Distribution in Displacement Ventilated Rooms. *Journal of Asian Architecture and Building Engineering,* 3: 71-75.

Mazumdar S, Poussou SB, Lin C-H, Isukapalli SS, Plesniak MW, Chen Q (2011). Impact of Scaling and Body Movement on Contaminant Transport in Airliner Cabins. *Atmospheric Environment,* 45: 6019-6028.

Mazumdar S, Yin Y, Guity A, Marmion P, Gulick B, Chen Q (2010). Impact of Moving Objects Oncontaminant Concentration Distributions in an Inpatient Ward with Displacement Ventilation. *HVAC&R Research,* 16: 545-563.

Menter FR (1994). Two-Equation Eddy-Viscosity Turbulence Models for Engineering Applications. *AIAA Journal,* 32: 1598-1605.

Miguel AF, Aydin M, Reis AH (2005). Indoor Deposition and Forced Re-Suspension of Respirable Particles. *Indoor and Built Environment,* 14: 391-396.

Moin P, Kim J (2006). The Structure of the Vorticity Field in Turbulent Channel Flow. Part 1. Analysis of Instantaneous Fields and Statistical Correlations. *Journal of Fluid Mechanics,* 155: 441-464.

Murakami S, Deguchi K (1981). New Criteria for Wind Effects on Pedestrians. *Journal of Wind Engineering and Industrial Aerodynamics,* 7: 289-309.

Murakami S, Zeng J, Hayashi T (1999). Cfd Analysis of Wind Environment around a Human Body. *Journal of Wind Engineering and Industrial Aerodynamics,* 83: 393-408.

Oberoi RC, Choi J-I, Edwards JR, Rosati JA, Thornburg J, Rodes CE (2010). Human-Induced Particle Re-Suspension in a Room. *Aerosol Science and Technology,* 44: 216-229.

Octavian F, Jon S, Dirk ML, Frank T (2011). Large-Scale Dynamics in the Flow around a Finite Cylinder with a Ground Plate. *Fluid Dynamics Research,* 43: 015504.

Oh W, Kato S (2018). The Effect of Airspeed and Wind Direction on Human's Thermal Conditions and Air Distribution around the Body. *Building and Environment,* 141: 103-116.

Oliveira AVM, Gaspar AR, Francisco SC, Quintela DA (2014). Analysis of Natural and Forced Convection Heat Losses from a Thermal Manikin: Comparative Assessment of the Static and Dynamic Postures. *Journal of Wind Engineering and Industrial Aerodynamics,* 132: 66-76.

Ono T, Murakami S, Ooka R, Omori T (2008). Numerical and Experimental Study on Convective Heat Transfer of the Human Body in the Outdoor

Environment. *Journal of Wind Engineering and Industrial Aerodynamics,* 96: 1719-1732.

Park S-J, Kim J-J, Kim MJ, Park RJ, Cheong H-B (2015). Characteristics of Flow and Reactive Pollutant Dispersion in Urban Street Canyons. *Atmospheric Environment,* 108: 20-31.

Poussou S, Plesniak M (2015). Flow Field in the Wake of a Bluff Body Driven through a Steady Recirculating Flow. *Experiments in Fluids,* 56: 1-16.

Poussou SB, Mazumdar S, Plesniak MW, Sojka PE, Chen Q (2010). Flow and Contaminant Transport in an Airliner Cabin Induced by a Moving Body: Model Experiments and Cfd Predictions. *Atmospheric Environment,* 44: 2830-2839.

Poussou SB, Plesniak MW (2012). Vortex Dynamics and Scalar Transport in the Wake of a Bluff Body Driven through a Steady Recirculating Flow. *Experiments in Fluids,* 53: 747-763.

Qian J, Ferro AR (2008). Resuspension of Dust Particles in a Chamber and Associated Environmental Factors. *Aerosol Science and Technology,* 42: 566-578.

Qian J, Peccia J, Ferro AR (2014). Walking-Induced Particle Resuspension in Indoor Environments. *Atmospheric Environment,* 89: 464-481.

Rodriguez I, Borell R, Lehmkuhl O, Perez Segarra CD, Oliva A (2011). Direct Numerical Simulation of the Flow over a Sphere at Re = 3700. *Journal of Fluid Mechanics,* 679: 263-287.

Rostamy N, Sumner D, Bergstrom DJ, Bugg JD (2012). Local Flow Field of a Surface-Mounted Finite Circular Cylinder. *Journal of Fluids and Structures,* 34: 105-122.

Saarinen P, Kalliomäki P, Koskela H, Tang J (2018). Large-Eddy Simulation of the Containment Failure in Isolation Rooms with a Sliding Door—an Experimental and Modelling Study. *Building Simulation,* 11: 585-596.

Salmanzadeh M, Zahedi G, Ahmadi G, Marr DR, Glauser M (2012). Computational Modeling of Effects of Thermal Plume Adjacent to the Body

on the Indoor Airflow and Particle Transport. *Journal of Aerosol Science,* 53: 29-39.

Sasaki R, Yamada M, Uematsu Y, Saeki H (2000). Comfort Environment Assessment Based on Bodily Sensation in Open Air: Relationship between Comfort Sensation and Meteorological Factors. *Journal of Wind Engineering and Industrial Aerodynamics,* 87: 93-110.

Se CMK, Inthavong K, Tu J (2010). Inhalability of Micron Particles through the Nose and Mouth. *Inhalation Toxicology,* 22: 287-300.

Sohankar A, Mohagheghian S, Dehghan AA, Dehghan Manshadi M (2015). A Smoke Visualization Study of the Flow over a Square Cylinder at Incidence and Tandem Square Cylinders. *Journal of Visualization,* 18: 687-703.

Solazzo E, Cai X, Vardoulakis S (2008). Modelling Wind Flow and Vehicle-Induced Turbulence in Urban Streets. *Atmospheric Environment,* 42: 4918-4931.

Tao Y, Inthavong K, Petersen P, Mohanarangam K, Yang W, Tu J (2018). Experimental Visualisation of Wake Flows Induced by Different Shaped Moving Manikins. *Building and Environment,* 142: 361-370.

Tao Y, Inthavong K, Tu J (2016). Computational Fluid Dynamics Study of Human-Induced Wake and Particle Dispersion in Indoor Environment. *Indoor and Built Environment,* 26: 185-198.

Tao Y, Inthavong K, Tu J (2017a). A Numerical Investigation of Wind Environment around a Walking Human Body. *Journal of Wind Engineering and Industrial Aerodynamics,* 168: 9-19.

Tao Y, Inthavong K, Tu JY (2017b). Dynamic Meshing Modelling for Particle Resuspension Caused by Swinging Manikin Motion. *Building and Environment,* 123: 529-542.

Thatcher TL, Wilson DJ, Wood EE, Craig MJ, Sextro RG (2004). Pollutant Dispersion in a Large Indoor Space: Part 1 – Scaled Experiments Using a Water-Filled Model with Occupants and Furniture. *Indoor Air,* 14: 258-271.

Tian L, Inthavong K, Lidén G, Shang Y, Tu J (2016). Transport and Deposition of Welding Fume Agglomerates in a Realistic Human Nasal Airway. *The Annals of Occupational Hygiene,* 60: 731-747.

Tian Y, Sul K, Qian J, Mondal S, Ferro AR (2014). A Comparative Study of Walking-Induced Dust Resuspension Using a Consistent Test Mechanism. *Indoor Air,* 24: 592-603.

Tominaga Y (2015). Flow around a High-Rise Building Using Steady and Unsteady Rans Cfd: Effect of Large-Scale Fluctuations on the Velocity Statistics. *Journal of Wind Engineering and Industrial Aerodynamics,* 142: 93-103.

Tominaga Y, Stathopoulos T (2013). Cfd Simulation of near-Field Pollutant Dispersion in the Urban Environment: A Review of Current Modeling Techniques. *Atmospheric Environment,* 79: 716-730.

Tsai MY, Chen KS (2004). Measurements and Three-Dimensional Modeling of Air Pollutant Dispersion in an Urban Street Canyon. *Atmospheric Environment,* 38: 5911-5924.

Wang H, Zhou Y, Chan C, Zhou T (2009). Momentum and Heat Transport in a Finite-Length Cylinder Wake. *Experiments in Fluids,* 46: 1173-1185.

Wang HF, Zhou Y (2009). The Finite-Length Square Cylinder near Wake. *Journal of Fluid Mechanics,* 638: 453-490.

Wang J, Chow T-T (2011). Numerical Investigation of Influence of Human Walking on Dispersion and Deposition of Expiratory Droplets in Airborne Infection Isolation Room. *Building and Environment,* 46: 1993-2002.

Wu Y, Gao NP (2014). The Dynamics of the Body Motion Induced Wake Flow and Its Effects on the Contaminant Dispersion. *Building and Environment,* 82: 63-74.

Yakhot V, Orszag S (1986). Renormalization-Group Analysis of Turbulence. *Physical Review Letters,* 57: 1722-1724.

Yakhot V, Orszag SA, Thangam S, Gatski TB, Speziale CG (1992). Development of Turbulence Models for Shear Flows by a Double Expansion Technique. *Physics of Fluids A,* 4: 1510-1520.

You S, Wan MP (2015). Experimental Investigation and Modelling of Human-Walking-Induced Particle Resuspension. *Indoor and Built Environment,* 24: 564-576.

Zhang K, Katsuchi H, Zhou D, Yamada H, Han Z (2016). Numerical Study on the Effect of Shape Modification to the Flow around Circular Cylinders. *Journal of Wind Engineering and Industrial Aerodynamics,* 152: 23-40.

Zhang Z, Zhang W, Zhai ZJ, Chen QY (2007). Evaluation of Various Turbulence Models in Predicting Airflow and Turbulence in Enclosed Environments by Cfd: Part 2—Comparison with Experimental Data from Literature. *HVAC&R Research,* 13: 871-886.

Zhou B, Zhao B, Tan Z (2011). How Particle Resuspension from Inner Surfaces of Ventilation Ducts Affects Indoor Air Quality—a Modeling Analysis. *Aerosol Science and Technology,* 45: 996-1009.

Zukowska D, Melikov AK, Popiolek ZJ (2007). Thermal Plume above a Simulated Sitting Person with Different Complexity of Body Geometry. *Roomvent 2007: Proceedings of the 10th International Conference on Air Distribution in Rooms.,* 3: 191-198.